ALMA MATER STUDIORUM · UNIVERSITÀ DI BOLOGNA

Characterization of a versatile and sensitive detector for gamma-ray astronomy

Tesi di Laurea Magistrale

Presentata da:
Gabriele C. Gangemi

Relatore:
Chiar.mo Prof.
Cristian Vignali

Co-relatori:
Dott.Fabio Fuschino
Dott.Riccardo Campana

Sessione II
Anno Accademico 2015-2016

This thesis work was done as part of the research activity of the Istituto di Astrofisica Spaziale e Fisica Cosmica (IASF) in Bologna.

Esiste un uomo, dall'anima tanto ottenebrata
che non abbia mai detto a se stesso
"Questa è la mia terra, la terra natia!",
il cui cuore non abbia mai palpitato
al momento di volgere le sue orme verso la patria
dopo aver errato per contrade straniere?

Sir Walter Scott

Introduzione

L'astronomia in banda γ studia i fenomeni più violenti dell'Universo. L'osservazione di tale radiazione non è tuttavia banale: nuove tecniche e tecnologie sono sviluppate di continuo in modo da superare le sfide poste dall'osservazione diretta in questa banda.

Il lavoro presentato in questa tesi è stato svolto presso l'Istituto di Astrofisica Spaziale e Fisica Cosmica di Bologna (IASF-Bologna) nell'ambito delle attività di ricerca della collaborazione ReDSoX (REsearch Drift for SOft X-rays). Le attività di tale collaborazione sono finanziate dall'Istituto Nazionale di Fisica Nucleare (INFN) e dalla Fondazione Bruno Kessler (FBK) e coinvolgono diversi istituti di ricerca ed università italiane. ReDSoX mira allo sviluppo, alla realizzazione e all'ottimizzazione di *Silicon Drift Detector* indirizzati verso campi applicativi molto differenti tra di loro, dalla spettroscopia X alla fisica nucleare e medica, fino all'astrofisica spaziale. Il mio progetto di tesi si pone come obiettivo la realizzazione di uno spettrometro γ per missioni di astrofisica spaziale. Tale spettrometro si basa su una tecnologia nota e affidabile come quella dei rivelatori al Silicio, i cui processi produttivi sono ben collaudati e capaci di garantire elevate prestazioni spettroscopiche e temporali, mantenendo un design compatto e la possibilità di lavorare senza la necessità di un sistema attivo di raffreddamento.

Il lavoro presentato in questa tesi riguarda la caratterizzazione di un prototipo di rivelatore realizzato accoppiando un cristallo scintillatore con un rivelatore a stato solido (Silicon Drift Detector, SDD). Il fotorivelatore è costituito da una matrice di 7 SDD a geometria esagonale. Tale matrice è stata disegnata con lo specifico obiettivo di essere utilizzata come fotorivelatore per la luce di scintillazione proveniente da un

cristallo scintillatore commerciale di forma cilindrica e dal diametro di 0,5". Abbiamo utilizzato un cristallo di Bromuro di Lantanio attivato al Cerio, $LaBr_3(Ce)$. Esso è un cristallo di nuova generazione caratterizzato da un'elevata produzione di luce (*light yield*), un tempo di emissione molto rapido e alta linearità. Queste proprietà lo rendono uno degli scintillatori più promettenti per la spettroscopia γ. In questa tesi abbiamo testato ampiamente il prototipo sia per le sue prestazioni spettroscopiche che temporali. Sono state misurate le prestazione in termini di rumore sia a temperatura ambiente che a temperature moderatamente basse ($-10\,°C/-20\,°C$). I segnali sono stati processati sia con una catena spettroscopica analogica sia con una digitale, confrontandone i risultati.

Data la particolarità dei meccanismi fisici in gioco e la natura sperimentale di questo lavoro, è stata ritenuta necessaria l'inclusione di una lunga introduzione. Nel Capitolo 1 è introdotto il contesto astrofisico in cui questo lavoro si colloca, descrivendo i principali meccanismi di emissione responsabili della produzione di raggi γ, includendo una breve descrizione della storia dell'astronomia in banda γ e soffermandosi su come la scoperta di nuovi fenomeni sia legata allo sviluppo tecnologico. Nel Capitolo 2, a dimostrazione dell'estrema flessibilità e versatilità che contraddistingue le SDD, sono presentate alcune missioni spaziali in fase di studio che si propongono obiettivi scientifici molto differenti tra di loro ma che presentano, come elemento in comune, un rivelatore realizzato sfruttando la tecnologia delle SDD accoppiato con un cristallo scintillatore. Nel Capitolo 3 sono descritti i rivelatori γ più comuni, i loro principi di funzionamento e gli elementi tipici che costituiscono le catene spettroscopiche. Il Capitolo 4 è interamente dedicato alle SDD, al loro principio di funzionamento e alle loro proprietà base, mentre il Capitolo 5 è incentrato sulle proprietà degli scintillatori con una particolare attenzione al $LaBr_3(Ce)$. Nel Capitolo 6 è affrontata l'intera caratterizzazione del prototipo, dalle analisi preliminari atte ad assicurarsi il corretto funzionamento della matrice di SDD, all'accoppiamento con il cristallo fino alle analisi delle prestazioni spettroscopiche e temporali. Nel Capitolo 7 sono riassunti i principali risultati ottenuti e vengono fatte alcune considerazioni sulle prospettive future che questa tecnologia offre.

Parte del lavoro presentato in questa tesi è stato pubblicato in Fuschino, Labanti,

Campana, Gangemi, et al. Proc. SPIE, 9905, 99056J (2016).

iv

Introduction

γ-ray astronomy studies the most energetic phenomena of the Universe. Observation of γ-ray emission is not a trivial task: new techniques and technologies are continuously developed to overcome the challenges set by the direct observation of astronomical γ-rays. The progress in this field, even more than in the other fields of astronomy, is closely linked to the technological development.

This thesis work has been carried at the Istituto di Astrofisica Spaziale e Fisica Cosmica in Bologna (IASF-Bologna) among the activities of the ReDSoX (REsearch Drift for SOft X-rays) collaboration that involves several research institutes and universities. The activities of the ReDSoX collaboration are financed by the Istituto Nazionale Fisica Nucleare (INFN) and by Fondazione Bruno Kessler (FBK). ReDSoX is aimed at developing and customizing the layouts of Silicon Drift Detectors for different applications, such as X-rays spectroscopy, nuclear and medical physics and space astrophysics. My thesis project aims at developing an innovative γ-ray detector to be used in astrophysical space missions, based on a reliable technology such as the Silicon-based detector, that is able to achieve high-spectroscopic and timing performance over a wide energetic range, keeping a compact design and being able to work without an active cooling system.

The work presented in this thesis is based on the characterization of a prototype detector that consists of a solid state device (a Silicon Drift Detector, SDD) coupled with a scintillator crystal. The device used here is a multi-cell SDD, composed of 7 hexagonal cells. This matrix has been designed to be coupled with commercially available cylindrically shaped crystals of 0.5" diameter. The crystal used here is Cerium-activated Lanthanium Bromide, $LaBr_3(Ce)$, a new generation scintillator

characterized by a high light yield, a fast decay time and excellent linearity. Such properties make LaBr$_3$(Ce) one of the most promising scintillator crystals for spectroscopic and timing applications. In this thesis, we have extensively tested the device in both spectroscopic and timing performances. The noise performance and spectroscopic characterization of the entire device has been carried out at room and lower temperatures (-10 °C/-20 °C). The analysis has been performed with both an analog and digital spectroscopic chain, and the comparison of the results is also presented.

Given the complex nature of the experiment and underlying physics, a long introduction has been included in my thesis. Chapter 1 introduces the astrophysical context, i.e. γ-ray astronomy, from the emission mechanisms resulting in the production of γ-rays throughout the Universe to a brief introduction of the history of γ-ray astronomy, with a particular emphasis on how the discovery of new γ-ray astronomical phenomena is tied to the technological development. Chapter 2 presents some of the proposed γ-ray satellite missions currently under study. Although these space missions pursue different scientific objectives, all of them are equipped with a γ-ray spectrometer that can be obtained by coupling high-performing Silicon photodetectors and scintillator crystals similar to the one which is studied in this thesis. This demonstrates that the use of this type of technology is extremely flexible for different scientific applications, towards which the γ-ray astronomy is heading. Given the technological nature of this thesis, in Chapter 3 the most common γ-ray detectors, their working principles and typical spectroscopic setups are described. Chapter 4 is instead dedicated to a more specific overview of the SDD working principle and basic characteristics, and Chapter 5 is about the properties of scintillators crystals, with a particular emphasis on LaBr$_3$(Ce). Chapter 6 describes the complete characterization of the prototype, including the preliminary analysis performed to ensure the correct operation of the SDDs matrix, the coupling with the crystal and the analysis of the γ-ray spectroscopic and timing performance. In Chapter 7 the main results of my work are summarized, and some future applications of this technology are delineated.

Part of the work presented in this thesis has been published in Fuschino, Labanti,

Campana, Gangemi, et al. Proc. SPIE, 9905, 99056J (2016).

Contents

Chapter 1

Gamma-ray astronomy

γ-ray astronomy is the application field for which the prototype tested in this thesis is designed.

The observation of astrophysical γ-ray radiation is very challenging. One of the main problems is that γ-rays are absorbed by Earth's atmosphere. For this reason, direct observation of celestial γ-rays cannot be ground-based. This issue can be solved by bringing the instrumentation in space via satellites.

However, realizing a satellite is a constant compromise between the science to be studied and the limitations sets by the availability of funds. The study of a particular scientific case requires the use of appropriate instrumentation but building such a payload must take in account several factors. The size of the payload defines which launch vehicle must be used, its weight and the orbit where the satellite must be placed define the amount of fuel needed. From this follows the need to realize instrumentation the more compact, lightweight and performing as possible, without neglecting the reliability, since once sent in orbit, the possibility of eventual repairs is close to zero.

The prototype examined in this thesis aims at fulfilling these requirements. It can be thought not only as a single detector, but also as the basic unit on which to design detectors with different shapes and sizes. Its energy band goes from few keys to several MeVs. This bandwidth allows us not only to study the most energetic phenomena of the Universe, such as supernovae explosions and γ-ray bursts, but also

to address questions across a broad range of topics, including the origin of transient sources, the nature of dark matter and the origin of cosmic rays.

γ-ray observation techniques are different from those used in other bands of the electromagnetic spectrum. The great sensitivity of traditional telescopes is due to the focusing of light on small dimension detectors. This is not possible in γ-rays since their energy and wavelength do not allow focusing (Skinner et al., 2004), so the collecting area of a γ-ray telescope is usually equal to the detector one. To improve sensitivity, an increase of detector size is required.

Another challenge is due to the shortage of photons. γ-ray photons carry a great energy, therefore, assuming for example a source which emits the same amount of energy in different energetic bands, the γ-ray photons will be present in a lower number than the optical or infrared ones. This implies longer exposure times to collect a statistically significant number of photons.

Because of all these issues γ-ray astronomy is not even 60 years old, having to wait for the development of proper technologies.

1.1   The gamma-ray sky

Observing the sky at different wavelengths allows us to look at phenomena that are invisible to our own eyes. The γ-ray sky is very different from the optical one: there is almost no Sun, a diffuse cloud-shaped ring traces the Milky Way and the surrounding sky is filled by a bright glow of γ-rays produced by cosmic rays, remnants of exploded stars and other structures that may be the annihilation sites of dark matter particles.

The physical processes described in the next subsections produce γ-rays that illuminate the γ-ray sky allowing satellite such as Fermi to capture images like the one shown in Figure 1.1 where we can distinguish point-like sources and diffuse emission.
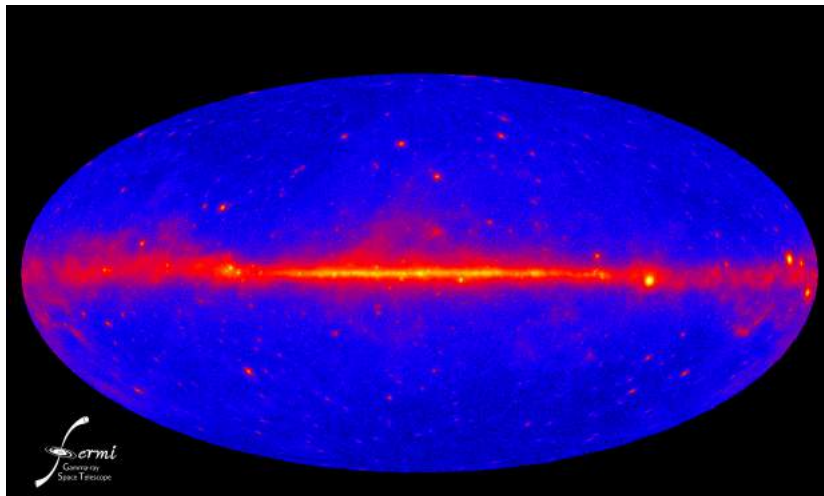
Figure 1.1: *The entire sky at energies higher than 1 GeV based on five years of data from the LAT instrument on NASA's Fermi Gamma-ray Space Telescope. Image Credit: NASA/DOE/Fermi LAT Collaboration.*

1.1.1 Emission processes

Many processes involve the production or interaction of γ-rays: *bremsstrahlung, synchrotron radiation, inverse Compton scattering* and *pion decay*. In the first three processes, high-energy electrons are also involved, the latter is a decay process.

Each process that involves radiation or particles is characterized by its own *cross section*. The cross section gives a measure of the probability for a reaction to occur and may be analytically calculated if the form of the basic interaction between particles is known. Formally, the cross section is defined in the following manner. Consider a beam of particles I incident upon a target particle as shown in Figure 1.2. Assume that the particles in the beam are uniformly distributed in space and time. Because of the randomness of the impact parameters (defined as the perpendicular distance between the path of an incoming particle and the target), the number of scattered particles will fluctuate over different time intervals. However, averaging many finite measuring periods, this number will tend towards a fixed $dN_s/d\Omega$, where N_s is the average number of scattered particles per unit time and $d\Omega$ the solid angle. The *differential cross section* is then defined as:
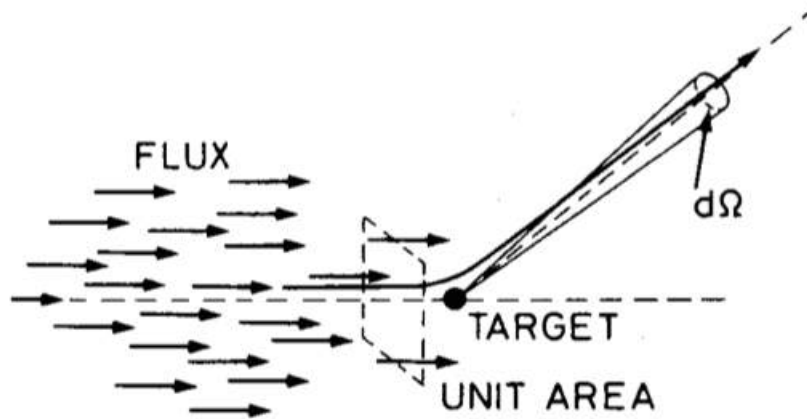
Figure 1.2: *Definition of the scattering cross section.*

$$\frac{d\sigma}{d\Omega}(E, \Omega) = \frac{1}{F}\frac{dN_s}{d\Omega} \tag{1.1}$$

where $d\sigma/d\Omega$ is the average fraction of the particles scattered into $d\Omega$ per unit time per unit flux F and $d\sigma$ has dimensions of area. The *total cross section* can be calculated as the integral of $d\sigma/d\Omega$ over all solid angles:

$$d\sigma(E) = \int d\Omega \frac{d\sigma}{d\Omega} \tag{1.2}$$

Now that some basic notions have been given, in the following a description of the physical processes resulting in production γ-rays will be given. The formalism is based on Rybicki and Lightman (1979).

1.1.1.1   Bremsstrahlung

The German word *Bremsstrahlung* means "braking radiation" and refers to the energy emitted by a charged particle with a non-zero acceleration, for example when it is deflected by another charged particle, as in the case of the scattering of an electron by an atomic nucleus. A typical Bremsstrahlung spectrum is shown in Figure 1.3.
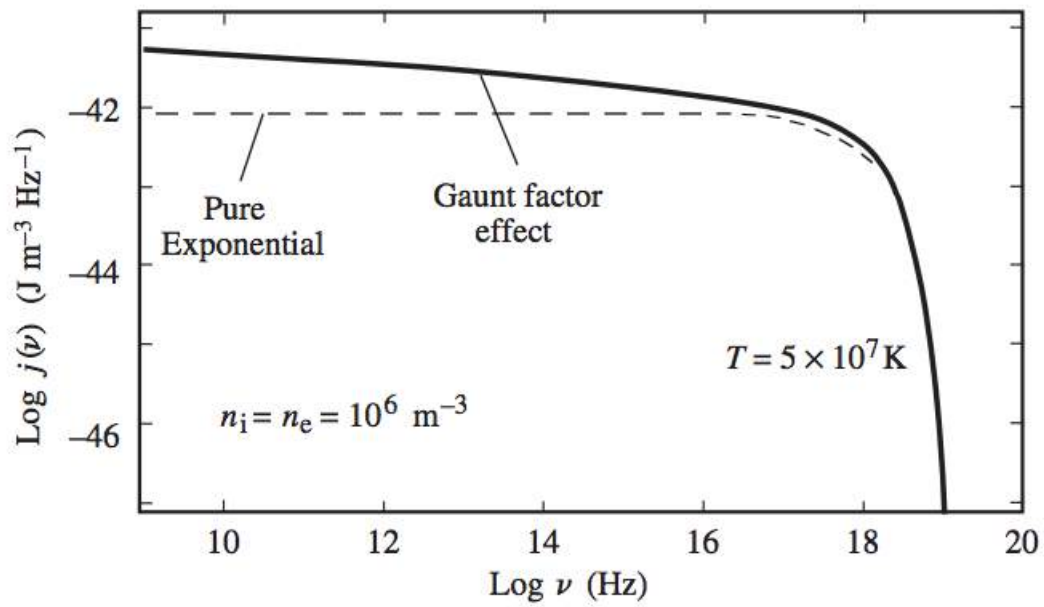
Figure 1.3: *Theoretical continuum thermal bremsstrahlung spectrum for a flux of $n_e = 10^6$ electrons per unit of volume at a temperature of 5×10^7 K. The volume emissivity is also plotted with the Gaunt factor included. Figure from Rybicki and Lightman (1979).*

1.1.1.2 Synchrotron radiation

If the physical deflection experienced by charged particles is due to a magnetic field, the interaction takes the name of *magnetic Bremsstrahlung* or *synchrotron radiation.* If the electrons, while moving at velocity close to light speed c, cross a magnetic field on their way, they are deflected by the *Lorentz force* $q(\overrightarrow{v} \times \overrightarrow{B})$ and, as they accelerate, they lose some of their kinetic energy.

The spectrum $I(\nu)$ [Wm^{-2}Hz^{-1}sr^{-1}] of such radiation depends on the shape of the electron's energy spectrum.

Assuming for the electron distribution $N(E) = N_0 E^{-\delta}$ where N_0 and δ are constants, the specific emissivity can be approximated as:

$$j_s(\nu) \propto \nu^{-(\delta-1)/2} = \nu^{-\alpha} \quad \text{where } \alpha = \frac{\delta - 1}{2} \tag{1.3}$$

The emitted synchrotron spectrum is a power law where α is the *photon index* which depends exclusively on the electron distribution.

1.1.1.3 Inverse Compton scattering

When a photon of energy $E = h\nu$ hits an electron at rest, it can transfer part of its energy and momentum to the electron such as in an elastic collision between particles. What results from this interaction is thus a photon shifted to a longer wavelength and an accelerated electron, both scattered from the initial trajectory by angles θ and ϕ respectively. The scattered wavelength depends from the amount of energy and momentum transferred according to the equation

$$\lambda' - \lambda = \frac{h}{m_e c}(1 - \cos\theta) \tag{1.4}$$

where λ is the initial wavelength of the photon, λ' is the wavelength after the scattering, h is the Planck constant, m_e is the electron rest mass, c is the speed of light and θ the scattering angle of the photon. The electron scattering angle ϕ is a consequence of the above formula under the conservation of energy and momentum. This process

is known as *Compton scattering.*

However, there is also the reverse case, in which a low-energy photon gains energy from scattering off a relativistic electron, that takes the name of *inverse Compton scattering.* If $E_\gamma = h\nu$ is the energy of the photon, then the condition $E_\gamma \ll m_e c^2$ defines the *Thomson* or classical regime, and $E_\gamma \gg m_e c^2$ defines the *Klein-Nishina,* or relativistic regime.

1.1.1.4 Pion decay

Pions are mesons, which means that they are made of a quark and an antiquark, and are produced from interactions between high energy hadrons. There are three different pions: π^+ and π^- that are charged particles, and the π^0 that is neutral. The decay processes of the first two do not involve γ-rays so they are not described here.

The π^0 has a mass of 135 MeV/c^2, an average lifetime of $\sim 8.3 \times 10^{-17}$s, much shorter than the other two pions, and it decays via electromagnetic interaction. Up to now, five π^0 decay modes have been observed, two of them leading to the production of at least one γ-ray. The fraction of particles which decay by an individual decay mode is expressed by the *branching ratio*, if only one decay mode can occur, its branching ratio is equal to unity. The π^0 main decay mode, with a branching ratio of 0.988, is the following:

$$\pi^0 \rightarrow \gamma + \gamma \tag{1.5}$$

the other, much less likely with a branching ratio of 0.01174, is

$$\pi^0 \rightarrow \gamma + e^- + e^+ \tag{1.6}$$

1.1.2 Diffuse Emission

"Diffuse" γ-ray emission consist of several components: truly diffuse emission from the interstellar medium, the extragalactic background, whose origin is not yet firmly

established, and the contribution from unresolved and faint Galactic point sources (Fichtel et al., 1978). The Galactic diffuse emission dominates over other components and has a wide distribution with most emission coming from the Galactic plane.

The diffuse emission from the interstellar medium is strictly correlated with the Milky Way structures. It is mainly due to cosmic rays: protons, nuclei or electrons that, after being accelerated to relativistic velocities, travel through the interstellar medium confined by Galactic magnetic field. When one of these particles goes nearby a bulk of interstellar gas, slows down and produces γ-rays by Bremsstrahlung (§1.1.1.1). Another source of photons is the electromagnetic decay of neutral pion in two γ-rays (Ackermann et al., 2013) (§1.1.1.4). These two types of emission are characterized by different spectra, but both are tracer of the coupling between interstellar medium and cosmic rays. In this way the correlation between the measured γ-ray emission with the large scale structure of our Galaxy can be explained.

The study of diffuse Galactic γ-ray emission provides direct information on the energy distribution of cosmic rays in various locations of the Galaxy which is needed to understand the origin and interactions of cosmic rays.

1.1.3   Discrete Emission

For "discrete" emission we mean all the individual γ-ray sources that are bright enough to be detected or close enough to be resolvable.

Not all the γ-ray emission shown in Figure 1.1 is due to interstellar medium: there are many discrete source of γ-ray emission over the sky. Pulsars, magnetars and supernova remnants are the more common stable γ-ray emitters. Emission in pulsar is due to their spin down energy (Cheng et al., 1986), in magnetars it is due to very intense magnetic field that power the emission (Kouveliotou et al., 1999) but the most powerful γ-rays emitters are distant Active Galactic Nuclei (AGN). The super-massive black hole at the center of such galaxies, thanks to the material that is accreted on it, provides an intense flux of charged particles. When those particles interact with gas and dust, they undergo various processes such as those discussed in §1.1.1, producing high energy photons, from X-rays to γ-rays.

Another example of transient sources that suddenly show up and very soon fade away are Gamma-ray bursts. GRBs are a frontier topic in γ-ray astronomy since the knowledge of the GRBs phenomenon is far from clear. Many studies and mission are focused on unveiling their nature and the physical processes that are involved. Since some of these mission proposals will be presented in the next chapter, a deeper description of the present knowledge about GRBs is given.

1.1.3.1 Gamma-Ray Bursts

Gamma-ray bursts (GRB) are short, intense, and non-repeating flashes of γ-rays. Characterized by with a wide range of spectral and temporal properties, GRBs are so bright that they can outshine all other γ-ray sources, making them easy to be detected with omnidirectional detectors. Their uniform projected distribution on the sky and their fluency distribution point to a cosmological origin (Hartman & Epstein, 1989). The light-curves of GRBs are quite variable from one burst to another. The shapes are different as are the timescales which can vary from few milliseconds to hundreds of seconds (Hurley 1989a). The time profile can be characterized by multiple peaks, repeated or not, or can be simple without showing any fine structure. Most of the GRBs light curves show two distinct emission phases: the *prompt* and the *afterglow*.

1.1.3.2 Prompt emission

The initial prompt phase lasts typically less than 100 s and releases, on the whole, an amount of energy equal to $\sim 10^{51}$ erg and seems to be composed of individual pulses, with a pulse being the "building block" of the overall light curve. The duration of the bursts spans five orders of magnitude, ranging from $0.01\,\text{s}$ to more than $100\,\text{s}$. Most prompt emission is highly variable, showing 100% variation in the flux on a time scale much shorter than the overall duration of the burst. The variability time scale, δt, is determined by the width of the peaks: δt is much shorter than the duration of the burst. Despite the broad diversity in their γ-ray emission properties (peak energy, spectral shape, variability timescale, duration), there is a bimodal distribution on their duration (Figure 1.4) allowing the distinction between short and long bursts
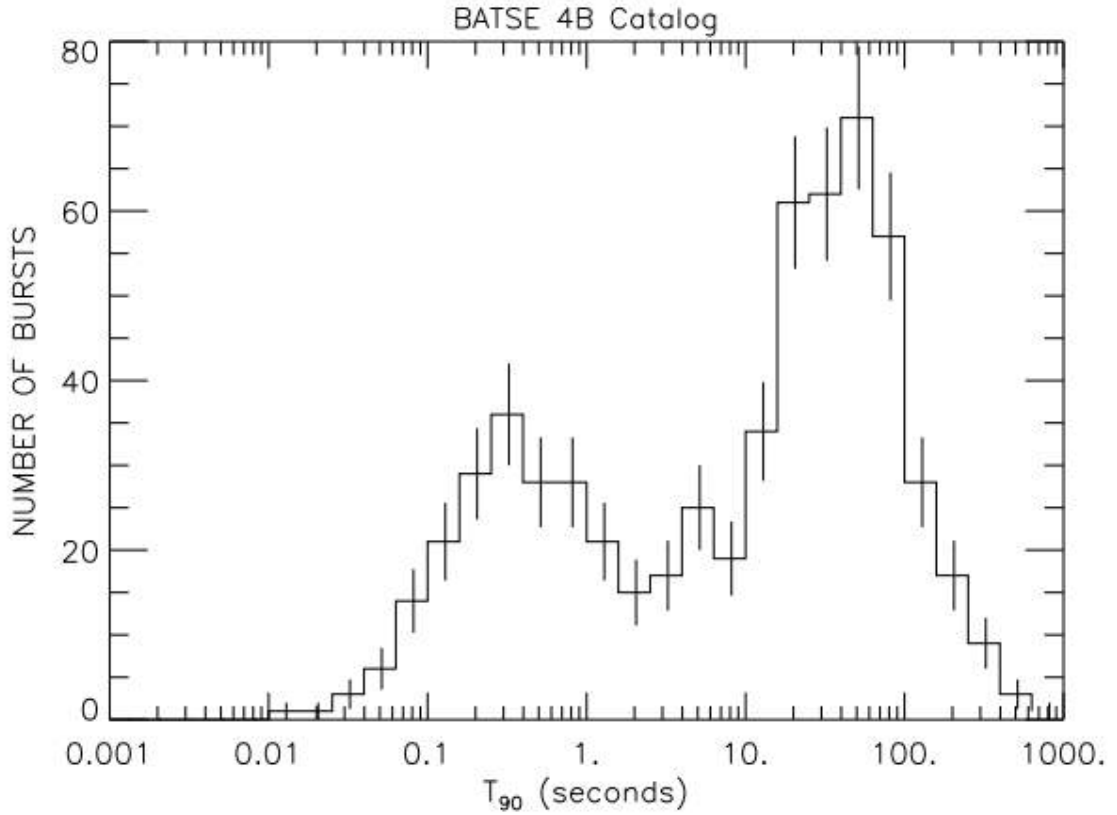
Figure 1.4:   *Distribution of the prompt duration for 2704 GRBs observed by CGRO/BATSE. The duration is expressed in terms of T_{90}, that is the time over which a burst emits from 5% to 95% of its energy. Figure from Meegan et al. (1996).*

(Kouveliotou et al., 1993).

Long GRBs   Long GRBs (LGRBs) are associated with the brightest regions of galaxies where the most massive stars lie. LGRBs observations range over different value of redshift, from $z = 0.0085$ (GRB 980425) to $z > 8$ (GRB 090423). LGRBs are extremely bright in both γ-ray prompt emission and multi-wavelength afterglow (described later in this section). They are the endpoints of the lives of massive stars and their rate is therefore approximately proportional to the star formation rate of the host galaxy.

Short GRBs   In contrast to LGRBs, SGRSs typically originate in host galaxies with a wide range of star formation properties, including low star formation rate. This indicates a different origin, and leads to think that SGRBs arise from an old population of stars possibly related to mergers of neutron star/black hole or neutron star/neutron star binary systems (Nakar, 2007).

Spectral properties   A GRB prompt spectrum is *non thermal*, which means that the particles that produce the emission are not in thermal equilibrium with their surrounding, and varies strongly from one burst to another. It can be spectrally modeled by two power laws joined smoothly at a break energy, the so-called *Band function*.

1.1.3.3   Afterglow emission

The afterglow is an emission that temporally follows the prompt. It has been discovered when Beppo-SAX activated the follow up to GRB 970228 (Costa et al., 1997). The afterglow emission spreads over the electromagnetic spectrum going from X-ray to radio through optical and IR and can last days to months (Nousek et al., 2006). The typical X-ray light curve is usually composed by four power laws $F_t \propto t^{\alpha_i}$ with different spectral index α_i. Flares may also be superimposed on the trend described above. The optical light curve is simpler than the X-ray light curve and is often modeled by a single power law.

Spectral properties   The origin of the afterglow spectrum is also non thermal, and its broadband nature is well described by synchrotron emission, although an inverse Compton component may also contribute to the X-ray afterglow (Sari et al., 1998). The X-ray afterglow is typically well fit by an absorbed power law with a photon index $\Gamma \sim 2.1$ and a column density of the order $10^{21} - 10^{22}$ cm^{-2}. Spectral evolution is sometimes observed.

1.1.3.4   Models

The current interpretation of the phenomenon of GRBs is likely to be related to the formation of a black hole, the large energy output being supplied by the gravitational energy liberated in the process. This energy is liberated in a very short time, and is thought to be due either by the collapse of the rotating core of a massive star in the case of long GRB, or, for short GRBs, by the merger of two compact stellar remnants, such as two neutron stars or perhaps a neutron star and a binary black hole, resulting in the disruption of the neutron star. In both cases, the physical phenomenon on which this emission is based should be similar. In the next paragraph the most accepted theoretical model is described.

GRB Fireball Model   Many different models were proposed since the GRBs discovery, most of them based on the view that these bursts result from energetic processes near a compact object. Cavallo and Rees, in 1978, laid the foundations of the currently most accepted GRBs mechanism model: the *fireball model*.

The fireball can be imagined as a radiation sphere of radius R and initial energy E_0. Inside the initial radius, the particles have a bulk Lorentz factor $\Gamma \propto 1$ and random isotropic velocities. If the initial temperature T is high enough, e^-e^+ pairs will form, and because of the opacity due to pairs the radiation cannot escape. The pair-radiation plasma behaves like a perfect fluid. The fluid expands under of its own pressure and, as it expands, it cools with $T \propto R^{-1}$. As the temperature drops below the pair-production threshold, the pairs annihilate. When the local temperature is around 20 keV the number of pairs becomes sufficiently small that the plasma becomes transparent and the photons escape freely to infinity. In the meantime the fireball is accelerated and is relativistically expanding outwards. Energy conservation require that the Lorentz factor, in this outward motion, satisfies $\Gamma \propto R$.

In addition to radiation and e^-e^+ pairs, baryonic matter is present and is accelerated with the rest of the fireball converting part of the radiation energy into bulk kinetic energy. The interaction of the baryons with the surrounding medium, taking place in relativistic shocks, allows the energy to be radiated away with a non-thermal

spectrum (Rees and Meszaros, 1992). The shocks taking place in the fireball model are both *internal* and *external.*

Internal shocks will appear within a relativistic wind produced by a highly variable source. If the Lorentz factor of the wind is variable, successive shells will have different relative velocities. Hence a fast shell injected after a slower one can eventually catch up and collide with it, giving birth to internal shocks. The electrons accelerated in these shocks emit synchrotron radiation in the presence of magnetic fields. Each shock produces its own emission and the resulting prompt emission (spectrum and variability) is the addition of simultaneous emission from multiple shocks.

The afterglow emission is generated in an external shock. External shocks must occur when the relativistic ejecta has swept up a sufficient amount of surrounding interstellar medium, to slow down (Rees and Meszaros, 1992). For an ejecta of baryon mass M_{ej}, with a Lorentz factor of Γ_0, this occur when the amount of swept up mass is $M_{\mathrm{sw}} \simeq M_{\mathrm{ej}}/\Gamma_0$. Particles scattered across the shock interface will be accelerated to a relativistic velocity, leading to non-thermal synchrotron and IC radiation (Rees and Mészáros, 1993; Meszaros et al., 1993).

1.2   A brief history of gamma-ray astronomy

In the following a brief history of γ-ray astronomy is presented, from the first satellite to the missions still operating. Since the historical overview covers also the technological evolution, in which this thesis fits, a detailed description of the various detector working principles will be given in Chapter 3.

Long before they could detect astronomical γ-rays, scientists suspected this type of radiation was produced throughout the Universe. To identify this high-energy emission, Earth-bound detectors needed to be placed outside our atmosphere, which typically absorbs γ-rays. On 27 April 1961, the Explorer XI satellite carried the first γ-ray instrument into Earth's orbit. This date could be considered the one in which the γ-ray astronomy was born.

Explorer XI (Figure 1.5a) was the first satellite dedicated to γ-ray astronomy.

Placed in an elliptic orbit around Earth, the satellite searched for the signs of cosmic-ray interaction with interstellar material. A sandwich crystal scintillator (CsI and NaI) and a Lucite Cherenkov counter, surrounded by a plastic anti-coincidence scintillator, was put on board to detect γ-rays above 50 MeV. The satellite operated until early September, when power supply problems became noticeable. Over a period of 23 days, 9 hours of useful data were collected, containing information on 22 γ-rays and 22,000 events due to charged cosmic rays.

As often happens, one of most important discovery for γ-ray astronomy was serendipitous. A military defense system, the Vela satellites, was launched in Earth orbit by USA, after a treaty banning nuclear atmosphere tests in 1963, to monitor clandestine Russian nuclear activity. In 1967, Vela detected the first fast and intense Gamma Ray Burst coming from the outer space. However, because of the secret nature of the satellite program the detections were not publicly reported until 1973.
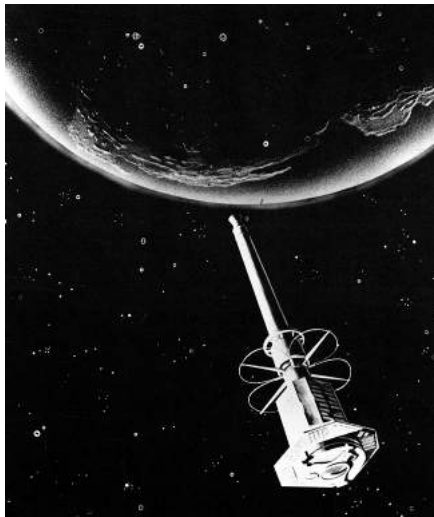
(a)   (b)

Figure 1.5: *(a) An artistic illustration of Explorer 11. Source: HEASARC GSFC NASA.*
(b) NASA Compton Gamma Ray Observatory (CGRO). Source: HEASARC GSFC NASA

A year before, in 1972, NASA launched the Small Astronomy Satellite 2 (SAS-2) with an on board instrumentation made of a wire spark-chamber that covered the energy band between 20 MeV and 1 GeV. Even if not provided with a high resolution,

SAS-2 allowed to obtain the first map of the sky at γ-rays frequencies. It helped to identify the presence of discrete γ sources, although their exact location was made difficult by the low instrumental resolution.

The first satellite to provide a detailed view of the Universe in γ-ray was also the first one sent on orbit by the newborn European Space Agency (ESA) in 1975: COS-B. It carried a single large experiment, the Gamma-Ray Telescope, a spark chamber γ-ray detector covering the energy range from $\sim$30 MeV to 5 GeV, and a 2–12 keV proportional counter mounted on the side of the γ-ray detector.

The '90s were a turning point for γ-ray astronomy: satellites began to be provided with wide field instrumentations, able to give a better angular resolution. In 1991, USA launched the first orbiting satellite fully dedicated to gamma astronomy: the Compton Gamma-Ray Observatory (CGRO) (Figure 1.5b), with its four instruments: the Imaging COMpton TELescope (COMPTEL), the Oriented Scintillation Spectrometer Experiment (OSSE), the Burst And Transient Source Experiment (BATSE), and the Energetic Gamma Ray Experiment Telescope (EGRET). CGRO was able to cover an unprecedented six orders of magnitude in energy from 30 keV to 30 GeV. COMPTEL consisted in two detector arrays, made of a liquid scintillator and NaI crystals. γ-ray are revealed by two successive interactions, in the liquid scintillator a γ-ray undergoes Compton scattering and then is totally absorbed in the solid scintillator. Location of interaction and energy losses are both measured. Scintillation light is read and amplified by photomultiplier tubes (PMTs) coupled with the crystals. OSSE allowed observations of a γ-ray source to be alternated with observation of nearby background regions thanks to four NaI scintillation detectors, sensitive to energies from 50 keV to 10 MeV, where each detectors could be individually pointed. The primary objective of BATSE was to study the phenomenon of GRBs, although the detectors also recorded data from pulsars, terrestrial γ-ray flashes, soft gamma repeaters, black holes and other exotic astrophysical objects. BATSE was made up by eight uncollimated detector modules. Each detector contained two NaI(Tl) scintillation detectors: a Large Area Detector (LAD) and a Spectroscopy Detector (SD). The LAD detector was a disk of NaI mounted on a layer of quartz. A light collector housing on each detector brings the scintillation light

into three photo-multiplier tubes (PMTs) and the signal is summed at the detector; instead, SD was an uncollimated NaI(Tl) scintillation detector directly coupled to a PMT. The last instrument on board was EGRET. It was designed to cover the energy range from 20 MeV to about 20 GeV. The instrument used a multilevel thin-plate spark chamber system to detect γ-rays by electron-positron pair production process. A NaI(Tl) calorimeter was placed beneath the instrument to provide good energy resolution over a wide dynamic range. The entire instrument was covered by a plastic scintillator anti-coincidence dome to prevent triggering on events not associated with γ-rays.

Thanks to all these instruments, CGRO achieved many important scientific goals like mapping the Milky Way using the 26 Al γ-ray line, the discovery of the "Bursting Pulsar" (Kouveliotou et al., 1996) and the discovery of the isotropic distribution of the GRBs events (Kouveliotou et al., 1993). CGRO ended its mission with a controlled re-entry on June 4th, 2000.

In October 2002, INTEGRAL (Figure 1.6) was launched. The scientific goals of the INTERnational Gamma-Ray Astrophysics Laboratory were addressed through the use of high-resolution spectroscopy with fine imaging and accurate positioning of celestial sources in the soft γ-ray domain. Its payload consists of three instruments: a Spectrometer (SPI) and a Imager (IBIS) differently optimized in order to complement each other. While the spectrometer is designed for high resolution spectroscopy in the 18 keV – 9 MeV energy range of γ-ray emission lines with a relatively low spatial resolution (2.5°), the imager is dedicated to imaging of point sources with a spatial resolution of 12′.

Five years later (2007), it was the turn of Astrorivelatore Gamma ad Immagini LEggero (AGILE), an Italian Space Agency (ASI) mission. It is the first of a new generation of high-energy space missions based on solid-state silicon technology combining for the first time two sophisticated co-axial instruments: a γ-ray detector, sensitive to photons with energy in the range of 30 MeV – 50 GeV, and a hard X-ray detector, sensitive in the range 18 – 60 keV. The instrument is completed by a calorimeter (energy range 250 keV–100 MeV) and by an anti-coincidence system. Its angular resolution, 0.1°–0.2° in γ-rays and 1-2 arcmin in X-rays, the very large field
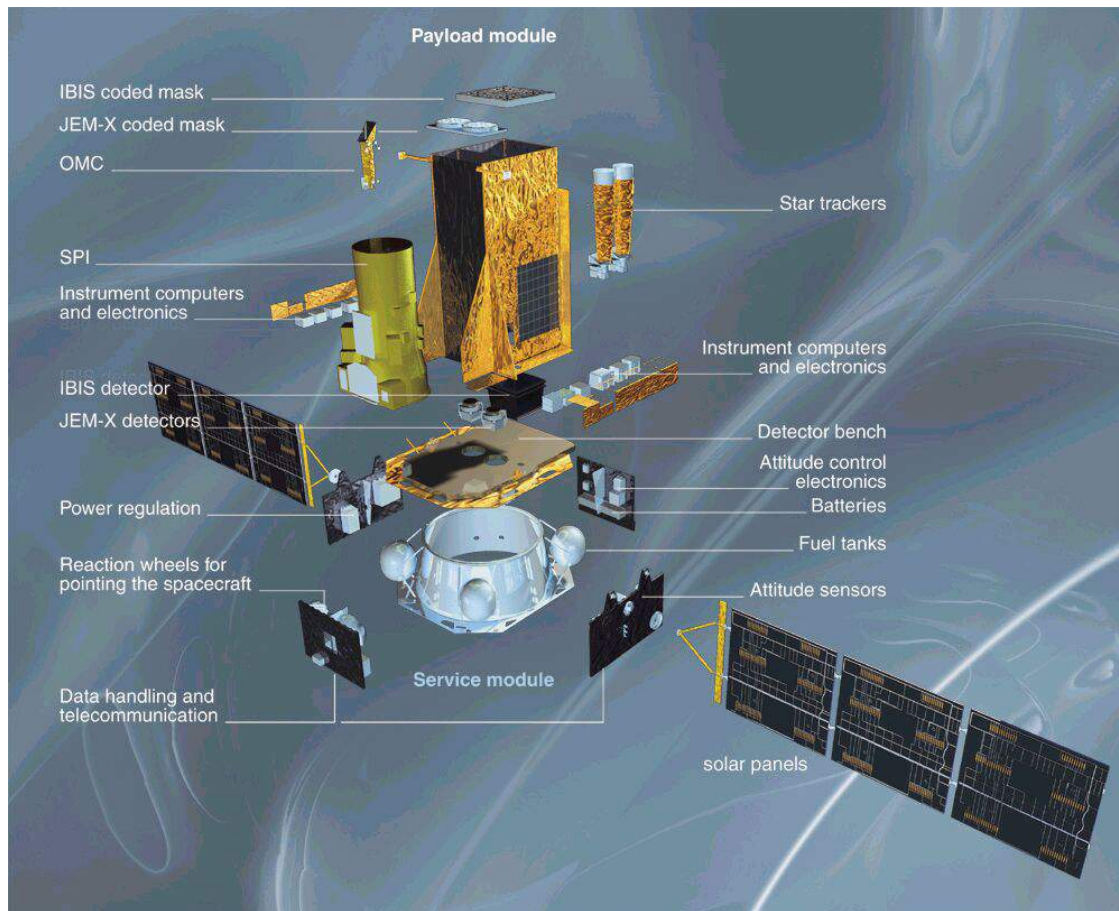
Figure 1.6: *Exploded diagram of the INTEGRAL spacecraft. Credits to ESA. Illustration by Medialab*

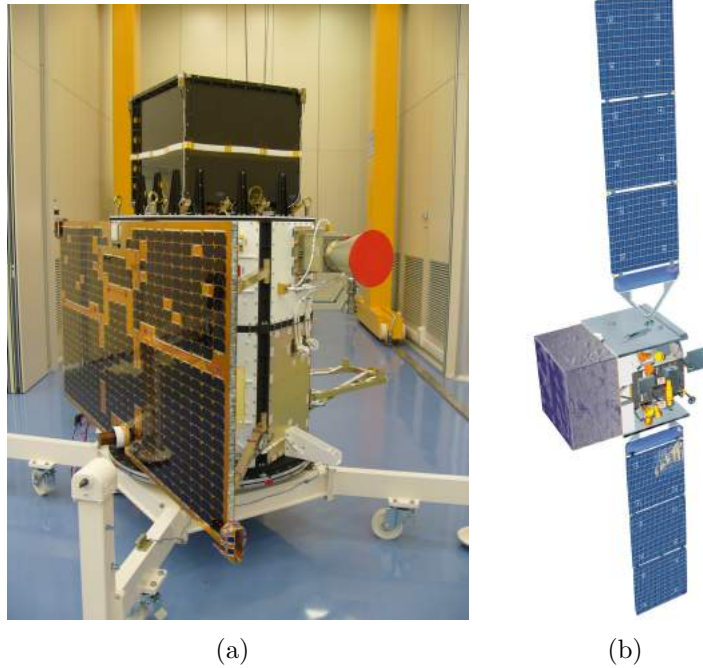(a)   (b)

Figure 1.7: *(a) Agile within the clean room of Gavazzi Space at Tortona.   Credits to Media Inaf (b) Artist rendering of the Fermi Gamma-ray Space Telescope.   Credits: NASA/Sonoma State University/Aurore Simonnet.*

of view as well as its small dead time (100 μs), makes AGILE a very good instrument to study persistent and transient γ-ray sources.

The latest γ-ray dedicated mission is Fermi (Figure 1.7b), formerly called the Gamma-ray Large Area Space Telescope (GLAST), launched in 2008 and still operating. The main instrument on board is the Large Area Telescope (LAT), a imaging high-energy γ-ray telescope covering the energy range from about 20 MeV to more than 300 GeV, with a field of view that covers about 20% of the sky. The Gamma-ray Burst Monitor (GBM) is the other Fermi's instrument, it is made up by two sets of detectors: twelve NaI scintillators and two BGO scintillators. The first ones are sensitive in the lower end of the energy range, from a few keV to about 1 MeV and provide triggers and locations. The BGO detectors, instead, cover the energy range from 150 keV to 30 MeV, providing a good overlap with the NaI at the lower end

and with the LAT at the high end. Fundamental for detecting transient phenomena such as GRBs, is to scan frequently as much sky as possible.

For more than eight years, the international Fermi Gamma-ray Space Telescope has surveyed the entire gamma-ray sky, vastly increasing our knowledge of the high-energy Universe. This survey has included both Galactic sources like pulsars, supernovae remnants and high-mass binaries and extragalactic objects like starburst galaxies and active galactic nuclei (AGN).

This digression on the history of γ-ray astronomy shows how its birth and development is strictly tied with the technology used. Today this bound is stronger than ever: new devices and techniques are developed in order to expand the existing knowledge of the high-energy Universe and to discover new phenomena.

Chapter 2

The new frontier of γ-ray satellites

The use of γ-ray detectors made of scintillator crystals coupled with Silicon Drift Detectors, similar to the one under investigation in this thesis, is a very promising technology that is spreading rapidly in the γ-ray astronomy field. Indeed, many missions propose a payload based on this type of technology. Detection, spectroscopy and timing on a broad energy band, combining a low-energy threshold (1–2 keV) and energy resolution for the X-rays events significantly better than any other detection system based only on scintillators (Campana et al., 2016) are the reasons why a large part of the scientific community is supporting this technology.

In this chapter some space missions proposed for the next decades which heavily rely on such a technology will be described, with their scientific goals and instrumentation. These missions, THESEUS, HERMES and e-ASTROGAM, represent the future towards the γ-ray astronomy is heading. Differences in the payload and scientific objectives demonstrate the extreme flexibility of the technology treated in this work in adapting to different applications.

2.1   THESEUS

THESEUS (Transient High Energy Sources and Early Universe Surveyor) is a mission project candidate to the Medium-size mission opportunity in ESA's Cosmic Vision

Program[1] M5. The project is supported by an international consortium with main participation of UK, Spain, Denmark, Czech Republic, USA, France and Hungary (Lead proposer: Lorenzo Amati, INAF/IASF-BO).

2.1.1   Scientific Case
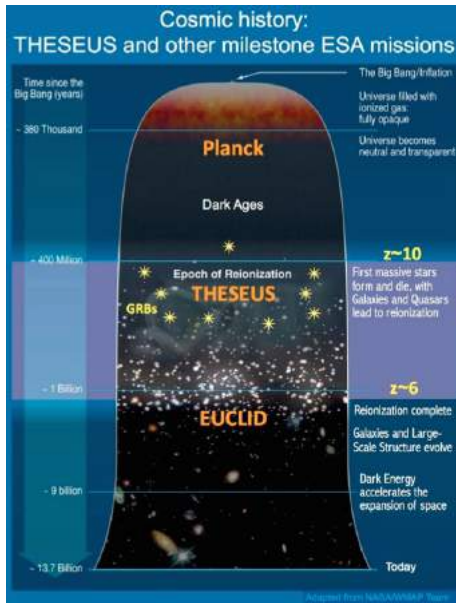
Figure 2.1: *The observation limit, in terms of redshift, of THESEUS compared to the Planck's and Euclid's ones.*

Because of their huge luminosities, mostly emitted in X and gamma-rays, their redshift distribution, extending at least to $z \sim 10$, and their association with explosive death of massive stars, GRBs are unique and powerful tools for cosmology. In particular, GRBs represent a unique tool to study the early Universe up to the re-ionization era. The history of the Universe between recombination of hydrogen at very high z and the formation of the first quasars and stars (the so-called "Population III" or POP III stars) is poorly known. This period has been called the 'dark ages'. The first light from stars ended this period and heated the interstellar medium, reionizing the entire Universe (Barkana and Loeb, 2001). GRBs allow to investigate the environment and the properties of the host galaxies from the study of their emission lines which can be observed when the afterglow has faded away (Sokolov et al., 2001).

Our understanding of GRBs is defective and incomplete. Many of the still open issues preventing the understanding of these phenomena can be addressed only by broad band sensitive measurements of the prompt emission from several MeVs down to 1 keV. A such extended energy band down to soft X-rays is of key importance for

---

[1]http://sci.esa.int/jump.cfm?oid=56198

several reasons: testing the prompt emission models, studying the properties of the circum-burst environment via the detection of transient absorption features, investigating X-Ray Flashes (XRFs, which can constitute the bulk of the GRB population) and contributing to increase the detection rate of high-redshift GRBs.

The primary scientific goals of the mission are to explore the early Universe by unveiling the GRBs population in the first billion years and to perform an unprecedented deep survey of the soft X-ray transient Universe. Observing GRBs up to $z \sim 10$–12 provides a huge amount of information, not only on the Star Formation Rate (SFR) of massive stars, but also on the presence of the first population of stars. Even the James Webb Space Telescope (JWST) would be unable to identify Pop III stars but, since these elusive objects are believed to end their lives with high energy GRBs, these high energy photons would be detectable by THESEUS which will allow also to study very faint host galaxies that could not be detected in absence of GRB.

To successfully achieve these such challenging results, an instrumentation able to cover a wide energy range is required, allowing to detect those GRB whose emission is shifted towards lower energies because of their cosmological distance. Such instrumentation qualifies not only to GRBs observation but also to investigate a wide variety of astronomical phenomena, from AGN to SNs, from Pulsars to Tidal Disruption Events (TDEs) and Magnetars.

2.1.2 Mission payload

Given the THESEUS scientific goals, its payload is studied to be very sensitive in a broad energy band, from the IR to the X/γ, it is composed of three instruments

- Soft X-ray Imager (SXI);

- InfraRed Telescope (IRT);

- X-Gamma-rays Spectrometer (XGS);

Soft X-ray Imager   The THESEUS *Soft X-ray Imager* (SXI) comprises 5 modules. Each module is a wide field Lobster Eye telescope, using the optical principle first

described by Angel (1979). The optics aperture is 290×290 mm^2 formed by a 7×7 array of square pore Micro Channel Plates (MCPs). The MCPs are 40×40 mm^2 and are mounted on a spherical frame with radius of curvature 600 mm. The focal plane of each module is provided by 4 back illuminated CCD. Each CCD has dimensions 61×61 mm^2 which, with a focal length 300 mm, gives an active area of 135.7 square degrees for each module. The total active area is 542.8 square degrees. Thus, a suit of 5 SXI modules has a total field of view of 2714 square degrees. The SXI will cover the energy band from 0.3 to 5 keV.

InfraRed Telescope The *InfraRed Telescope* (IRT) on board THESEUS is designed to identify, localize and study the afterglows of the bursts detected by the SXI. The telescope is a Cassegrain with a 0.7 m aperture and 0.23 m for secondary mirror. It is made of SiC for both optics and optical tube assembly. SiC is a material that has been used in other space missions (such as Gaia, Herschel, Sentinel 2 and SPICA). The detector is a Charge-Coupled Device (CCD), the Hawaii-2RG 2048×2048 pixels (18 μm each) produced by Teledyne.

IRT is designed not only to identify, localize and study the afterglows detected by the SXI but also to observe GRBs over a wide range of redshift, since high-z ones will be detected to larger wavelength due the cosmological redshift.

X-Gamma-rays Spectrometer X-Gamma-ray Spectrometer (XGS) is the instrument that exploit the same technology under investigation in this work. It is based on units made of a scintillation bar (CsI(Tl)) where each end of the bar is coupled with a SDD for the read-out of the scintillation light, while the other sides of the bar are wrapped with a light reflecting material convoying the scintillation light towards the SDDs. In this particular architecture, the SDD on the side that faces the photon entrance window is operated both as solid state detector for low energy X-ray photons interacting in Silicon and simultaneously as read-out system of the scintillation light resulting from hard–X or γ-ray interactions in the scintillator. The bottom SDD at the other end of the crystal bar operates only as a photo-device.
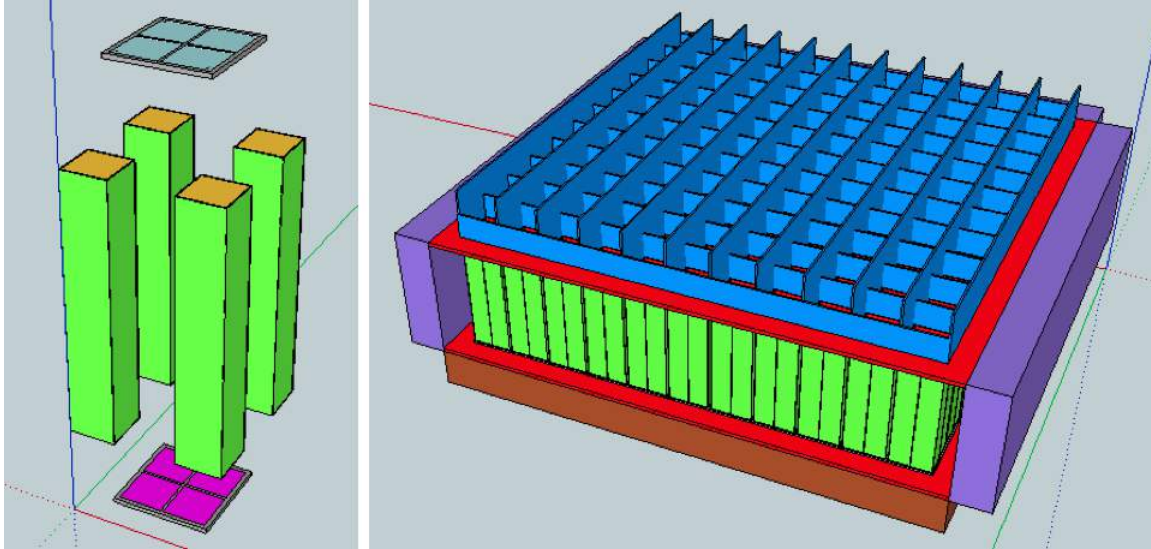
Figure 2.2: *Left: Exploded view of 4 CsI(Tl) scintillator bars optically coupled to an array of SDDs. Right: Sketch of the module, including the collimator limiting the module FOV (blue) and the lateral and bottom electronics boxes (violet and brown); the front box has been removed.*

As shown in Figure 2.2, crystals are tightly packed in an array of 22×22 elements to form the module. The face of the module exposed to the sky is surmounted by a collimator limiting the field of view (FOV) of the detector up to ∼200 keV; in such way the FOV is about 100°×60° matching the SXI detectors FOV. XGS will cover a wide energy range, from 2 keV up to 20 MeV with a sensitivity and effective area that are shown in Figure 2.3.

2.2 HERMES

HERMES stands for High Energy Rapid Modular Experiment Scintillator. The project is in a preliminary study phase and has been supported by ASI for a technological research and development activities (PI: Luciano Burderi, University of Cagliari)

(a)   (b)
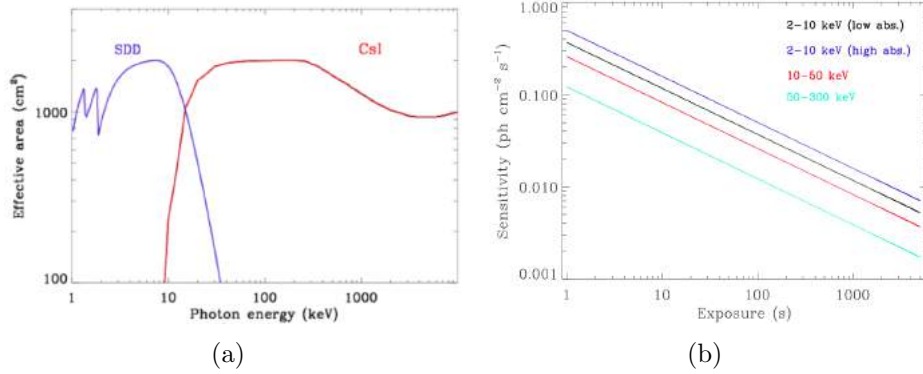
Figure 2.3: *(a) FOV averaged effective area of the XGS SDD and CsI detecting planes (b) XGS sensitivity as a function of exposure time in different energy bands. For the 2–10 keV energy band two values of the absorption column in the source direction were assumed: $N_H = 5 \times 10^{20}$ cm^{-2} and 10^{22} cm^{-2}*

2.2.1 Scientific case

Many theories, such as the *Loop Quantum Gravity*, predict a discrete structure for space-time on small scales, at about the *Planck length*, $L_P = 1.6 \times 10^{-33}$ cm. The key element of the theory of Special Relativity is the Lorentz invariance: all observers measure the same speed of light in vacuum, independent of photon energy, which is consistent with the idea that space is a three dimensional continuum. If the space is discrete on very small scales, it is conceivable that light propagating in this lattice exhibits a dispersion relation, in which the speed of photons depends on their energy. This has supported the idea that Lorentz invariance might break near the Planck scale (Wheeler *et al.*, 1998).

If minuscule variations in the speed of photon occurs, the further the source is, the more the tiny variation can be accumulated and be detected. The ideal candidates to verify these theories are very energetic sources at cosmological distance. The GRBs qualify as the ideal tools to test these effects of space-time quantization, by observing their lightcurves in different energy bands (Amelino-Camelia et al., 1998), since tiny quantum-spacetime effects modifying light propagation scale with the distance of the GRB, they can be separated from other kind of spectral delays caused by physics of the emission mechanism.

The main purpose of the mission is to detect the lattice-like structure of the space-time, investigating the lags between spectral components of the prompt emission of GRBs in order to clarify the emission mechanism that is still far from clear, and to investigate the most impulsive events that suddenly brighten the X/γ ray sky with a wide spectral band and unprecedented temporal resolution.

2.2.2 Mission payload

To fulfill the mission goals, timing performances have the priority in designing the detector, but also a good spectroscopic performance needs to be achieved. The detection of X-ray and γ-ray radiation considered in this project is achieved by a two-step conversion of the photon energy to visible light in a scintillation material and the visible photons to the electric charge in a photo-detector. In order to extract as accurately as possible information about the time of occurrence of the radiation detection and of its energy, both the scintillator and the photo-detector should have a fast, low noise response. For this reason, the detector, shown in a schematic representation in Figure 2.4, will be composed by a fast scintillator crystal, such as LaBr$_3$(Ce), and a combination of

Figure 2.4: *A schematic representation of a single element of the HERMES detector*

silicon photomultiplier (SiPM) and SDD operating in parallel. A small SiPM can be used just to deliver a fast trigger for timing while the SDD is used for good energy resolution, and to validate the SiPM trigger. Except for the presence of the SiPM, the architecture on which this basic unit is designed is the same of the prototype tested in this thesis.

Since also source position measurements are fundamental for this project, HERMES is designed as a modular experiment in which each unit is composed of 100

"Plug&Play"Modules. Each module has an effective area of 100 cm^2, a weight of 5–10 kg, energy band from 10 keV to 30 MeV, energy resolution of 15% at 30 keV, temporal resolution of 2–4 ns.

The units can be arranged in a suitable configuration on board of the International Space Station (ISS) in order to have baselines between detectors of the order of ten meters, performing by triangulation of the signal measured, a fast source position measurement. Another option is represented by the use of a micro satellite system such as *CubeSat*^{2}. The modules can be placed inside the micro satellite and sent to different orbits. This also represent a low cost solution (cost of about some tens of thousands of euro for each satellite launch) that will allow to use baselines enormously longer than the one on board of the ISS, achieving a much higher precision position measurement.

2.3   e-ASTROGAM

e-ASTROGAM is also an M5 mission candidate. At variance with respect to the other two missions, that focus on specific research themes, e-ASTROGAM is proposed as an observatory to investigate the high-energy Universe (PI: Alessandro De Angelis, University of Udine)

2.3.1   Scientific Case

The scientific themes that e-ASTROGAM aims at studying in deep can be grouped in three main areas:

- Matter and antimatter in our Galaxy and beyond;

- Accelerators in the nearby and distant Universe;

- Fundamental Physics and new messengers.

---

^{2}http://www.cubesat.org/

e-ASTROGAM aims to study the nuclear enrichment in our Galaxy related to SN activity and star formation exploring deeper the physics of Type Ia and core-collapse supernovae and their possible responsibility for cosmic-ray acceleration by performing observation in the MeV range star forming regions, massive stars, supernovae, Galactic novae together with their occasional GeV emission. The recent detection of the 847 keV line from the Type Ia SN 2014J in the starburst galaxy M82 by INTEGRAL (Churazov et al., 2014) represents the first of such measurements and raises a series of questions regarding the explosion mechanism and the scenario of Type Ia SNe. e-ASTROGAM is expected to detect several Type Ia SNe in the nearby universe in 3.5 years of operations.

It also will be capable to detect polarization in the MeV range and above 100 MeV. This information will be crucial for a variety of investigations including the study of compact objects, the magnetic field structure in jets and the emission mechanism during the different phases of GRBs.

A wealth of recent data on Galactic and extragalactic sources suggest the existence of particle acceleration mechanisms more efficient than the traditional Fermi-like diffusive processes. e-ASTROGAM will investigate the signatures of magnetic field reconnection at the crucial transition between quasi-thermalized and non-thermal accelerated distributions. The puzzling gamma-ray flares from the Crab Nebula and similar rapid phenomena in extra-galactic jets require non-ideal magnetohydrodynamics mechanisms in need of crucial data in the MeV range. Studies of rotationally-powered pulsars, magnetars, and pulsar wind nebulae will also greatly benefit from data collected in the 1–100 MeV range.

e-ASTROGAM will operate in the presence of next-generation detectors of gravitational waves and neutrinos. The multi-messenger nature of the emission will provide unique diagnostics for the study of gravitational collapse, particle acceleration and emission at the highest energies. Among the most interesting sources, GRBs will be copiously detected by e-ASTROGAM.

2.3.2 Mission payload

The e-ASTROGAM payload is shown in Figure 2.5. It consists of three main detectors:

- A *Silicon Tracker* in which the cosmic gamma rays undergo a first Compton scattering or a pair conversion, based on the technology of double sided Si strip detectors to measure the energy and the 3D position of each interaction with an excellent energy and spatial resolution;

- A 3D-imaging *Calorimeter* to absorb and measure the energy of the secondary particles.

- An *Anticoincidence* (AC) system to veto the prompt-reaction background induced by trapped, solar, or cosmic-ray charged particles, design with plastic scintillators covering the instrument to detect single charged relativistic particles with an efficiency exceeding 99.99%.
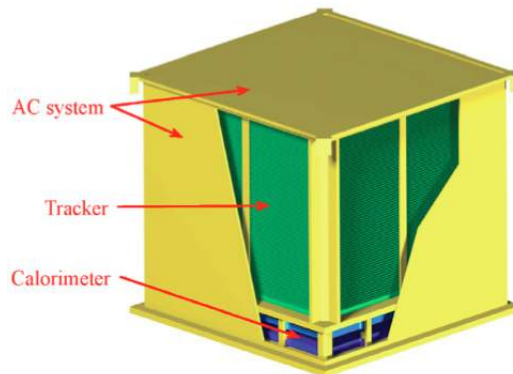
Figure 2.5: *Overview of the ASTROGAM payload showing the Silicon Tracker, the Calorimeter and the Anticoincidence system.*

The e-ASTROGAM **Calorimeter** is a pixelated detector made of a high Z scintillation material, the CsI(Tl), for an efficient absorption of Compton scattered gamma rays and electron-positron pairs. It consists of an array of 12,544 parallelepiped bars of CsI(Tl) of $5\times5\times50$ mm^3 dimension, readout by silicon drift detectors at both

ends. Depending on the available cost, the use of $LaBr_3(Ce)$ for its spectroscopic and temporal properties can be evaluated with respect to the baseline CsI(Tl) crystal. In this case, even more than in the case of HERMES, the architecture of the detector is similar to XGS, from which it differs for the absence of direct X-ray detection.

Interactions of photons with matter in the e-ASTROGAM energy range is dominated by Compton scattering and by electron-positron pair production. e-ASTROGAM maximizes its efficiency for imaging and spectroscopy of energetic gamma rays by using both processes. Figure 2.6 shows representative topologies for Compton and pair events. For Compton events, point interactions of the gamma ray in tracker and calorimeter produce spatially resolved energy deposits, which have to be reconstructed in sequence using the redundant kinematic information from multiple interactions. Once the sequence is established, two sets of information are used for imaging: the total energy and the energy deposit in the first interaction measure the first Compton scatter angle. The combination with the direction of the scattered photon from the vertices of the first and second interactions generates a ring on the sky containing the source direction. Multiple photons from the same source enable a full deconvolution of the image, using probabilistic techniques. Pair events produce two main tracks from the electron and positron at small opening angle. Tracking of the initial opening angle and the plane spanned by electron and positron enables direct back-projection of the source.
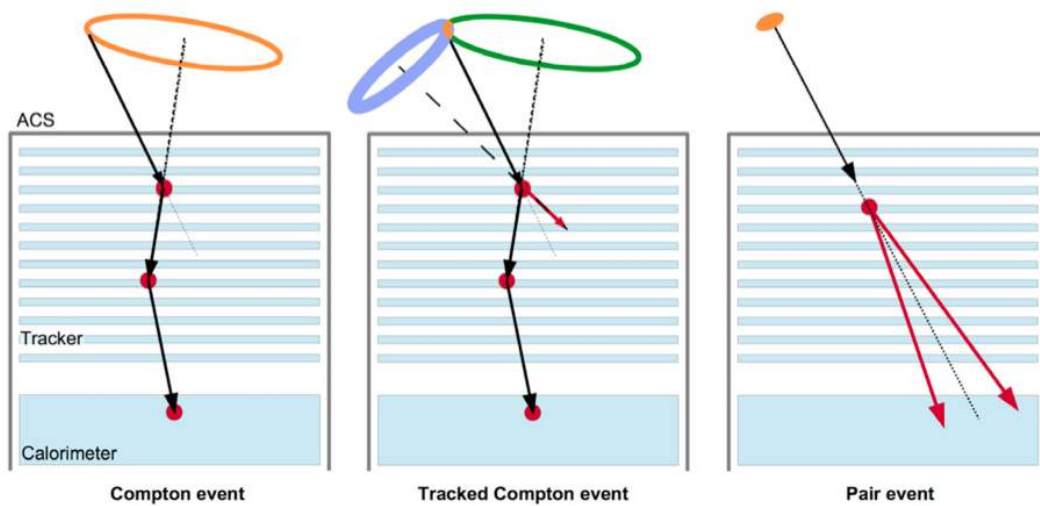
Figure 2.6: *Representative event topologies for Compton events without (left) and with electron tracking (center) and for a pair event (right panel).*

Chapter 3

Gamma-ray detectors

In order to emphasize the choices made in the design of the prototype under consideration and its differences from alternative technologies, in this Chapter a brief overview of the most common detectors, their working principles and characteristics are given.

To reveal γ-rays it is necessary to detect their interactions with matter which results in full or partial energy transfer from the incident photon to electrons or nuclei of the detector atoms. The detection is therefore based on energy losses: the detectors which are used to detect γ-rays are usually sensitive also to particles, even if the interaction mechanisms could be different. The interaction between photons, particles and matter is not a deterministic processes but different modes of interaction are possible depending on the energy of the incoming radiation. The following description is based on Knoll (2010) and Leo (1994).

Photoelectric effect Given an incoming photon of energy $h\nu$, it may undergo an interaction with an atomic electron. If the energy $h\nu$ is equal or larger than the electron binding energy, it can be fully absorbed and, as shown in Figure 3.1, the photoelectron is ejected from its atomic shell with a kinetic energy given by $E_{\rm kin} = h\nu - E_b$ where E_b is the binding energy, that is the amount of energy needed to ionize the atom. The probability of the photoelectric effect to occur is measured by the cross section of the process $\sigma_{\rm ph}$ that is a function of the atomic number Z and
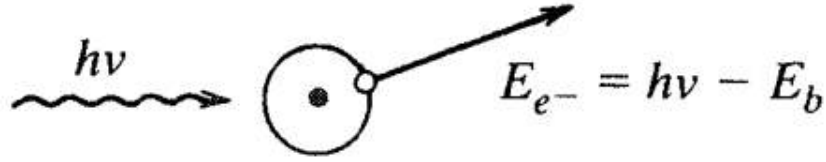
Figure 3.1: *Schematic representation of the physical mechanism of the photoelectric effect. Figure from Knoll (2010).*

the photon energy E

$$\sigma_{\mathrm{ph}} \propto \frac{Z^n}{E^3} \tag{3.1}$$

where n is a number that varies between 4 and 5 (Evans). This effect is the most efficient for low energy photons. For higher photon energies, the cross section of the photoelectric effect become smaller and the *Compton scattering* process become significant.

Compton scattering   In this type of interaction, only part of the photon energy is absorbed by the electron which is recoiled (assumed to be initially at rest). Since both energy and momentum are conserved in this interaction, the incoming γ-ray and the recoil electron are scattered by an angle θ and an angle ϕ, respectively, defined from the initial trajectory of the γ-ray (Figure 3.2). The energy of the photon after the interaction is given by

$$h\nu' = \frac{h\nu}{1 + \frac{h\nu}{m_e c^2}(1 - \cos\theta)} \tag{3.2}$$

where $m_e c^2$ is the rest-mass of the electron.

For a single photon, more than one Compton event is possible if the energy of the scattered photon is enough to undergo successive interactions. As a first approximation, the probability of Compton scattering per atom of the absorber depends on the number of electrons available and therefore increase linearly with the atomic number Z of the material.
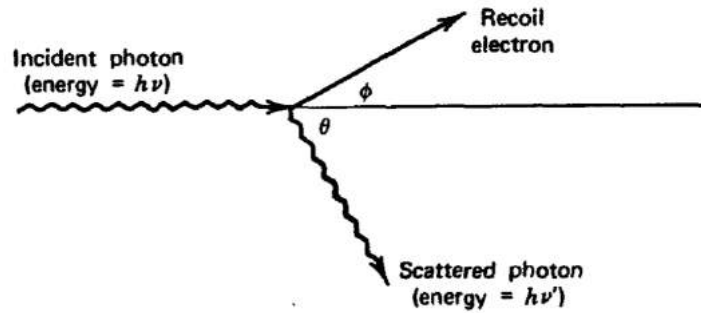
Figure 3.2: *Sketch of the Compton scattering that shows the photon before and after the interaction. Figure from Knoll (2010).*

Pair production   At 1.022 MeV, the pair production process is energetically allowed but it is usually negligible until several MeV. The energy limit of 1.022 MeV for pair production is due the minimum energy needed to convert a photon into a e^-e^+ pair. Since the electron and positron rest energy is 0.511 MeV, when a γ-ray has an energy of more than twice the rest-mass of an electron and is near an atomic nucleus, it can be transformed in a e^-e^+ pair: $\gamma \rightarrow e^- + e^+$. Since the energy of the process is conserved, the excess energy carried by the photon is converted into the kinetic energy of the two particles. This interaction also involve the nearby nucleus in order to satisfy conservation of momentum. For this reason, the nucleus receives some recoil. The cross section of the pair production is formally derived by quantum electrodynamics but, to simplify, can be written as:

$$\sigma = \alpha r_e^2 Z^2 P(E, Z) \tag{3.3}$$

where α is the *fine structure constant*, r_e is the electron radius and $P(E, Z)$ is a function that depends on energy and atomic number.

Figure 3.3 reports the three described processes and shows which is the dominant process at a given energy and atomic number.

High Z material are the best to exploit photoelectric effect but this is inefficient in detecting photons with energy higher than 1 MeV. For the most energetic photons ($>$ few MeVs), pair production is the dominant process over a wide range of Z. The Compton scattering, instead, is the most likely for a large energetic range for very
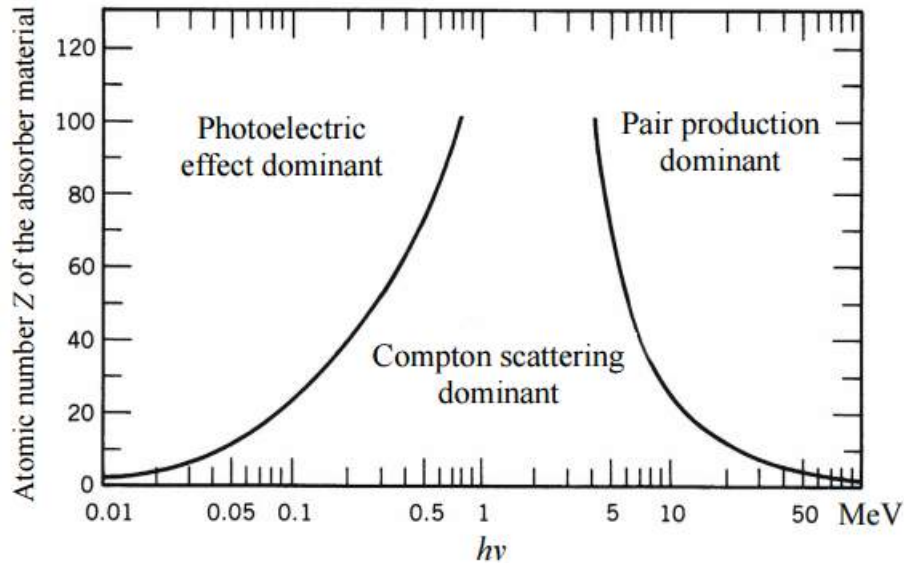
Figure 3.3: *The relative importance of the three major types of γ-rays interaction for typical hard X rays/ low γ photons. The lines represent the energy and Z values for which the processes have the same probability to occur. Figure from Knoll (2010).*

low Z material. At higher Z values, it keeps its dominance on the other two processes only in an energetic range from almost 1 MeV to several MeV.

Ionization energy losses   Interaction of photons with matter can be considered point like. Particles, instead, interact in a continuous manner through two electromagnetic processes: *elastic collisions* with the nuclei of the material and *inelastic collisions* with atomic electrons. In the first, very little energy is transferred since the mass of the nuclei of most materials are usually large compared to the incident particle mass. In the latter process, the energy is transfered from the particle to the electron causing an excitation or a ionization of the material. The amount of energy transfered in each collision is generally a very small fraction of the particle total energy; however, in normally dense matter, the number of collisions per unit path length is so large that a substantial cumulative energy loss is observed even in relatively thin layers. The average energy loss per unit path length is often called *stopping power* and its expression was first derived by Bethe, Bloch and other

authers:

$$-\frac{dE}{dx} = K\rho\frac{Z}{A}\frac{z^2}{\beta^2}\left(\ln\frac{2m_ec^2\gamma^2v^2W_{\text{Max}}}{I^2} - 2\beta^2 - \delta - 2\frac{C}{Z}\right) \qquad (3.4)$$

where ρ, A and Z are the density, the mass number and the atomic number of the target material, respectively, z and v are the charge and the velocity of the incident particle, I the mean excitation potential, W_{Max} is the maximum energy transferable for each collision and δ and C are the *density* and *shell* correction terms. The density effect arises from the fact that the electric field of the particle also tends to polarize the atoms along its path causing a shielding from the full electric field intensity of the electrons far from the path of the interacting particle. Collisions with these outerlying electrons will therefore contribute less to the total energy loss. The shell correction accounts for effects which arise when the velocity of the incident particle is comparable or smaller than the orbital velocity of the bound electrons.
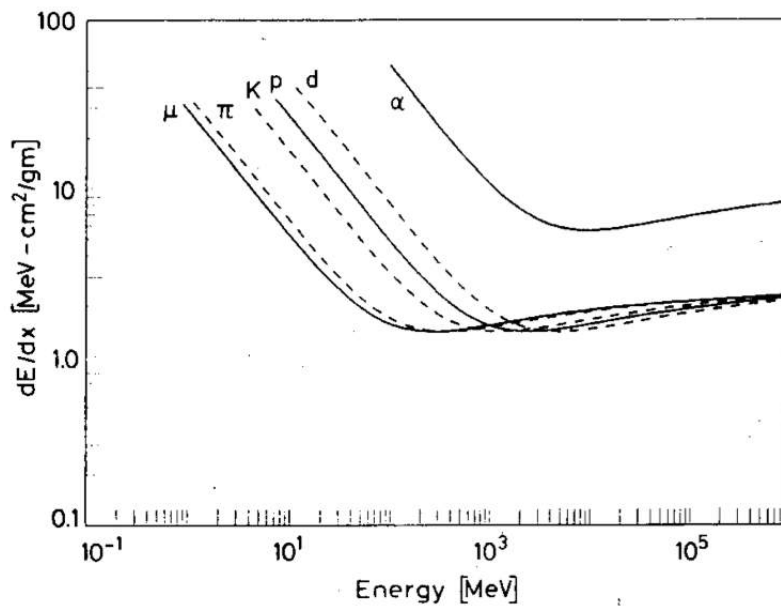
Figure 3.4: *The stopping power dE/dx as function of energy for different particles. Figure from Leo (1994).*

At non-relativistic energies, dE/dx is dominated by the overall $1/\beta^2$ factor and decreases with increasing velocity until about $v \sim 0.96c$, where the *minimum ionizing energy* is reached. The minimum value of dE/dx is almost the same for all particles of the same charge as shown in Figure 3.4. At energies beyond this point, the term $1/\beta^2$ becomes almost constant and dE/dx rises again due to the logarithmic dependence of Equation 3.4. For energies below the minimum ionizing value, each particle exhibits a characteristic dE/dx curve. This is often exploited for the identification of particles.

3.1   Gamma-ray spectroscopy detectors

The prototype under investigation in this thesis is mainly designed for spectroscopic purposes. Spectroscopy, in general, aims at measuring the energy of an incoming electromagnetic radiation or a flow of particles in order to determinate the properties of their source. A detector which is developed for spectroscopic purposes must be able to accurately distinguish the different energies deposited within its sensitive volume.

For γ-ray spectroscopy up to to several MeVs the most frequently used detectors are based on the coupling between scintillators and photodetectors like semiconductor detectors or photomultiplier tubes (PMT).

3.1.1   Semiconductor detectors

Semiconductor detectors are based on a crystalline semiconductor material, the most common used for designing radiation detectors are Silicon and Germanium.

The outer atomic levels of a semiconductor exhibits an energy band structure. In Figure 3.5 is shown this structure which consists in a *valence band*, a *forbidden energy gap* and a *conduction band*, and also shows a comparison with the band structure of insulators and metals.

In the conduction band, electrons are free to move into the entire crystalline structure since they have high enough energy to be disentangled from their parent atom. The electrons in the valence band, however, are more closely bound and
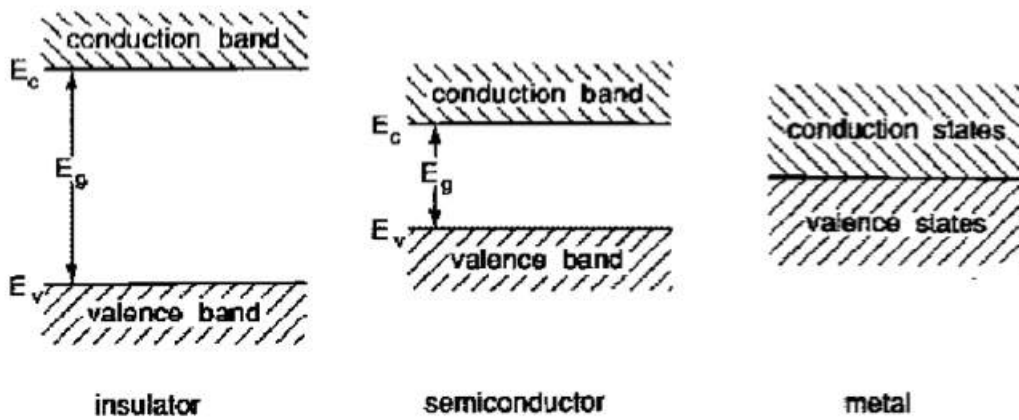
Figure 3.5: *Band theory schematic distinction between insulator, semiconductor and metal. Figure from Knoll (2010).*

remain associated to their respective lattice atoms. Every time an electron leaves its parent atom, a *hole* is created. A hole is the absence of an electron in an atom and, although it is not a real particle, it is a charge carrier responsible for a current that flows in the opposite direction with respect the current generated by the flow of electrons.

In metals the conduction and the valence bands overlap, there is no forbidden energy levels and electrons from the valence band can freely move to the conduction band. In an insulator, at normal temperatures the electrons are all in the valence band, since the thermal energy is insufficient to excite the electrons across the gap. When an external electric field is applied to an insulator, there is no movement of electrons and thus no current. In a semiconductor the energy gap is intermediate in size, such that only a small but appreciable amount of electrons is excited into conductive band by thermal energy. When an external electric field is applied a small current is observed.

The semiconductor conductivity can be changed by cooling or by the introduction, in its crystal lattice, of atoms from an other element in a few part per billion. This process is called *doping*, and the result semiconductor is referred as *extrinsic*. *Intrinsic* semiconductors are, instead, the pure ones.

Extrinsic semiconductor can be classified in two types: n-type and p-type semi-conductor. n-type semiconductors are created by substituting some atoms of the semiconductor itself with donor atoms. A donor atom has more valence electrons than the atom it replaces. This kind of doping leads to an excess of electrons in the semiconductor. The other doping mode is realized instead with acceptor atoms, that have fewer valence electrons than the atoms they replace. This provides an excess of holes, leading to an p-type semiconductor. When the amount of doping is high, $\sim 10^{18} \text{cm}^{-3}$, it is referred as p^+ or n^+ versus the $\sim 10^{13}$ cm^{-3} of p-type and n-type. The doping open a wide range of applicative possibilities. Since doping alters the arrangement of the energy levels, is possible to vary the conductivity introducing the adequate amount of doping for the desired application.
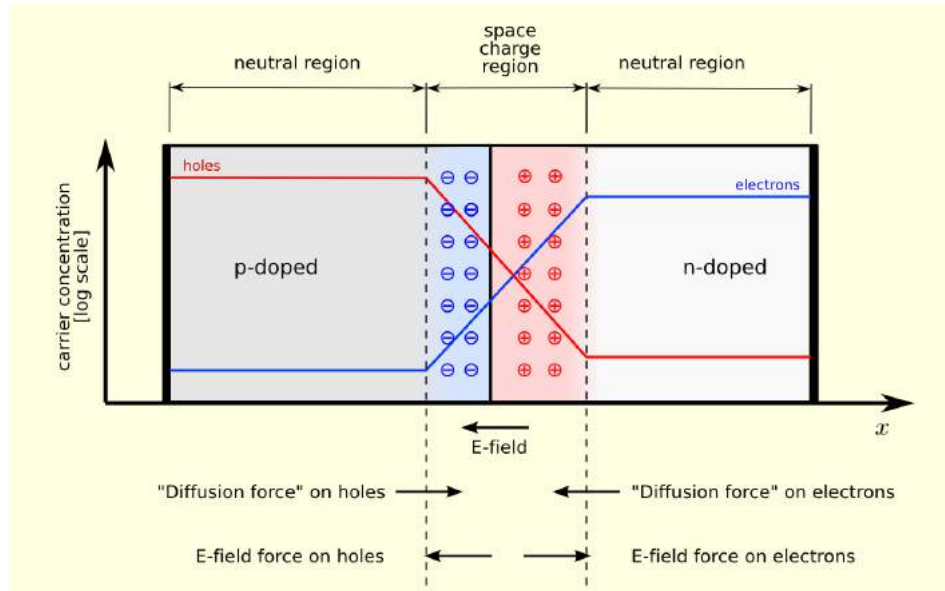
Figure 3.6: *Representation of a pn junction and its depletion region*

The operation of semiconductor detectors depends on the formation of a semi-conductor *p-n junction* that can be obtained for example by diffusing sufficient p-type activators into one end of a homogeneous bar of n-type material resulting into changing that end into a p-type semiconductor. Free electrons and holes of the two materials will diffuse towards the lower concentration zone and recombine, creating

the *depleted zone*. The departure of an electron from the n-side to the p-side leaves a positive donor ion behind on the n-side, and likewise the hole leaves a negative acceptor ion on the p-side. Since the p-side is injected with extra electrons it thus becomes negatively charged, while the n-side becomes positive leading to the creation of an electric field gradient across the junction which stops the diffusion process. The depletion zone, shown in Figure 3.6, has the property of being devoid of all mobile charge carriers. The passage of radiation in this zone creates electron-hole pairs. The number of electron-hole pairs generated is given by

$$N = \frac{E}{w} \tag{3.5}$$

where E is the energy of the incoming radiation and w is average energy needed to generate a pair. If a voltage is applied on both ends of the junction, a current signal proportional to the ionization will be detected.

The main advantage of semiconductor as radiation detector is the very small average energy ω needed to create an electron-hole pair, i.e. for Si $\omega_{\mathrm{Si}} = 3.62$ eV and $\omega_{\mathrm{Ge}} = 2.96$ eV. Compared to the energy gap that are 1.1 eV and 0.7 eV, respectively, this shows how less than a third of the energy deposited by passing radiation is spent on the production of electron-hole pairs. The others two thirds go into exciting lattice vibrations.

Since $E_{\mathrm{Gap}}^{\mathrm{Si}} > E_{\mathrm{Gap}}^{\mathrm{Ge}}$, given the same energy deposited into the materials, in Ge a greater number of electron-hole pairs compared to Si is produced, leading to a more intense charge signal. Better spectroscopic performance can be achieved with Ge if properly cooled (a liquid nitrogen cooling system is required) because a low value of E_{Gap} causes current due to the thermal agitation. For this reason Ge present a worse spectroscopic performance with respect to Si at room temperature.

3.1.2   Photomultiplier Tubes

The photomultiplier tubes (PMTs) are detectors sensitive to visible light, producing an electrical signal in very short times (few ns). Because of that, they have been often coupled with scintillators. A typical PMT is shown in Figure 3.7 and basically consists of two parts: the *photocathode* and the *multiplication system*. The photocathode converts the incident light into electrons by means of the photoelectric effect. The conversion efficiency depends on the wavelength of the incident light and the material constituting the photocathode. The electrons generated from the photocathode are collected and focused on the first stages of the multiplication system by an electron-optical input system.
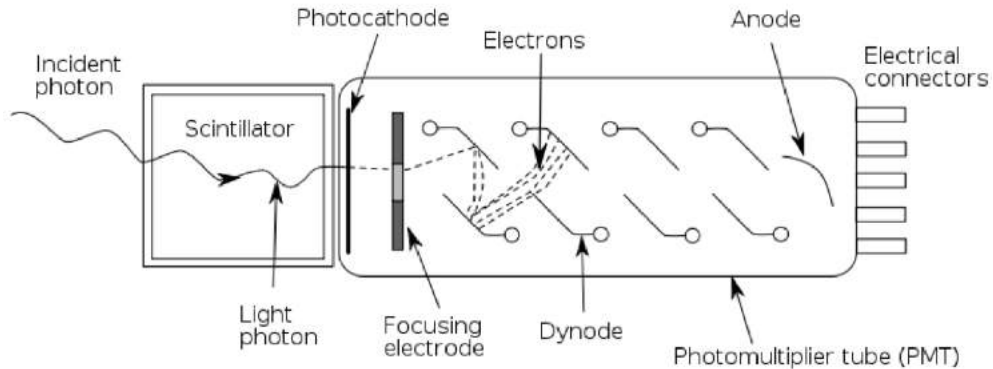
Figure 3.7: *PMT working principle schematics.*

The multiplication system amplifies the weak current generated by the photocathode thanks to a series of electrodes called *dynodes*, producing a measurable signal at the anode. The dynodes emit for *secondary emission*, a process very similar to photoelectric effect except that the photon is now replaced by an electron. As the electron impacts on a dynode, energy is transferred directly to other electrons in the material of the dynode allowing a number of electron to escape. In order to focus and accelerate the electron flux from one dynode to the following till the collecting anode, a electric field is applied. Most conventional PMT contain from 10 to 14 dynodes achieving an overall gain up to 10^7 on the initial current generating a macroscopic charge pulse.

The behavior of the detectors described above, regardless of the operating principle, is described by parameters such as the *energy resolution*, the *noise* of the system, the *efficiency* and the *sensitivity*. These parameters will be illustrated in the following section.

3.1.3 Energy resolution

The *energy resolution* indicates the ability of a detector to distinguish between two close monochromatic δ-shaped lines. For this reason, it is the parameter that defines the spectroscopic performance of the detector. The monochromatic δ-shaped line is just a idealization, indeed, lines are usually Gaussian-shaped. As shown in Figure 3.8a, the energy resolution at a given energy E_0 is formally defined as the ratio between the *full width half maximum* (FWHM), i.e. the width of the spectral distribution at half of its height, and the mean value E_0:

$$R = \frac{FWHM}{E_0} \tag{3.6}$$

where R is dimensionless and is often expressed as a percentage.

Two close energies are considered resolved only if separated by more than a FWHM. The number of charge carriers generated by the incoming radiation statistically fluctuates and, assuming that the formation of each charge carrier is a *Poisson process*, given N charge carriers generated on average, a standard deviation of $\sqrt{N}$ is expected. Usually, the detector response is linear, so $E_0 = KN$ where K is a proportionality constant. The standard deviation σ of the peak is $\sigma = K\sqrt{N}$ and its FWHM is $2.35K\sqrt{N}$. So the limiting resolution due only to statistical fluctuations is:

$$R_{\text{stat}} = \frac{FWHM}{E_0} = \frac{2.35K\sqrt{N}}{KN} = \frac{2.35}{\sqrt{N}} \tag{3.7}$$

which is the theoretical limit the energy resolution can achieve. The above theoretical treatment is based on the assumption that the production of each single charge
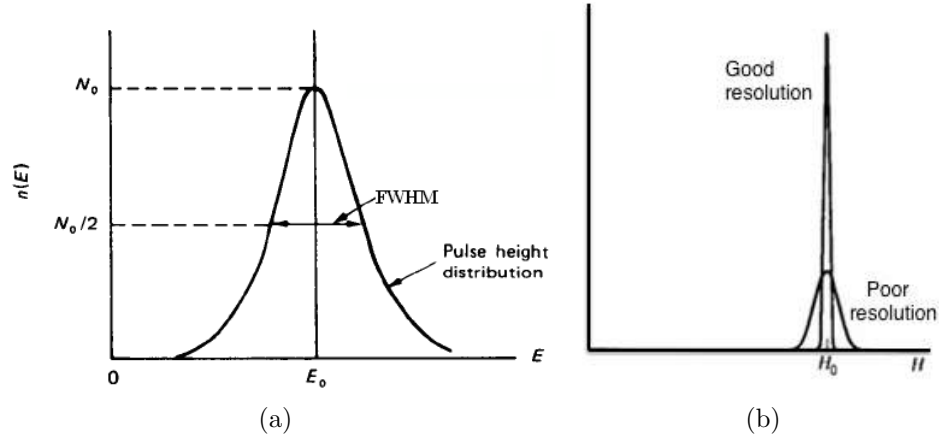
Figure 3.8: *(a) A typical energy peak of a spectrum in which the FWHM, the energy E_0 and the distribution are identified (b) A comparative example between good resolution and poor resolution.*

carrier is statistically independent. In some cases the generation process could be different, for example multiple excitation mechanisms can occurs making the charge carrier generation not independent. This is the case of X-ray detection in solid state detectors. The correction term that takes in account this effect is the *Fano factor F* (Fano, 1947), thus the resolution can be rewritten as

$$R_{stat} = 2.35\sqrt{\frac{F}{N}} \tag{3.8}$$

The Fano factor is $F = 0.118$ and $F = 0.13$ for Si and Ge respectively (LOW, 1997). It also slightly vary with temperature (Mazziotta, 2008).

The resolution is not only influenced by the statistical term; other elements are also present which contribute to spread the line worsening the resolution. In case of spectroscopic detectors, the electronic chain used to process the output signal introduces fluctuations that are referred as *electronic noise*. The convolution of all the contributions is represented by the total FWHM actually measured:

$$(FWHM)_{\text{Tot}}^2 = (FWHM)_{\text{Stat}}^2 + (FWHM)_{\text{Noise}}^2 + (FWHM)_{\text{Sys}}^2 \tag{3.9}$$

where $FWHM_{\mathrm{Sys}}$ is a term that takes in account all the other contributions that are not statistical or due to the measurement noise.

3.1.4 Sources of electronic noise

By definition, noise is any undesired fluctuation that appears superimposed on a signal source. The nature of this fluctuation can be statistical or due to the instruments used to take the measurement.

The sources of electronic noise can be classified in three main classes: *thermal noise*, *low-frequency voltage noise*, and *shot noise*.

Thermal Noise This noise is due to the thermal fluctuations of the electron distribution in a conductor. Consider, for example, a resistor of resistance R. Even without having a current flowing, it is possible to measure a noise voltage U between the two terminals of the resistor. The spectral density of the noise power, according to thermodynamic calculations, is given by

$$\frac{dU^2}{df} = 4kTR \tag{3.10}$$

with f the frequency, k the Boltzmann constant and T the absolute temperature. As the thermal noise spectrum is independent of the frequency, thermal noise is often referred to as *"white noise"*. Since sources of thermal noise are the resistors of the circuits, it can be modeled as a voltage generator in series with the signal source and is also referred as *series noise*.

Low-Frequency Voltage Noise Since the physical source of this noise is not unique, and may be due to widely differing mechanisms for different types of electronic elements, this type of noise is seen in most electronic devices. The noise power spectrum in most cases has an approximate $1/f$ dependence, described by:

$$\frac{dU^2}{df} \approx \frac{A}{f^\alpha} \, , \qquad \text{with } \alpha \approx 1 \tag{3.11}$$

where A is a proportional constant. Furthermore, the $1/f$ dependence is only a rough approximation. Since its spectral density varies with f, this type of noise is often referred to as *"pink noise"*.

Shot Noise Fluctuations in the number of charge carriers may occur in many circumstances, such as the case in which the emission is limited by a potential barrier, where the probability of a carrier to cross the barrier is independent of any other carrier emitted, so the emissions are random and uncorrelated.

The frequency spectrum fluctuations in a flowing current i due to the shot noise can be expressed as

$$\frac{di^2}{df} = 2Iq \tag{3.12}$$

It is also referred as *parallel noise* since it can be modeled as a current generator in parallel with the detector capacitance C_D and the capacitance of the preamplifier system C_i. Notice that shot noise requires the presence of a current flow caused by an external power source, while thermal noise is present in devices even without the application of external power.

3.1.4.1   Equivalent Noise Charge

A figure of merit to characterize the electronic noise in the solid state detectors is the *equivalent noise charge* (ENC). It is defined as the quantity of charge that gives in output a signal equal to the rms value of the signal. The ENC depends on the series, parallel and $1/f$ noise in the following way:

$$ENC^2 = a\left(C_D + C_i\right)\frac{A_1}{\tau} + kA_2 + bA_3\tau \tag{3.13}$$

where a, k and b are parameter depending on series, $1/f$ and parallel noise respectively, A_1, A_2 and A_3 are coefficients depending on the filter used and τ is the *shaping time* that is a characteristic time in amplifier systems that will be treated in §3.2.2. In Figure 3.9 is reported the dependence of the ENC from series and parallel noise at different shaping times.
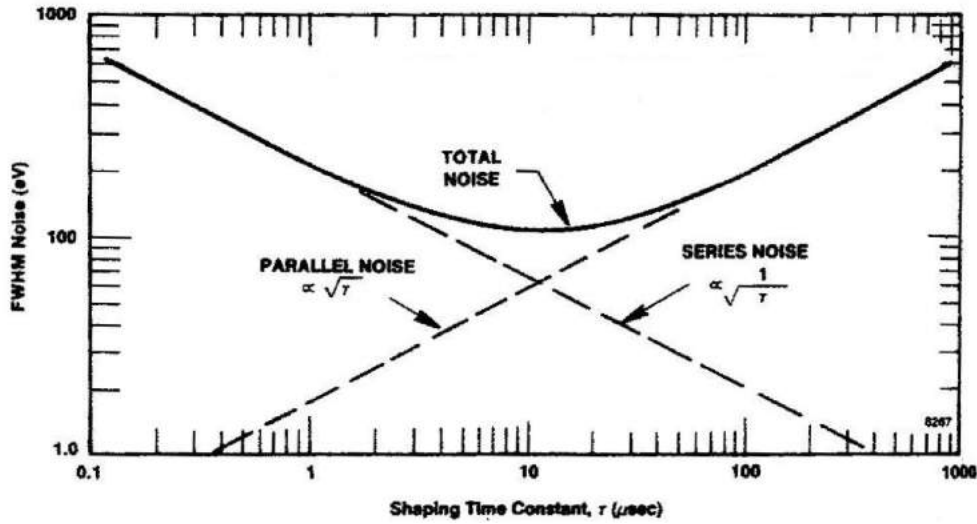
Figure 3.9: *The dependence of the ENC from the series and parallel noise at different shaping times. Figure from Schonkeren (1970)*

The contribution of series noise tends to become less important as the shaping time is increased. On the other hand, sources of parallel noise become more important. Considering the effect of the combination of all three sources of noise (which will combine in quadrature), the overall electronic noise will go through a minimum at a given shaping time, which is generally at the point where series and parallel noise contributions are equal.

3.1.5   Efficiency

Since the interaction between radiation and the detector material is not a deterministic process but a probabilistic one, not all the incident radiation will be detected. The parameter that takes into account the percentage of revealed particles is the *efficiency*, and is due to both geometrical and physical characteristics.

Efficiency can be defined by

$$\epsilon(E) = \int_{\Omega} \prod_i (\exp(-\mu_i(E)x_i)) \cdot (1 - \exp(-\mu_d(E)x_d)d\Omega \tag{3.14}$$

where μ_i and x_i are the *stopping power* and the *dimension* of the passive layers that separate the radiation source from the detector (i.e. air, shielding material, etc), and μ_d and x_d are the same quantities but referred to the detector. Efficiency is also expressed in relative terms as percentage of the ratio between the number of particles that interact within the detector and the number of particles revealed

$$\epsilon = \frac{N_{\text{incident}}}{N_{\text{revealed}}} \qquad\qquad (3.15)$$

3.2   Spectroscopic setup

The charge signal given by the detector must be processed in order to maximize the SNR. To elaborate the information it contains, a series of electronic circuits that perform logic operations on the signal is implemented at the detector output. The ensemble of these circuits is often referred as *spectroscopic setup* for detectors sensitive to the energy of the incoming radiation or, more generally, *electronic chain*.

Many different circuits and operations are used according to the experimental requirements. In this section the general circuits that are usually used in X and γ-ray spectroscopy with a semiconductor detector will be presented.

A typical spectroscopic setup is presented schematically in Figure 3.10.

3.2.1   Charge sensitive preamplifier

The *charge sensitive preamplifier* has the function to convert the detector output charge into a voltage signal proportional to the charge, and to provide the output pulse to the following electronic circuits, i.e. the shaping amplifier, therefore its name "preamplifier".

The signal from a semiconductor detector is a quantity of charge $q(t)$ proportional to the absorbed energy E, and is delivered as a current pulse. Thus the preamplifier ideally receives a delta-shaped charge pulse and returns a signal that is the convolution of this charge signal and its impulse response $h(t)$: $f(t) = \int q(t')h(t-t')dt'$ resulting in
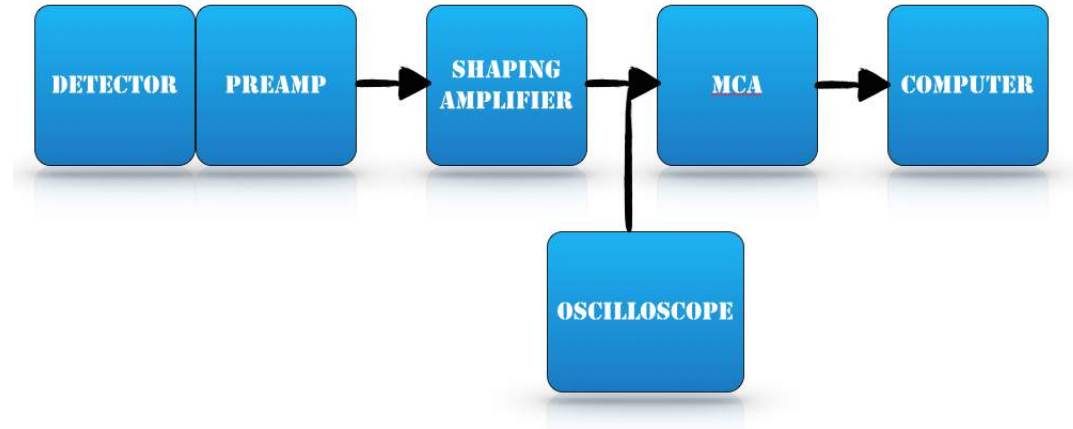
Figure 3.10: *A generic spectroscopic setup is made of preamplifier and amplifier for signal analysis, a Multi Channel Analyzer and a Computer for acquiring and storing the data.*

$$f(t) = Ee^{-\frac{t}{T}} \tag{3.16}$$

where T is the time discharge constant, and is usually in the range of hundreds of microseconds for the case of solid state devices.

The preamplifier is made of three stages. A *Junction Field Effect Transistor* (JFET) is often used as first stage of the preamplifier. It is a unipolar (i.e. one type of charge carrier participates in the conduction process) transistor based on a p-n junction. Its schematic is reported in Figure 3.11 where the highly doped n-sides (called *source* and *drain*) are connected by a narrow channel. The depth of the channel adjust the charge that flows in the transistor and can be changed by the *gate voltage* resulting in a variation of the size of the two depleted regions and consequently also on the channel depth. In some applications the gate can not be modifiable for a variety of reasons (in Chapter 6 we will see that the preamplifier used in this thesis work is one of those cases). In such cases, a second gate called *backgate* is used in order to adjust the channel depth.

The JFET is followed by the second stage of the preamplifier, where the charge is integrated on the *feedback capacitor* that connects the output and the input of an
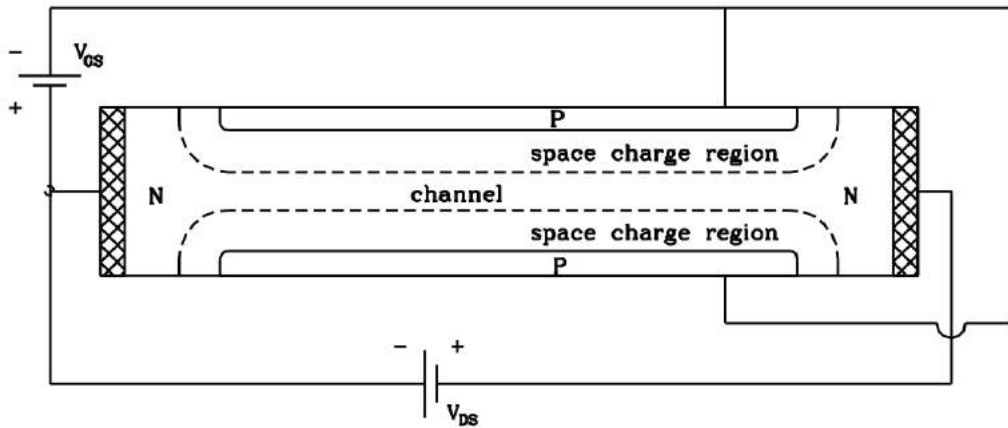
Figure 3.11: *Principle of an n-channel JFET transistor. Figure from Lutz (2007).*

operational amplifier. To avoid saturation of the feedback capacitor, it is discharged by means of the *feedback resistor*. This operation gives the characteristic exponential decay in the output, with a time constant $T = R_f C_f$, where R_f and C_f are the value of the feedback resistance and the capacitance, respectively. In order to ensure that complete charge collection occurs, preamplifiers normally provide a decay time for the pulse which is quite long (typically 50 μs). If the interaction rate is not small, these pulses will tend to overlap one another resulting in a pulse train such as shown in Figure 3.12a. This overlapping is referred as *pile-up* and can result in an incorrect handling of the true amplitude of the charge signal Q that produces the pulse. To prevent this to happen the output signal of the preamplifier is sent to the shaping amplifier that changes the shape of the signal to produce a pulse train as shown in Figure 3.12b preserving the information on the maximum amplitude.

The last stage is the one which drives the output voltage, proportional to the charge collected, and adjusts the output impedance Z_{out} to the lowest values as possible to minimize signal loss when the output is loaded by the subsequent component.

The most important specification for a preamplifier is its noise figure. The noise figure depends strongly on the capacitance with which the preamplifier input is loaded. The input capacitance arises from both the inherent detector capacitance and from the connecting wire between the detector and the preamplifier. Thus is
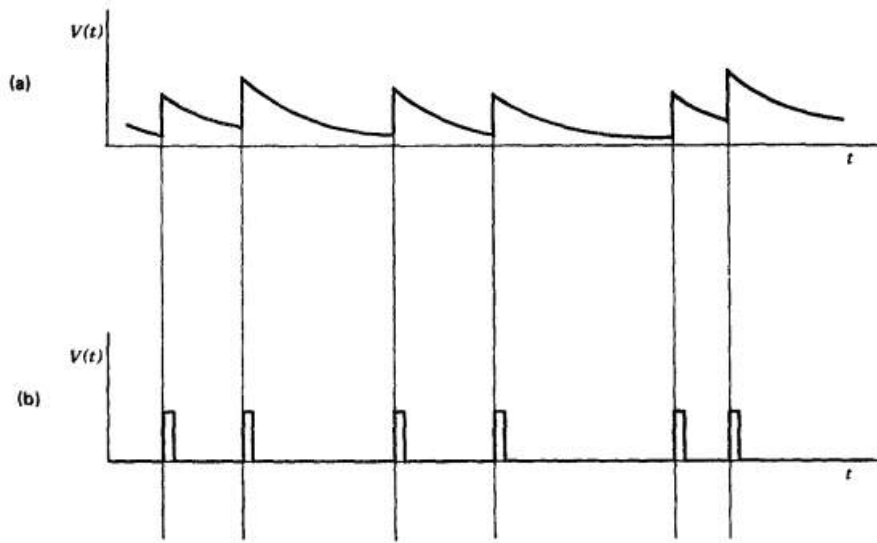
Figure 3.12: *The pulses with long tails shown in part (a) illustrate the apparent variation in amplitude due to pulse pile-up. These effects can be largely reduced by shaping the pulses as in part (b).*

important to keep the wiring as short as possible.

In order to design low-noise preamplifiers the R_f can be eliminated, resulting in two potential gains. One is the removal of the thermal noise associated with the resistance and the other is about avoiding pulse pile-up at high rates. Without R_f the charge pulses from the detector are accumulated on the feedback capacitance and the output voltage is a sequence of pulses with infinite length tails (Figure 3.13). A method must be provided to reset the voltage to zero before it can approaches to saturation level. This can be achieved using a *reset transistor*. It acts as a switch creating a short circuit that immediately discharges the feedback capacitance. This can reduce the overall noise of the device but introduces *dead time*: during the reset period (Figure 3.13) no further events can be acquired.

Thus the way the capacitor is discharged identifies, as shown in Figure 3.14, two different working configurations for the preamplifier: *pulsed reset configuration* and *continuous discharge configuration*.
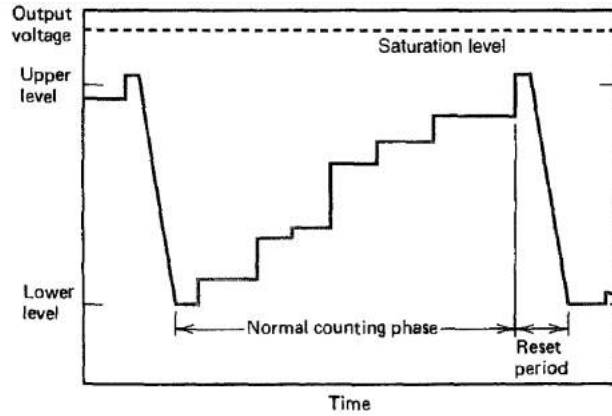
Figure 3.13: *The output voltage of a pulse reset preamplifier. The reset phase is triggered when the voltage crosses the upper-level limit during the normal counting phase. Each upward step is a separate signal pulse.*
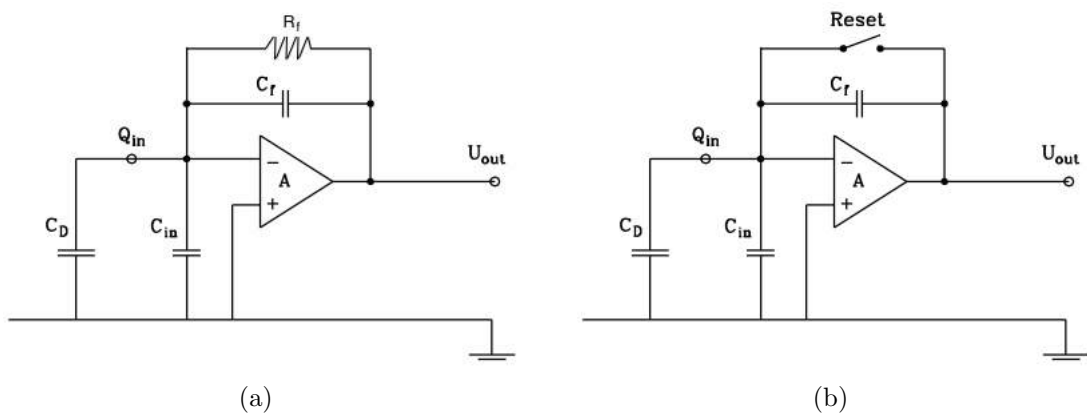
Figure 3.14: *Simplified schematic of a charge sensitive preamplifier with (a) a feedback resistor and (b) a pulsed reset switch.*

3.2.2 Shaping amplifier

Once the charge signal is converted into a voltage signal, it can be easily handled by other components such as the *shaping amplifier*. The shaping amplifiers filters the signal improving the signal-to-noise ratio by limiting the response of the instrumentation to those frequency ranges in which the signal has useful components while reducing as much as possible the transmission of frequency components from the various sources of noise and reduces the time duration of the signal preventing pile-up.

The simplest shaping amplifier is represented by a CR high-pass filter followed by an RC low-pass filter. The first filter attenuates the signal frequencies components lower than the *cutoff frequency* $f_c = \frac{1}{2\pi RC}$. Since the noise frequency distribution is wider than the signal frequency distribution, the signal-to-noise ratio is increased at filter output. Before the pulse reaches the output of the amplifier, it passes through the RC low-pass filter. The RC filter attenuates the frequency higher than its cutoff frequency.
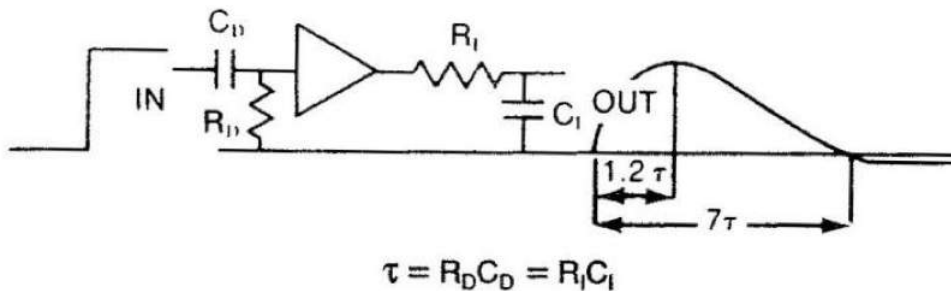
Figure 3.15: *CR-RC pulse shaping.*

A shaping amplifier may consist in more than one CR and RC basic circuits, so it can generally can expressed as $(CR)^n - (RC)^m$ with n and m as the *pole* order. The bandwidth of the shaping amplifiers is thus defined by the difference between the lower and the upper cutoff frequencies of CR and RC filters.

The global time constant of the final $(CR)^n - (RC)^m$ circuit defines the *shaping time* τ of the filter. In the interest of reducing pile-up, a short time constant is

preferable, so that the shaped waveform can return to the baseline as quickly as possible. Once the shaping time constant becomes shorter or comparable with the rise time of the pulse from the preamplifier some information on the amplitude is lost. This loss is called the *ballistic deficit* and can be avoided by keeping the time constant long compared with the charge collection time in the detector. Also the signal-to-noise ratio characteristic of the pulses influence the choice of the shaping time since the interplay of the series and parallel noise leads to an optimum choice of the shaping time when the minimization of Eq (3.13) is the final purpose.

The ENC defined in §3.1.4 is used as a figure of merit to estimate the quality of the shaping filter. It is shown that the best shape, which maximizes the signal to noise ratio, is the cusp, but it is not particularly practical for several reasons. The top is sharply pointed, which makes pulse amplitude measurement difficult unless pulse-stretching methods are employed. The restoration of the baseline is slow which is undesirable from a pile-up standpoint. It is also difficult to achieve with practical shaping circuits. For all these reasons, other methods of pulse shaping are more commonly used. It is useful to normalize the performance of the other shapers to the cusp in order to perform a comparison

$$\frac{ENC^2(shape)}{ENC^2(Cusp)} = \sqrt{A_1 A_3} \tag{3.17}$$

The values of this rail for various shapers are reported in the scheme in Figure 3.16.

3.2.3   Multi-Channel Analyzer

The multichannel analyzer (MCA) is an instrument used to measure the frequency distribution the signal amplitudes. A measurement of the differential pulse height spectrum from a radiation detector can yield important information on the nature of the incident radiation. By definition, the differential pulse height spectrum is a continuous curve that plots the value of dN/dH versus the value of the pulse height H. Since the ratio of the differentials can never be measured exactly, all the measurement techniques involve a determination of $\Delta N/\Delta H$. The increment in pulse height ΔH is commonly called the *channel width*. If ΔH is small enough, a
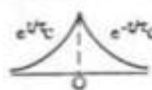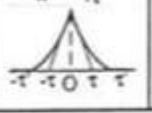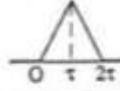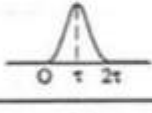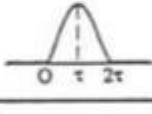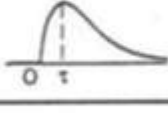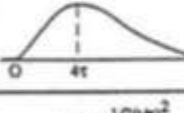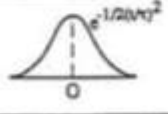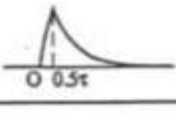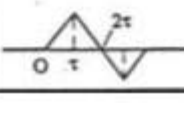
	Shaping	h(t) Function	A_2	$\sqrt{A_1 A_3}$	$\dfrac{A_2}{\sqrt{A_1 A_3}}$	A_1	A_3	$\sqrt{\dfrac{A_1}{A_3}}$
1	indefinite cusp	e^{t/τ_c} e^{-t/τ_c}	0.64 $\left(\frac{2}{\pi}\right)$	1	0.64	1	1	1
2	truncated cusp	$k = \tau'/\tau$ k=1 k=2 k=3	0.77 / 0.70 / 0.67	1.04 / 1.01 / 1	0.74 / 0.69 / 0.67	2.16 / 1.31 / 1.10	0.51 / 0.78 / 0.91	2.06 / 1.30 / 1.10
3	triangular		0.88 $\left(\frac{4}{\pi}\ln 2\right)$	1.15 $\left(\frac{2}{\sqrt{3}}\right)$	0.76	2	0.67 $\left(\frac{2}{3}\right)$	1.73
4	trapezoidal		1.38	1.83	0.76	2	1.67	1.09
5	piecewise parabolic		1.15	1.43	0.80	2.67	0.77	1.86
6	sinusoidal lobe		1.22	1.57	0.78	2.47	1	1.57
7	RC-CR		1.18	1.85	0.64	1.85	1.85	1
8	semigaussian (n = 4)		1.04	1.35	0.77	0.51	3.58	0.38
9	gaussian	$e^{-1/2(t/\tau)^2}$	1	1.26	0.79	0.89	1.77	0.71
10	clipped approximate integrator		0.85	1.34	0.63	2.54	0.71	1.89
11	bipolar triangular		2	2.31	0.87	4	1.33	1.73

Figure 3.16: *Parameters for the shaping functions. Figure from Gatti (1990).*

plot of $\Delta N/\Delta H$ versus H is a good approximation to the continuous curve of the actual differential pulse height spectrum.

The operation of a MCA is based on the principle of converting an analog signal (the pulse amplitude) to an equivalent digital number. Thus the analog-to-digital converter (ADC) is a key element in determining the performance characteristic of the analyzer. The basic function of the MCA involves an ADC and a digital memory. The number of addressable location in the memory defines the maximum number of channels into the spectrum can be subdivided. Once that the pulse has been processed by the ADC, the analyzer control circuits seek out the memory location corresponding to the digitized amplitude and the location is incremented by one count. This process is repeated and therefore the total accumulated number of counts is simply the total number of pulses measured. A MCA is directly connected to a computer for a direct display of the results.

3.2.4   Waveform Digitizer

The analog spectroscopic chain has represented the only choice available in the design of pulse processing systems for many decades. The development of high-speed analog-to-digital converter with good resolution opened a new possibility for the digital processing of pulses from the detectors. All the information in a single analog pulse from a preamplifier can be preserved with a high frequency sampling of the pulse. These arrays of data then can be further manipulated using standard digital operations in order to perform the same signal processing that takes place in the analog chain.

The electronic device that performs such operation is commonly called *digitizer*. The basic operating mode of a digitizer is essentially the same as a digital oscilloscope: the analogue signal is sampled by a flash ADC, and stored. When a signal must be acquired, a trigger arrives to the digitizer and the buffer is frozen and made available for the readout. A signal, to be properly acquired, must be characterized by a voltage that fits in the *dynamic range* of the instrument. Since the digitizer must be able to sample the signal in all its own time characteristic, the sampling rate of the digitizer

must be high enough to sample the frequencies that make up the signal.

In addition to the sampling rate, the *bit resolution* of the digitizer represent a fundamental parameter. An 8-bit digitizer will generate 256 discrete codes over its dynamic input range, a 12-bit digitizer will generate 4096 and so on. This number defines the maximum number of intervals into which the input voltage can be sorted.

The digitized waveforms are successively shaped via software that implement digital shaping algorithms.

3.2.5 Digital shaping

The digitized signal are then processed via software. The digital signal processing offers many potential advantages: unlimited flexibility in the choice of shaping parameters since these are just inputs into the software routines that carry the digital operations. For example, changing the shaping time in a conventional analog shaper requires switching physical circuit components and repeating the measurements. It also allows to design shapes that are impossible to achieve in analog circuits. Another advantage is the stability: once the signal is digitized, there can be no further change in that information, and the subsequent processing will be totally immune from the drifts that can take place in analog processors because of temperature or line voltage changes. So, the task that an analog shaping amplifier does in real time, is substituted by software that processes the digital data via digital algorithms.

Many different digital shaping algorithms have been developed, allowing to shape the signal in different forms, the Gaussian (T. Kihm, 2003), the cusp algorithm (Dig, 1994) to the trapezoid (Georgiev and Gast, 1993).

The development of such algorithms is often based on the *Z-transform*. The *Z*-transform allows to convert a function in the time domain into its representation in the complex *Z*-domain:

$$X(z) = \sum_{n=-\infty}^{\infty} x(n)z^{-n} \tag{3.18}$$

where z is a complex variable and $x(n)$ is a sequence representing a sampled signal.

The Z anti-transform allows the opposite conversion:

$$x(n) = \frac{1}{2\pi j} \oint_C X(z) z^{n-1} dz \tag{3.19}$$

where C is the convergence region.

For the Z-transform, such as for the Fourier transform, the convolution theorem is valid:

$$x_1[n] * x_2[n] \Leftrightarrow X_1(z) X_2(z) \tag{3.20}$$

It shows how the convolution of two sampled signal in the time domain is equal to the simple multiplication of their Z-transforms in the Z-transform domain.

It can be demonstrated that, for a detector with a collecting time that is not constant, the best shaping is the trapezoid (Dig, 1994). The general convolution theorem that allows to derive an algorithm for the trapezoid shaping is as follows

$$F_{\text{TRZ}}(z) = F_{\text{IN}}(z) \cdot H_{\text{SHA}}(z) \tag{3.21}$$

where $F_{\text{TRZ}}(z)$ is the Z-transformed function of the trapezoid itself and $F_{\text{IN}}(z)$ is the Z-transformed function of the input wave from the preamplifier. The expected shaping transmittance (the transfer function that relates the response of a linear time-invariant system, in this case $F_{\text{TRZ}}(z)$, and the input function $F_{\text{IN}}(z)$) has the form

$$H_{\text{SHA}}(z) = \frac{F_{\text{TRZ}}(z)}{F_{\text{IN}}(z)} \tag{3.22}$$

Assuming that the energy impulse from the preamplifier has the form described in Equation 3.16, in Z-transform domain it assumes the following form:

$$f(t) = E e^{-\frac{t}{T}} \rightarrow F_{\text{IN}}(z) = E \frac{z}{z - \beta} \tag{3.23}$$

where β is the a term that corrects the effect of undershooting that may happen after the signal shaping: $\beta = e^{-\Delta t/T}$ where Δt is the sampling period.
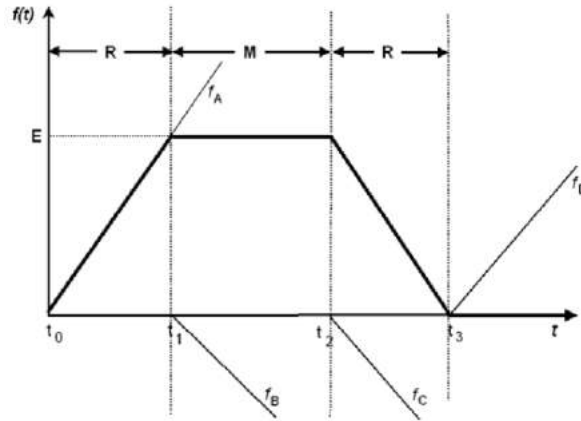
Figure 3.17: *Syntesis of the trapezoid. Figure from Guzik (2013)*

A trapezoid shape, such as shown in Figure 3.17, may be described as the sum of four linear components in the time domain:

$$f_{TRZ}(t) = f_A(t) + f_B(t) + f_C(t) + f_D(t) \tag{3.24}$$

where a linear pulse $f_A(t)$ may be expressed in the time domain and Z-transform domain as

$$f_A(t) = \frac{E}{t_1}t \rightarrow F_A(z) = \frac{E}{R}\frac{z}{(z-1)^2} \tag{3.25}$$

Given $f_A(z)$, three of the linear pulses can be expressed in the Z-transform domain by means of a delayed $F_A(z)$ function with adequate polarities.

$$\begin{aligned} F_B(z) &= -F_A(z) * z^{-R} \\ F_C(z) &= -F_A(z) * z^{-(R+M)} \\ F_C(z) &= -F_A(z) * z^{-(R+M+R)} \end{aligned} \tag{3.26}$$

where R and M are the number of samples used to define the rise time and the flat-top of the trapezoid which came from the following time assignment

$$t_1 = R\Delta t, \qquad t_2 = (R+M)\Delta t, \qquad t_3 = (R+M+R)\Delta t \tag{3.27}$$

where Δt is the time difference between a sample and the next, t_1 is the rise time, t_2 is the rise time added to the flat-top time and t_3 is the total duration of the trapezoid.

The final form of the algorithm, where φ is a normalization coefficient ($\varphi = 1/R$) is:

$$F_{TPZ}(z) = (1 - z^{-R}) * (1 - z^{-(R+M)}) * \frac{1 - \beta z^{-1}}{1 - z^{-1}} * \frac{z^{-1}}{1 - z^{-1}} * \varphi \qquad (3.28)$$

The presented expression describes a linear time invariant system. It means that the realization of the shaping circuit can be subdivided into independent operations executed in any order. The graphical representation of the developed algorithm is presented in Figure 3.18.
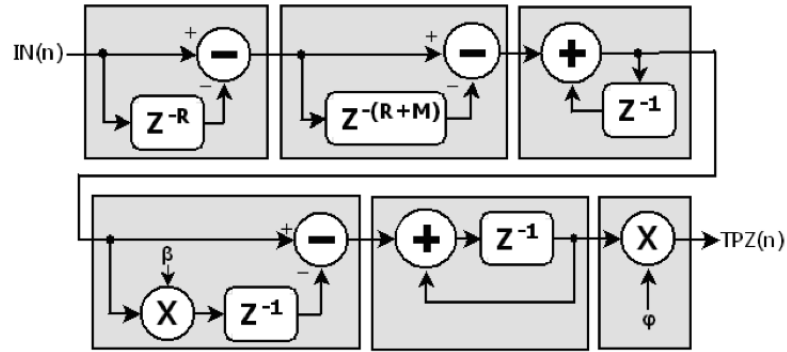
Figure 3.18: *Graphical representation of the trapezoidal algorithm. Figure from Guzik (2013).*

A generic z^{-n} represent a shift of n intervals of the sampled signal. The algorithm is therefore a series of shifting and adding operations on the arrays which contain the sampled signal.

The use of digital shaping provides a clear advantages in terms of time with respect the classical analog chain at a given spectroscopic performance. Since the huge amount of memory required to store the digitized waveforms is a limit in its applicability, it remains, at the moment, confined in the laboratory. Despite currently

its use is still not suitable for space application, where the analog chain remains the only option, new compression and data storage techniques could allow, in the future, its use on satellites.

Chapter 4

Silicon Drift Detectors

This Chapter will provide a description of the working principle and of the main characteristics of the Silicon Drift Detector, the fundamental element around which the detector characterized in this thesis is designed, taking as an example some of the possible different layouts of SDDs, thus highlighting the great flexibility of this type of technology.

The Silicon Drift Detector is a solid state device first designed in 1984 by E. Gatti and P. Rehak at Politecnico di Milano (Gatti and Rehak, 1984) for position measurements in particle physics. The realization of a SSD occurs in silicon foundries by the most known and widespread production process, the *planar process*. This process was invented by Jean Hoerni in 1959 and is the basis of the realization of a wide range of products from integrated circuits to semiconductor devices, including SDD. The SDD technology is thus based on a reliable productive process refined by the experience gained over more than half a century.

4.1 Working principle

A silicon drift detector is realized with a high resistivity n-doped silicon bulk on which are present a striped pattern of p^+ junctions (i.e. p-doped semiconductor with a higher dopant content than the p-type) over one surface of the SDD, and on

63
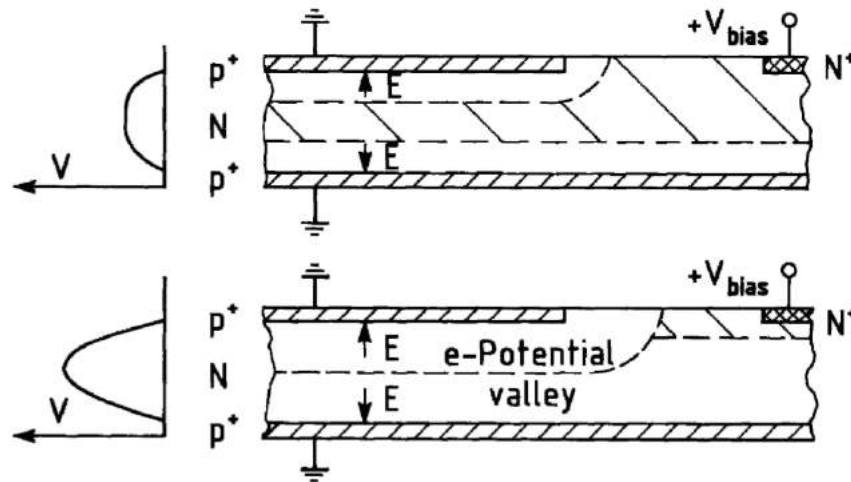
Figure 4.1: *In the upper side of the figure: Double diode partially depleted; In the lower side of the figure: Double diode fully depleted. Figure from Lutz (2007).*

the other side can be present a doped p^+ silicon layer or another striped pattern. In this way, as mentioned in the §3.1.1 and shown in Figure 4.1, two pn junctions are created with two depletion regions on both sides. Applying a reverse biased voltage, the depletions zones extend towards the center of the silicon bulk as the voltage increases, until the bulk is fully depleted.

In this way, the electron potential energy has a parabolic shape (as shown in the left side of Figure 4.1) with a minimum located in the middle of the wafer. For this reasons this process is referred as *sideward depletion principle.*

The interaction of radiation in the depletion region generates several electron-hole pairs, thus creating an electron cloud. Due to the bias voltage the electron cloud is concentrated in the center of the bulk, far from the surface which is a common source of noise. In order to force the electrons to drift towards the anode, an additional electric field is superimposed by applying a gradient voltage to the p^+ strips, in which the external voltage is more positive the closer the strip is to the anode, that is made of a n^+ region. The electrons, interacting with the superimposed electric field (Figure 4.2), drift towards the anode that can be designed in any form. The holes are instead quickly collected by the nearest cathodic p^+ contact. This characteristic
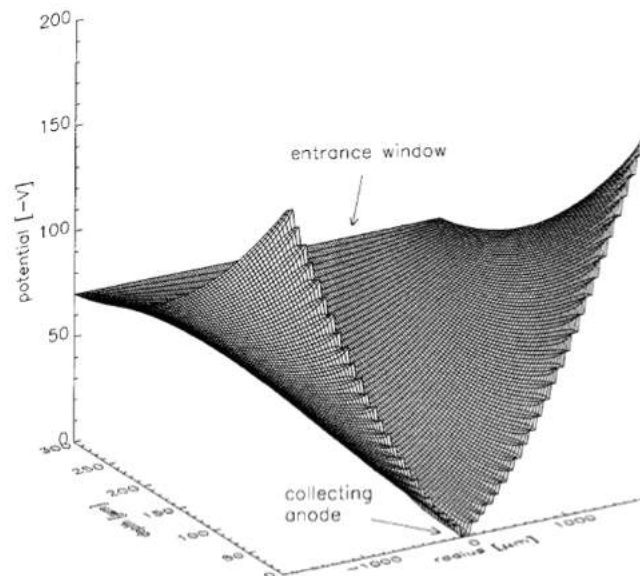
Figure 4.2: *Simulation of the potential energy for the electrons in a typical biasing condition of the SDD. Figure from Gatti and Rehak (1984).*

disentangles the area of the anode to the collecting area of the detector, allowing to design very small anodes (thus with a capacitance of the order of a few fF) whose size is limited only by the need to leave enough space to connect a bonding wire, usually of the dimension of tens of micrometers. This is the main advantage of an SDD with respect to a common p-i-n PhotoDiode with the same active area and thickness, whose collecting anode extends over all the detector surface, and thus exhibits a much higher capacitance, of the order of tens of pF.

If the time of interaction is known, the electron drift time can provide information on one interaction coordinate. According to the specifications of the design, the SDDs can be also used to exploit these position-sensitive capabilities.

4.2   SDD properties

SDDs couple a time response of the order of $\sim$100 ns when detecting X-rays and linear energetic response to an intrinsic excellent spectroscopic performance due to the very small capacitance anodes. Since the anode capacitance is of the order of few tens of fF, a bonding wire, even if few mm long, introduces a comparable stray capacitance, thus worsening the intrinsic spectroscopic performance (see Equation 3.13). To fully exploit the small anodic capacitance the first stage of the preamplifier can be also directly integrated on the SDD chip as shown in Figure 4.3. However, this is not the only viable solution. The process leading to the integration of the first preamplifier stage on the SDD is delicate and more complex since it is the union of two different production processes. To avoid these complications and maintain comparable spectroscopic performance, a solution is to ensure the best noise performance of the readout electronics.

The energy resolution (§3.1.3) that can be achieved is given by the quadratic sum of two main factors: the electronic noise (including the leakage current in the detector) and statistical fluctuations in the generation of charge carriers, thus the use of a low noise read-out electronics is fundamental to exploit the SDD energy resolution capabilities.
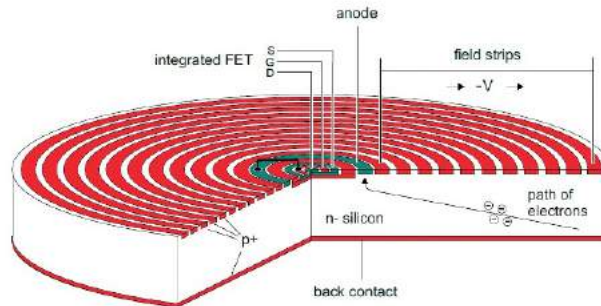
Figure 4.3: *A schematic representation of a circular SDD with integrated FET. Figure from LEC (1996).*

The detector performance depends not only on the good implementation of the production processes, but also by the quality of materials used. Impurities cause the

formation of energy levels in the energy gap region resulting in a different conductivity and in a non-controlled behavior. These levels can also be metastable and, besides increasing the electronic noise since the electrons can be promoted in such levels due to thermal agitation, may lead to a slower collection of charge. A very high purity bulk, with no imperfections in the structure, will lead to a better performance.

4.3   SDD layouts

Thanks to the simplicity of their working principle, SDD can be designed in many different layouts suitable to a variety of application needs. Figure 4.4 shows a silicon wafer with a large variety of different SDD layouts, produced by Fondazione Bruno Kessler (FBK) within the research project ReDSoX.

Some different geometries are discussed in following subsections.
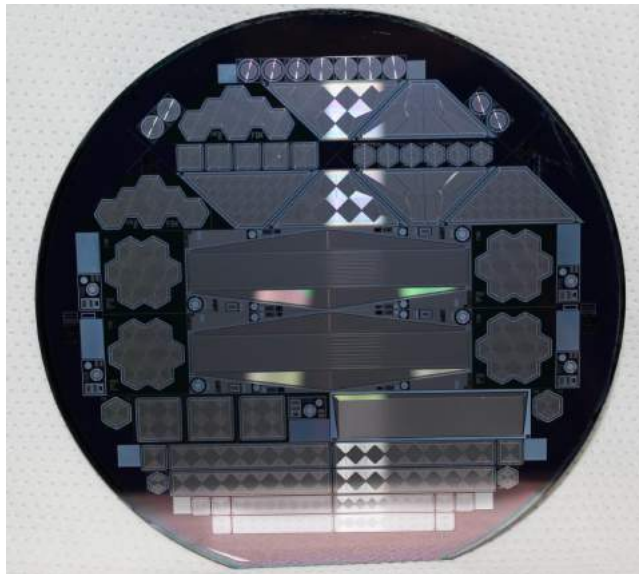
Figure 4.4: *This wafer is a FBK (Fondazione Bruno Kessler) production for the research projects ReDSoX.*

4.3.1 Single cell SDD

A single cell SDD can be considered the basic design, the fundamental building block from designing a matrix, i.e. several closely arranged single cells. Many layouts can be realized thanks to the great flexibility of this technology: from square to circular and hexagonal. The last one is the geometry of the basic cell that constitutes the detector under study in this thesis.

In Figure 4.5 some of the different single cell layouts realized using the SDD technology are shown.

(a)   (b)
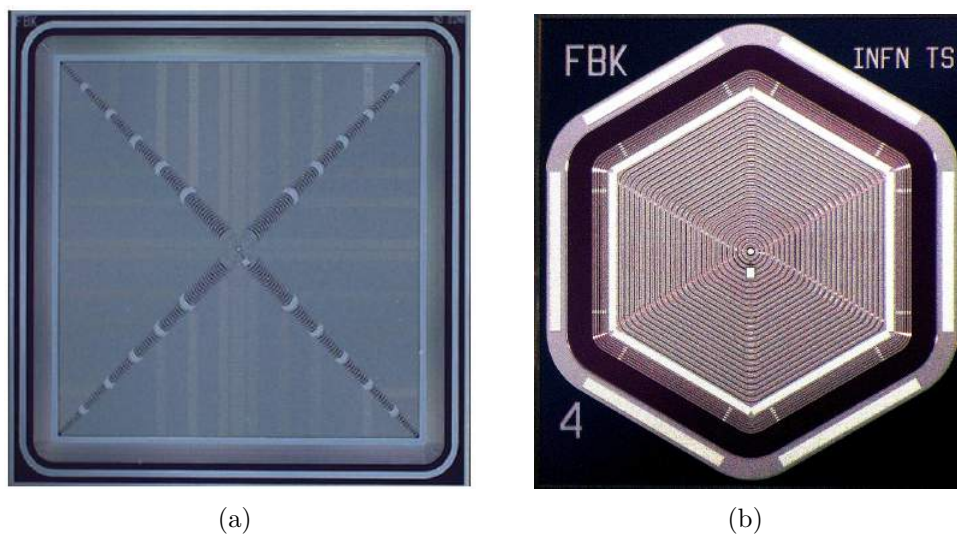
Figure 4.5: *(a) A square SDD layout. (b) An hexagonal SDD layout. It is the basic unit on which the matrix tested in this thesis is realized*

4.3.2 Large area SDD

As mentioned previously, the anode capacitance is independent from the active area of the SDD, so this type of technology is suitable to design large area detectors with a good noise performance.

An example of large area SDD is represented by the Alice-D4 SDD (Zampa et al., 2009) originally developed for particle tracking in the ALICE experiment of the Large

Hadron Collider (LHC) at CERN. The active area of the detector tile is 7.53×8.76 cm^2. The particular design of this detector is characterized by 256 anodes along the longest dimensions, with a pitch of 294 μm. Recently optimized for X-ray detection, this SDD layout has been employed as X-ray detector in the proposed medium class ESA-M5 space mission LOFT (Zampa et al., 2011).
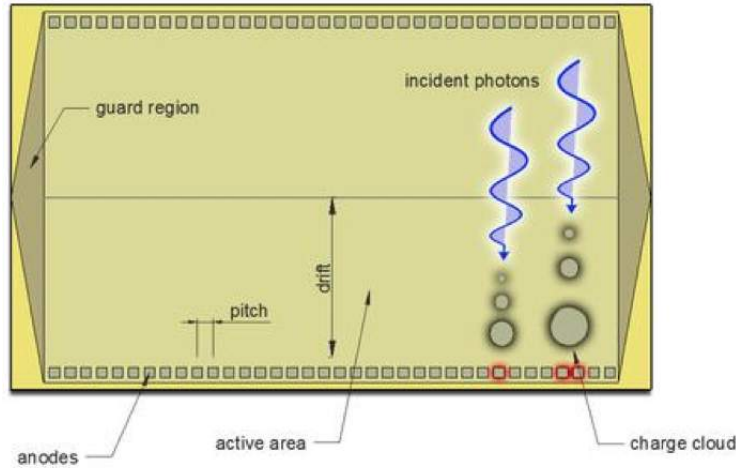
Figure 4.6: *Layout of the Alice-D4 SDD. The spreading of the electron cloud along its way towards the anodes is also represented.*

A schematic of the Alice-D4 SDD detector is reported in Figure 4.6. The drift field is "roof-shaped"with the higher voltage in the central region. This particular shape of drift field pushes the electron cloud towards the anodes, which are arranged in line on two sides of the device (Figure 4.6). Because of the diffusion mechanism, the electron cloud spreads with the time required to reach the anodes that is with the total drift distance:

$$\sigma = \sqrt{2Dt + \sigma_0^2} \tag{4.1}$$

where D is the diffusion coefficient, t the drift time and σ_0 is the (often negligible) initial cloud dimension.

With this layout, the sampling of the electron cloud by one or more anodes allows to derive information on the drift distance, and thus on the position of interaction

(Campana et al., 2011).

4.3.3   SDD matrices

If required by the application, ad in the case in which an array of scintillator bars should be read individually, a matrix layout can also be realized. It is also a large area system resistant to the presence of defects. In a matrix design, a single cell can be switched off in case of malfunctioning, at the cost of slightly lowering the effective area.
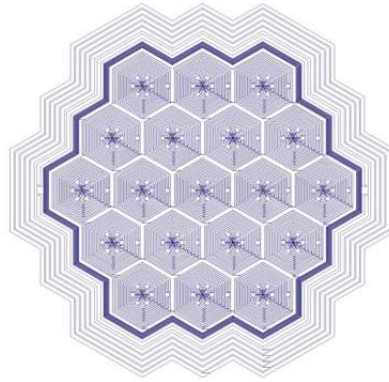
Figure 4.7: *A matrix layout realized by joining many hexagonal cells .*

Monolithic arrays of SDDs are of particular interest in high-resolution and high-rate X-ray spectroscopy. In fact, taking into account the already high-counting-rate capability of the single SDD unit (few hundreds kcounts/s for a typical area of 5 mm^2), the use of several units integrated in a segmented detector of relatively large area (few cm^2) could allow to achieve a counting capability of the whole detection system up to tens of Mcounts/s (Fiorini et al., 2005).

4.4   SDDs for γ-ray detectors

SDD are extensively used in the field of X-ray spectroscopy. However, they can also used for detecting optical photons. This characteristic also makes them useful as

read-out device for the light generated by scintillators. The PMTs have been since a long time the most widely used devices for this purpose. The high gain of the PMT makes the contribution of the electronic noise practically negligible. However, the statistical contribution, i.e the number of electrons detected, plays an important role: since the PMT has a low quantum efficiency (the last results in R&D of PMT lead to the production of detectors having a quantum efficiency of ∼30% in the range from 300 nm to 600 nm), this does not allow an efficient collection of the scintillation light.

The SDD coupled with low noise electronics and with a higher quantum efficiency up to ∼90% in the range from 450 nm to 1100 nm, are a very good candidate to replace the use of PMTs as read-out for scintillation light, as we will see in Chapter 6.

Chapter 5

Scintillators

Due to their typical thickness of $300 - 500$ μm, the SDDs are inefficient when the goal of the instrument is to detect photons with energies higher than 100 keV since they become transparent at these energies. Scintillators, typically thicker and with a high Z, are instead very sensitive to the high energy radiation. Therefore the coupling of scintillator with SDD appears to be an interesting solution for the design of a high-energy detector.

In this Chapter the general properties of scintillators, that is the other essential element of the technology studied in my thesis, will be presented. After introducing inorganic and organic scintillators, a particular focus will be set upon the cerium-activated lanthanum bromide ($LaBr_3(Ce)$), a recently developed scintillator used in my thesis work.

A scintillator is a material which emits light, typically in the visible or UV range, when a particle or a photon deposits energy into it. The underlying process is called *scintillation* which comes from the Latin word "scintillare". Under this term all the various physical processes that take place within a material which leads to light emission in a specific wavelength when excited by ionizing radiation are considered (§5.1).

5.1   Scintillation process

The energy released by the passage of charged particles or photons into a scintillator (Knoll, 2010) is converted into visible light. This property is referred as *luminescence*, but the physical emission mechanism is due to the phenomena of *fluorescence* and *phosphorescence*. Both are referred to the relaxation of an excited molecule and are distinguished by their temporal properties. In fluorescence the light is emitted immediately (from few ns to few μs), phosphorescence is, instead, characterized by far longer emission times because the excited state is metastable (i.e. longer lived due to the lower probability of transition to the ground state).

The number of photons N emitted in the scintillation mechanism can be described by linear superposition of two exponential decays:

$$N = A \exp\left(-\frac{t}{\tau_f}\right) + B \exp\left(-\frac{t}{\tau_s}\right) \tag{5.1}$$

where the decaying constants are referred to *fluorescence* and *phosphorescence* time characteristics of the scintillator material, referred also as slow and fast component, respectively, in Figure 5.1.

5.2   Organic and inorganic scintillators

Scintillation materials can be classified into inorganic and organic compounds, and can take the form of crystals, plastics and liquids.

Inorganic   In these scintillators the luminescence phenomenon is strictly correlated to their lattice structure. The energetic levels can be treated using band theory, in the same way as for the semiconductors described in Chapter 3.

For this reason, inorganic crystals can also be doped to modify their properties such as to reduce self-absorption and to change the intensity and wavelength of the emitted light according to the needs of different applications. The dopants, commonly called *activators*, create special sites in the lattice at which the band gap
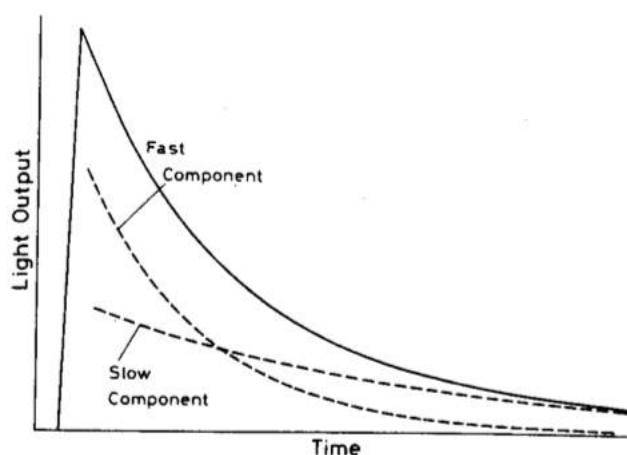
Figure 5.1: *The light yield as a function of time shows an exponential decay trend which is the sum of two contributions (solid line): the fast component (dashed line) is referred to the fluorescence emission, while the slow component (dashed line) is referred to the phosphorescence.*

structure is modified. New energy states are then allowed within what would be the forbidden band in the pure crystals.

Organic For organic materials, the process that leads to the emission of visible light is different with respect to the one which takes place in the inorganic ones. When a single particle passes through the material, the interaction occurs with the electronic and vibrational levels of a single molecule of the scintillator, and not with the energy bands relative to the entire crystal.

For this reason the organic scintillator can be present in different states of matter without changing its own properties. Organic scintillators may take forms of crystals, liquid and plastic. Liquid and plastic scintillator are, basically, solutions in a solvent that is liquid in the former case and a solid polymer in the latter. Organic scintillators are more malleable than the inorganic ones and their manufacture is commonly cheaper.

The main advantage of the inorganic scintillators when compared to the organic scintillators is their better energy resolution and greater stopping power. This derives

from their higher density (higher atomic number) and light output. Otherwise, they often are *hygroscopic*, a property which requires them to be housed in an air-tight enclosure to protect them from the damage due to the absorption of humidity, and have commonly higher production costs.

Scintillation in inorganic crystals is characterized by a typically slower time decay than in organic ones, ranging typically from a timescale of 30 ns for CeF_3 to 9000 ns for $CaWO_4$. Some exceptions characterized by a fast decay time, comparable with the organic scintillators, are also present.

5.3 Scintillator properties

Scintillators crystals are characterized by different properties that make each one unique for its own features. Since the scintillators are exploited due their light emission, the amount of light that the crystal releases isotropically is a parameter of primary interest, together with the wavelengths of emission and the decay time. Only a small fraction of the kinetic energy lost by a charged particle in a scintillator is converted into fluorescent energy. Most of the energy is dissipated non-radiatively, primarily in the form of lattice vibrations or heat.

The number of photons produced per unit of energy deposited in the scintillator is commonly referred to as *light yield*. The basic aim is to collect the largest amount of emitted light, so both self-absorption and the escape of photons from the scintillator surface have to be taken into account. Self-absorption, often negligible except for very large size scintillators, is due to the fact that the more the light has to travel through the crystal the higher is the probability to be re-absorbed by the crystal itself. To reduce escaping photons, an adequate wrapping, usually made of a reflecting material, is required to confine the photons inside the crystal, then decreasing the number of photon losses.

In order to convert entirely the energy of an incoming radiation into visible photons, the stopping power of the crystal is a fundamental parameter. Another parameter that has to be taken in account is the scintillator emission spectrum. The light emitted is usually peaked at a wavelength, although the entire emission is spreaded

around that value, as shown in Figure 5.2 in which some emission spectra of inorganic scintillators are reported.
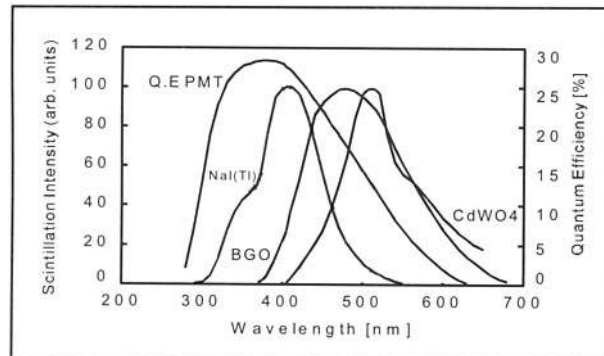
Figure 5.2: *Emission spectra of NaI(Tl), BGO and CdWO$_4$ scaled on maximum emission intensity.*

The ideal scintillator should possess the following characteristics:

- High stopping power.

- The light output response should be linear with the deposited energy.

- The material should be transparent to the wavelengths of its own emission.

Unfortunately, no material meets simultaneously all criteria, making the choice of a scintillator always a compromise.

5.4   LaBr$_3$(Ce)

The Cerium activated Lanthanium Bromide (LaBr$_3$(Ce)) is a newly developed scintillator crystal. It is characterized by an excellent quality in conversion efficiency, high effective atomic number and excellent linearity, making it one of the best performing scintillator crystals for spectroscopic purposes. Moreover, its very short decay time (between 14 ns and 60 ns, depending upon the concentration of cerium) is crucial
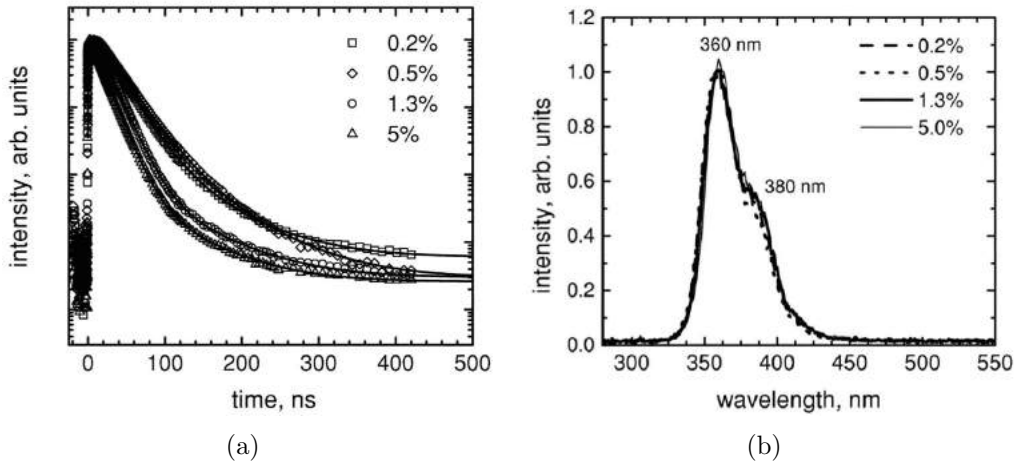
Figure 5.3: *(a) The light decay produced by a scintillator crystal* LaBr$_3$ *with Ce + dopant concentration of 0.2%, 0.5%, 1.3%, 5% (b) Emission spectrum of the crystal scintillator* LaBr$_3$(Ce) *with four different concentrations of cerium.*

for the contexts in which the rate of events to be measured is extremely high and an excellent temporal resolution as well as energy is required, e.g. in the case of the HERMES project (§2.2).

The amount of cerium dopant changes the fluorescence and phosphorescence decay constants of the scintillator modifying the temporal characteristics as shown in Figure 5.3a, but also the spectrum of emitted photons depends on the structure of the activation states of impurities in the crystal (Figure 5.3b)

The crystal was introduced in the market by Saint-Gobain[1] under the name of Brillance® 380 (where 380 refers to the wavelength of maximum emission expressed in nanometers). Table 5.1 shows the main characteristic of LaBr$_3$(Ce) and other commonly used scintillators.

The first fact that emerges from Table 5.1 is the high light yield: the LaBr$_3$(Ce) results in 63 photons/keV, that is almost 40% higher than the usually employed NaI, that because of its extensive use has become a reference standard. In addition to the excellent production of the scintillation light, the LaBr$_3$(Ce) has a high stopping

---

[1]http://www.crystals.saint-gobain.com/

Scintillator	Light Yield [photons/keV]	Decay time [ns]	Wavelength of maximum emission [nm]	Refractive index	Density [g/cm^2]
LaBr$_3$(Ce)	63	16	380	~1.9	5.08
CsI(Tl)	54	1000	550	1.79	4.51
NaI(Tl)	38	250	415	1.85	3.67
BaF$_2$	1.8	0.7	~210	1.54	4.88
BGO	9	300	480	2.15	7.13

Table 5.1: *Main scintillator characteristics*

power: with a density 5.08 g/cm^3, it has a higher efficiency than both sodium iodide, CsI (Tl) (+43 %) and barium fluoride, BaF (+8 %).

Another important feature of the LaBr$_3$(Ce) is the high linearity of the scintillation light yield at different energies. Both the high light output and good linearity make the energy resolution of LaBr$_3$(Ce) the best among those of scintillators on the market.

An ideal LaBr$_3$(Ce) scintillation crystal would be composed entirely of stable isotopes such as ^{139}La. Unfortunately there is inevitably some amount of contamination with the naturally occurring radioactive elements and isotopes. In these detectors the primary concern is the contamination with naturally occurring radioactive ^{138}La (0.08881% abundance). This means that these crystals will occasionally detect their own decay products. Recent work by Cre (2009) has found the internal activity in the range of 0.07 – 3 MeV to be ~4.4 cts/s/cm^3. This is sufficient to interfere with any long-term energy measurements but should not affect the scintillator ability to make precision fast-timing measurements.

An alternative to the LaBr$_3$(Ce) is given by the commonly used thallium-activated caesium iodide (CsI(Tl)). Its density and the refractive index do not differ much from those of LaBr$_3$(Ce) (Table 5.1) and its light output is second only to the latter. The maximum of its emission spectrum suggests a better match with the silicon detectors, since their quantum efficiency reach the maximum values in the same range of CsI(Tl) emission wavelengths. However, the long timescale of the CsI(Tl) light emission does

not make it suitable for missions in which timing accuracy is an essential element
(i.e. HERMES).

Chapter 6

Characterization of the detector prototype

In this chapter the experimental work on the characterization of the γ-ray detector prototype realized coupling a LaBr$_3$(Ce) scintillator crystal with a matrix of hexagonal SDDs will be described.

A preliminary analysis was conducted in order to ensure the correct functioning of the SDDs (§6.3.1). After the optical coupling with the scintillator crystal, the characterization using X-ray (§6.3.3) and γ-ray sources (§6.3.4) is performed. Furthermore, the timing performance of the device is analyzed (§6.4).

The SDD array has been developed and realized for X-ray applications within the ReDSoX (REseach Drift for Soft X-rays) collaboration[1] in a synergy between INFN-Trieste and Fondazione Bruno Kessler (FBK)-CMM (Trento, Italy). It is made of 7 hexagonal SDD cells organized in a radial geometry (Figure 6.1a and Figure 6.2a). The device is 450 μm thick and a single cell has an active area of 30 mm^2, with a total sensitive area of 210 mm^2.

The scintillator is a commercial cylindrically shaped LaBr$_3$(Ce) (Figure 6.1b) produced by Saint Gobain (BrilLanCe™380), with a 0.5" diameter and 0.5" height. LaBr$_3$(Ce) is a hygroscopic crystal, thus it is encapsulated in a hermetically sealed

---

[1]`http://zoidberg.iaps.inaf.it/redsox/`

(a)	(b)
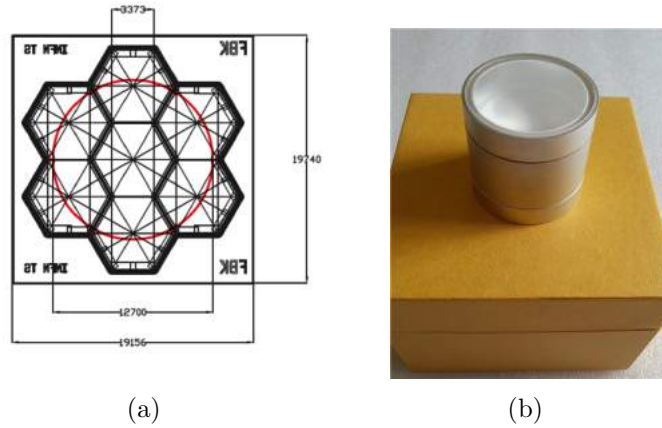
Figure 6.1: *(a) Schematic representation of the SDD matrix. The geometry of the device is optimized for the coupling with a 0.5" diameter scintillator crystals. Channel #1 is the central one, all the others are numbered clockwise starting from the top (central) cell that corresponds to Channel #2. The red circle encloses the region that will be covered by the crystal once the coupling is realized. (b) The $LaBr_3(Ce)$crystal in its protective casing.*

aluminum container to be protected from humidity. A reflector material is placed between the scintillator and the container walls and an optical window is incorporated into one end.

Figure 6.1 shows that only the central SDD cell is fully covered by the crystal. The fractional covered area of the other cells can be analytically calculated and is of 55.6% assuming a perfect alignment.

Each single cell is equipped with a discrete-component Charge Sensitive Preamplifier (CSP) designed and realized at INAF/IASF-Bologna. The anode capacitance is of the order of tens of fF, and a few mm of a 20 μm diameter wire will add a stray capacitance larger than the anode one, degrading the noise performance as explained by Equation 3.13. Thus, the first stage of the preamplifier, a JFET with a backgate (§3.2.1), is placed very close to the anodes. In this way the rest of the CSP can be arranged few mm farther. To ensure the mechanical protection and electromagnetic shielding, the entire device is placed inside an aluminum case. At the entrance window of the matrix, a hole has been cut on the aluminum case and covered with aluminum tape ($\sim$100 μm thick) to ensure light shielding.

(a) (b)
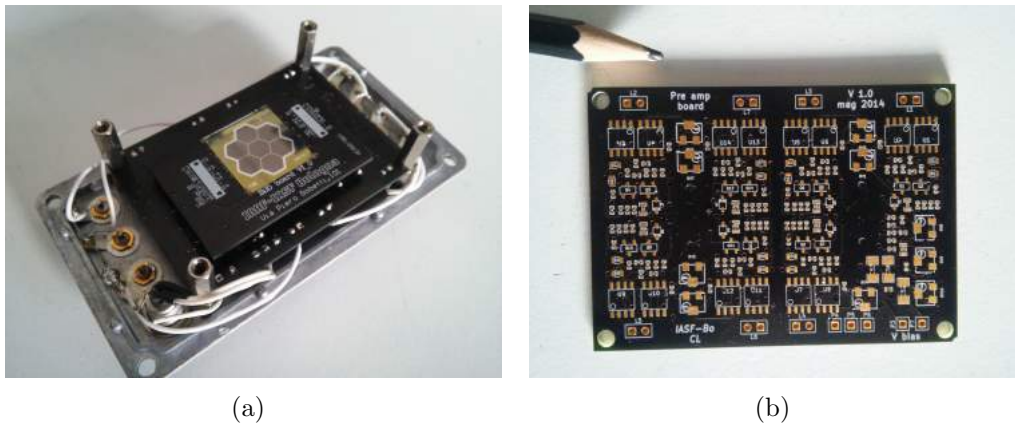
Figure 6.2: *(a) The SDD matrix already mounted on the JFET board. (b) The board on which the seven preamplifiers bonded with each channel are integrated.*

The characterization of the whole device has been carried out with both an analog and a digital setup. Since digitizers are a relatively new technology, this characterization has been made with the explicit purpose of allowing a comparison between the performance of a digitizer plus digital analysis of the signal and the classic analog acquisition chain.

6.1 Analog setup

In the analog setup, shown in its entirety in Figure 6.4a, the output signal from the preamplifier is connected to a custom board realized at IASF-Bologna. The board hosts an housing for a commercial analog Gaussian shaping amplifier module (Figure 6.3a) designed by Cremat[2], a *peak and hold* system that can be operated either in self-triggered mode or forced with an external trigger.

Once the signal is shaped by the Cremat module, the peak and hold circuit locates and keeps the maximum amplitude value of the shaped signal for ∼75 μs, that is the time needed to the ADC to sample all signals. The result is then sent to an acquisition software that has been specifically designed using the graphical

---

[2]http://www.cremat.com

(a) (b)
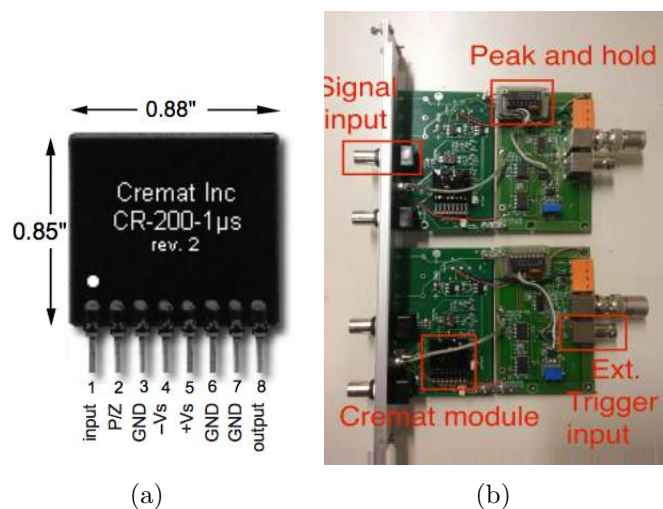
Figure 6.3: *(a) An example of the Cremat modules used. The one in figure is relative to a shaping time of 1 µs. (b) The figure shows a single element in which two boards are set. The key elements are highlighted by red boxes.*

programming language LabVIEW[3].

In order to maintain the experimental equipment as compact as possible, NIM modules (which are a standard for electronics in nuclear physics experiments) are exploited to house two of the custom boards (Figure 6.3b). Since the output of each preamplifier is directly sent to a board, a total of 4 NIM modules are used and housed in a standard NIM crate (Figure 6.4b).

The acquisition is configured so that every time a cell detects a signal all channels are acquired. This is achieved thanks to a custom *OR logic board*, realized at IASF-Bologna, also housed in the same NIM crate. Every time a channel is self-triggered the OR board forces the acquisition for all channels.

6.2 Digital setup

In the digital setup (Figure 6.5a), the output signal from the pre-amplifier is sent to a PXI-5105 digitizer realized by National Instruments (Figure 6.5b). The digitizer

---

[3]http://www.ni.com/labview/i/

(a)

(b)
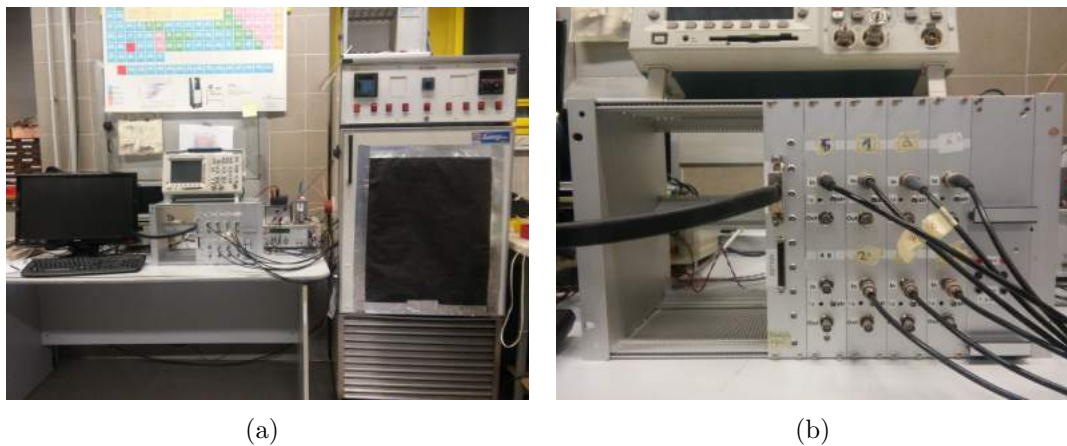
Figure 6.4: *(a) The analog setup adopted. (b) A detail of the NIM crate used with the 4 NIM modules.*

(a)

(b)
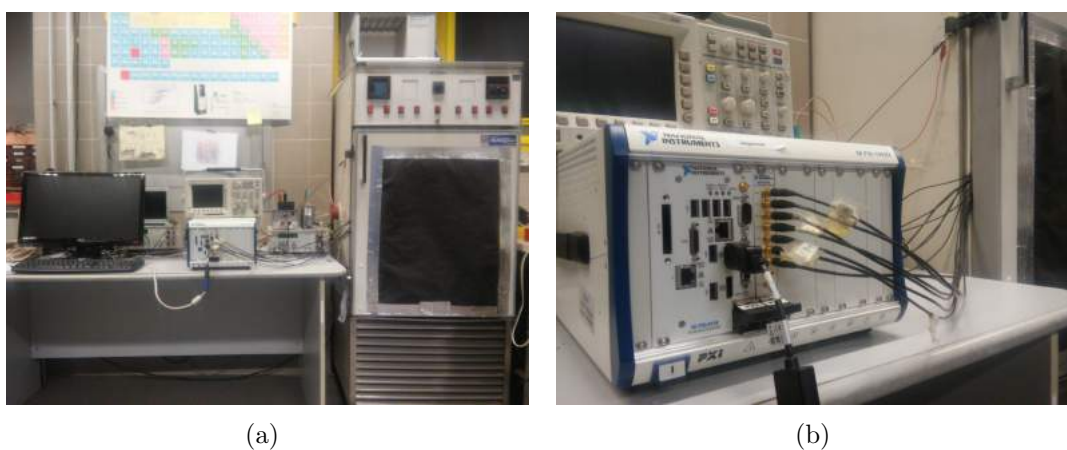
Figure 6.5: *(a) The digital setup adopted. (b) A detail of the NI PXI 5105 digitizer.*

allows the simultaneous sampling of 8 channels with a 12-bit resolution at a maximum sampling rate of 60 Mhz.

Each signal is thus digitized and stored in memory allowing to perform any type of off-line software analysis. The shaping of the signal is handled via a software developed by me that applies the *trapezoidal digital filter* (§3.2.5). An example of a trapezoidal shaped signal is shown in Figure 6.6 where it is superimposed to its raw waveform. Since the waveform signal is stored in a file, it is possible to apply different versions of the shaping algorithm many times on the same signal.
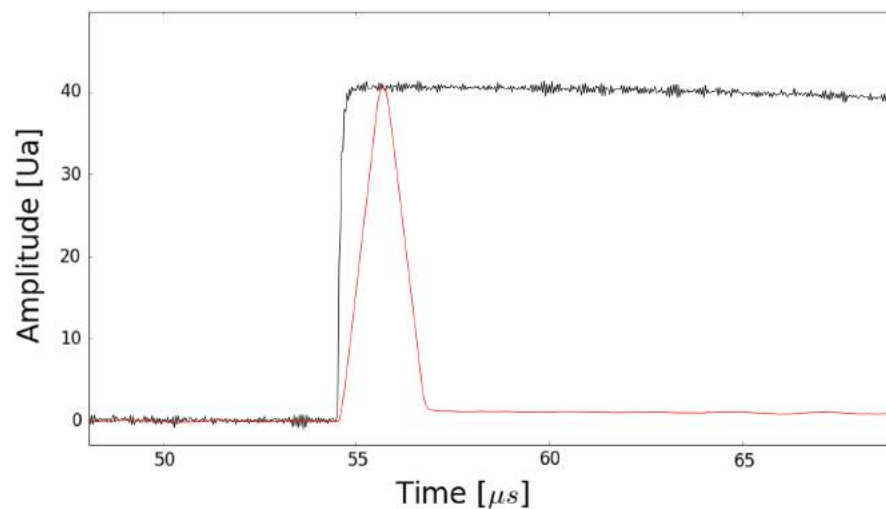
Figure 6.6: *A digitized waveform from an X-ray event (black line) and the shaped trapezoidal signal (red line). The shaped signal maintains the amplitude of the X-ray event signal and improves the signal-to-noise ratio.*

The digital setup, composed of a digitizer and a shaping software, allows us to replace the use of Cremat modules, the peak and hold system and the MCA, that is the whole NIM module, plus the PC. In this case the OR logic that allows to force the acquisition for all channels is already present in the digitizer.

The analog setup is obviously limited by the physical nature of the instrumentation: the available shaping times are limited to those on the hardware. The digital chain additionally provides a striking advantage over the use of the analog chain, as

we have seen (§3) with a single measurement an almost infinite series of analyzes on the same data can be performed without compromising them.

6.3 Working method and data analysis

6.3.1 Preliminary analysis

The first step of the characterization of the SDDs matrix is the *calibration*. The calibration consists in the determination of the detector response to the different absorbed photon energies. The detector is usually stimulated, in all its energy range, by monochromatic sources which emit photons with a-priori known energies. The response of the generic spectroscopic detector is a voltage signal with an amplitude related to the energy released in the sensitive volume of the device. In the case of solid state device, such response is usually calibrated in energy or in number of electrons (e^-) since this represents a deterministic way to express amplitudes.

The detection efficiency of the SDD to high-energy photons is reported in Figure 6.7. It shows an efficiency close to 100% for photon energy from 1 to 10 keV, although there are also absorptions due to dead layers. However, the efficiency drops below 10% at energies close to 30 keV because the thickness of the SDD is not enough to stop high-energy photons. The radioactive source to be used to perform the calibration should therefore have emission lines in the energy range of few tens of keVs.

Before the calibration, it is fundamental to ensure the correct operation of the detector and associated electronics. As a first step, using the analog acquisition chain, the detector was irradiated at room temperature with a ^{241}Am source that, as shown in the Table 6.1, has several emission lines in the range of interest.

According to the theory, the equivalent noise charge (ENC, §3.1.4) depends on the shaping time τ. To evaluate the performance of the device, the following shaping times were investigated with the analog chain: 0.25, 0.5, 1, 2 μs. They are the only ones available. To modify the shaping times of the analog setup means to manually replacing the seven Cremat modules, and to repeat the measurement for

X-ray from ^{241}Am		
E [keV]	I (%)	Assignment
11.871	0.66	Np L_l
13.761	1.07	Np L_{a2}
13.946	9.6	Np L_{a1}
15.861	0.153	Np L_h
16.109	0.184	Np L_{b6}
16.816	2.5	NpL_{b2}
17.061	1.5	Np L_{b4}
17.505	0.65	Np L_{b5}
17.751	5.7	Np L_{b1}
17.992	1.37	Np L_{b3}
20.784	1.39	Np L_{g1}
21.099	0.65	Np L_{g2}
21.342	0.59	Np L_{g3}
21.491	0.29	Np L_{g6}
Gamma-ray from ^{241}Am		
E [keV]	I (%)	Decay mode
26.3448	2.40	α
59.5412	35.9	α

Table 6.1: *In the table the intensities I of each line expressed as a percentage of the total emission of the source are reported (`http://nucleardata.nuclear.lu.se/toi`). The last column for the X-ray table reports the associated transition in the emission of the X-ray. For the γ-ray case, the same column reports the decay mode.*
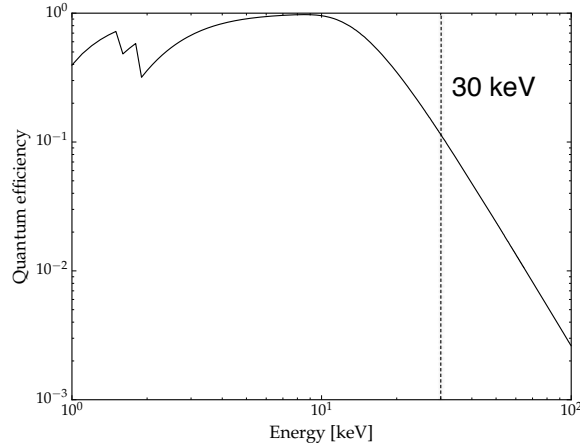
Figure 6.7: *The SDD quantum efficiency in the range 1–100 keV.*

each configuration.

In Figure 6.8a the ^{241}Am raw spectrum of channel #1 obtained at 0.5 μs is reported as typical case. Figure 6.8b shows instead a defective behavior of channel #2 at the same shaping time. This will be discussed in the following.

To determine the energy resolution of each channel at different shaping times, it is necessary to calibrate in energy the spectra in order to define the conversion factor and correct any offset. To perform the calibration, in the spectrum the energy peaks at 13.9 keV, 17.8 keV, 26.34 keV and 59.54 keV have been identified. A Gaussian fit has been performed on the peaks to evaluate centroid positions and FWHMs using a custom software that we have developed in *Python* for this purpose. Using the following equation, a linear fit to the four centroids has been done

$$E = G \cdot C + O \qquad (6.1)$$

(a) (b)
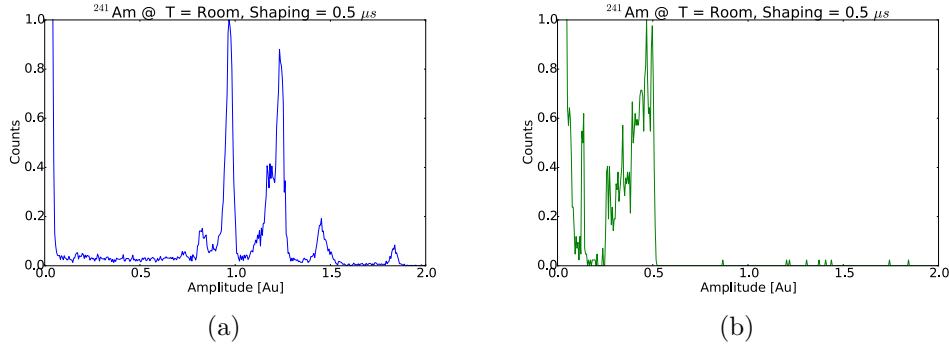
Figure 6.8: *(a) The ^{241}Am raw spectrum of channel #1 obtained at 0.5 μs at room temperature. It is expressed in Arbitrary Units [Au]. (b) The ^{241}Am raw spectrum of channel #2 obtained in the same conditions. It is evident its defective behavior since the spectrum acquired does not show any of the spectral features of ^{241}Am.*

where E is the energy, G is the calibration coefficient, C is the channel expressed in arbitrary units (i.e. the digitizer pulse height amplitude) and O represent the offset expressed in energy.

To study the linearity of the energy response of the SDD, we have calculated the residuals using $\frac{x_i - x_{\text{Model}}}{x_{\text{Model}}}$, where x_i is the centroid position measured and x_{Model} is the result of the linear fit. In Figure 6.9 the calibration line of channel #1 and the residuals expressed in percentage are reported. The other channels show a similar behavior and therefore are not reported here. All the residuals are within a maximum dispersion of 0.5% from the calibration line. This means that the energy response of the SDDs is as a very good approximation linear.

Given the preliminary nature of this calibration, whose goal is to perform a functional analysis of the device, we report only an example of the energy calibrated spectrum of channel #1 in Figure 6.10.

The energy resolution (FWHM) in percentage is obtained using Equation (3.6) where the centroid and the widths are estimated by a Gaussian fit on the 13.9 keV energy peak (which is the most intense line among those detected and the less influenced by the presence of multiple lines) performed using the custom software. The line observed at 13.9 keV is actually a blend of two lines: 13.761 keV and 13.946 keV,
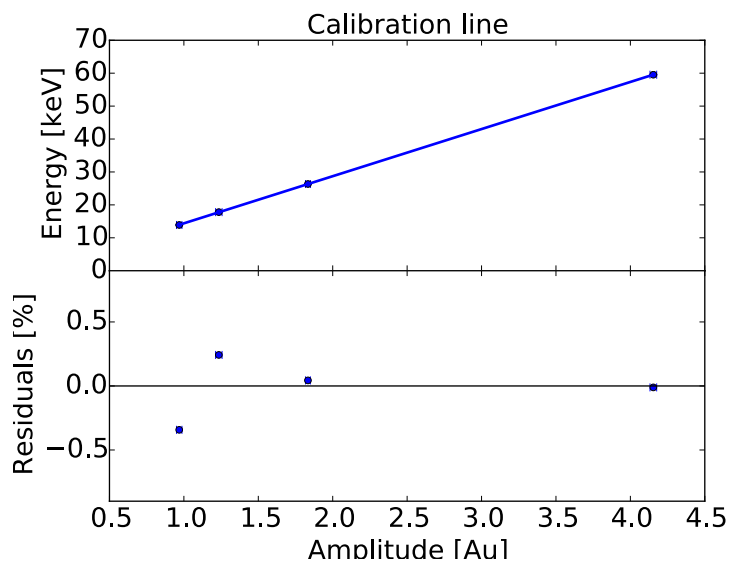
Figure 6.9: *The calibration line of channel #1 (upper panel) and the residuals expressed in percentage (bottom panel).*
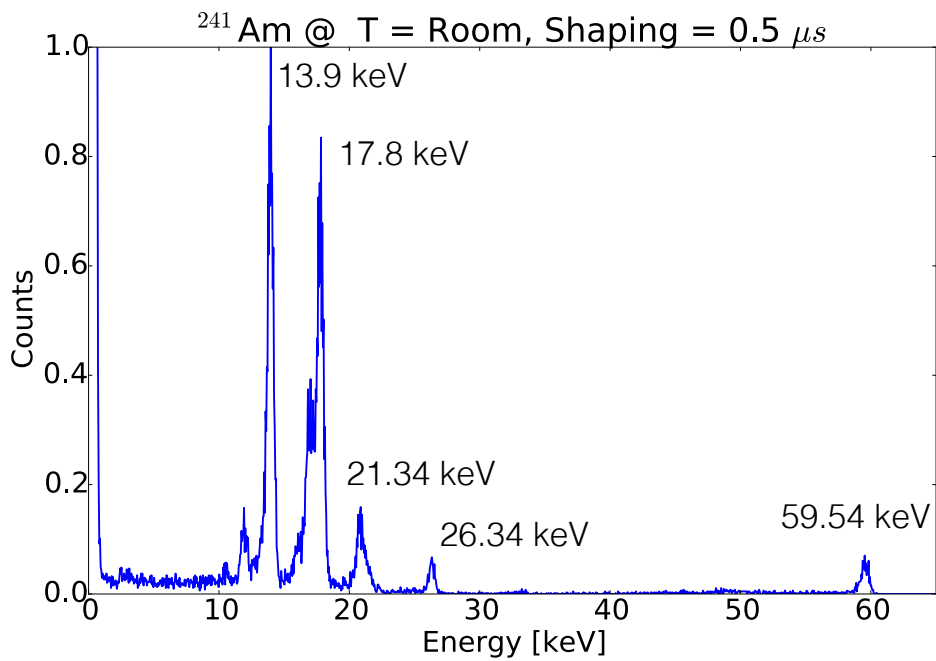
Figure 6.10: *The energy-calibrated spectrum of channel #1 at a shaping time of 0.5 μs.*

which differs by ∼200 eV. The former line contributes to the total amplitude of the blend by a ∼10%, while the latter represents the remaining ∼90%. Therefore the contribution of the less intense line does not broaden significantly the total FWHM and thus can be neglected. The only two lines that are not involved in narrow multiplets are those at 11.871 keV and 59.54 keV, but they have a too limited statistics to be exploited here for the resolution calculation.

The "noise figure" showing the resolution at different shaping times (Figure 6.11) is used to identify the shaping time corresponding to the best noise performance at room temperature.
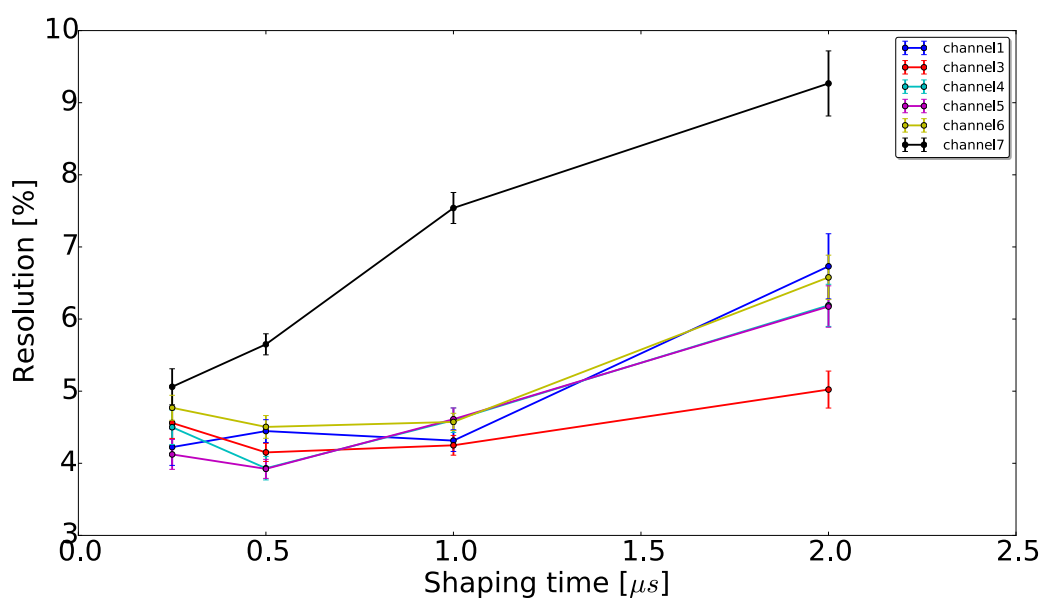
Figure 6.11: *Energy resolution at different shaping times for each channel obtained at room temperature. Channel #2 is missing since its malfunctioning over each shaping time made impossible its calibration.*

A defective behavior of channel #2 is evident from Figure 6.8b. As mentioned in Section 4.2, imperfections in the Si crystalline structure of the SDD cell may alter its electrical behavior generating a high dark current. This current may be also high enough to induce saturation in the preamplifier affecting its proper operation. The number of charge carriers that are in the conduction band due to thermal excitation,

thus contributing to the dark current, is given by:

$$N = Ae^{-\frac{E_G}{kT}} \tag{6.2}$$

where N is the number of charge carrier in the conduction band, A is a constant, E_G is the energy gap between the valence and the conductive band, k is the Boltzmann constant and T is the temperature. Reducing the operational temperature of the device results in a lower dark current. In the case of Si, for every temperature decrease of 7 °C the value of N and thus of the current is halved. A way to verify the hypothesis on the defective behavior of channel #2, i.e. that the preamplifier is saturated by a too high dark current, is to place the device inside a climatic chamber at $T = -10$ °C. This would reduce the number of the charge carriers in conduction band by a factor of $\sim$5. If the preamplifier is saturated, a lower current may bring it back to its correct operating point.

The ^{241}Am radioactive source was also placed in the climatic chamber and the Cremat modules were chosen in order to shape the preamplifier signal at 0.5 μs, which is the value for which the majority of the channels provide the best performance (Figure 6.11). The measurements are reported in Figure 6.12.

The lower operating temperature, as expected, results in a lower dark current. Channel #2 now shows the same behavior as the other channels, confirming the hypothesis of its higher dark current. Of course, the higher current produces a worser spectral resolution with respect the other channels.

In order to have a correct functioning of channel #2 also at room temperature, it is necessary to modify the preamplifier operating parameters, specifically, the JFET operating voltages.

As anticipated in §3.2.1, the JFET governs the current within the preamplifier by means of the gate voltage. In this case, however, the gate of the JFET used is directly connected to the anode of the SDD making the voltage unmodifiable. To carry out this kind of operations, the JFET used is provided with a second gate, called *backgate*, whose voltage variation produces the same effect that would be obtained by directly modifying the gate voltage.
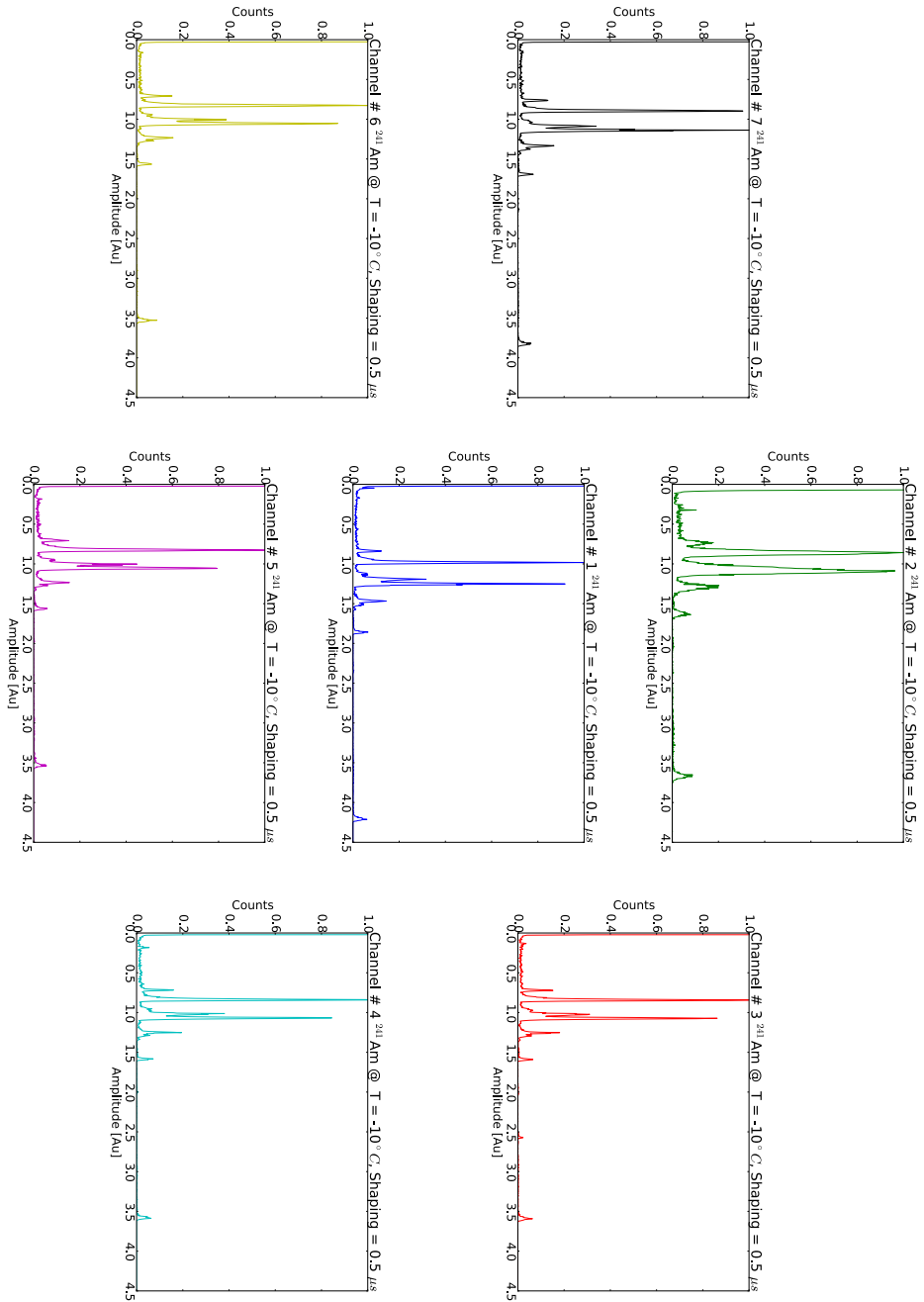
Figure 6.12: *The* ^{241}*Am spectra obtained from each SDD array cell at a shaping time of 0.5 μs after placing the detector inside the climatic chamber at a temperature of -10 ° C. The color are used to facilitate the immediate identification of the different channels: #1 blue; #2 green; #3 red; #4 light blue; #5 violet; #6 yellow; #7 black.*
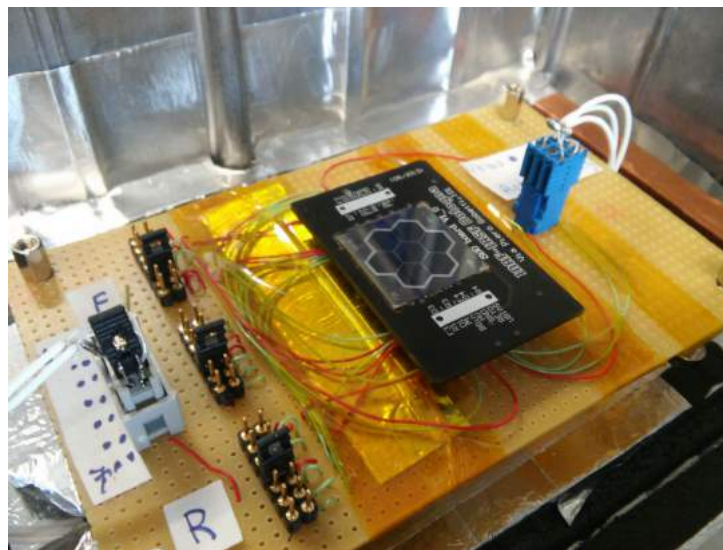
Figure 6.13: *The SDDs matrix placed on the test equipment used to set the preamplifier working parameters in real time.*

The device was then placed on the test equipment shown in Figure 6.13 and exposed to ^{241}Am. Observing the output via an oscilloscope, the backgate voltage was modified in order to lower the flowing current. The spectral measurement were then repeated and a proper functioning of the channel #2 was observed even at room temperatures.

6.3.2 Performance of the digital chain

Investigating different shaping times via the analog chain results to be quite time consuming since it implies a continuous disassembling and reassembling of components and new measurements.

The use of a digital spectroscopic chain would reduce enormously the time required since it would be sufficient to take the acquisition only once and then execute the digital analysis offline, at a later time. Furthermore it does not limit the choice of shaping time values. Since the main goal is to reach high spectroscopic performance, it is fundamental that the digital chain does not result in a lower energy resolution.

The device was placed again in the climatic chamber at a temperature of $-10\,°C$ and the analog chain was replaced by the digital one to make a performance comparison. I implemented in Python the algorithm for the trapezoidal shaping described in §3.2.5. This software allows us to shape the digitized waveform to a trapezoidal shape and is also used to replace the MCA, allowing to produce the final spectrum. The shaping time is defined, in this particular case of digital shaping, as the rise time plus half flat-top time (Figure 6.14).
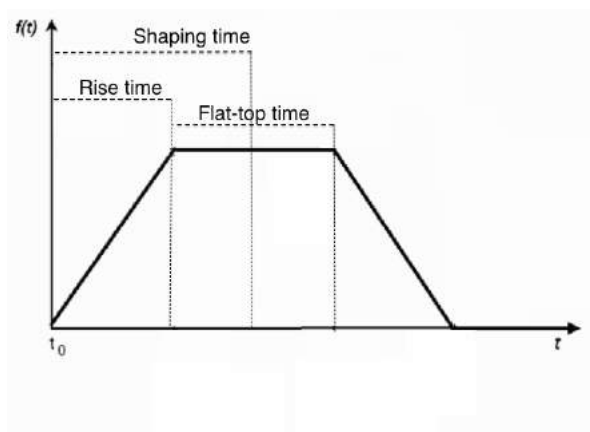
Figure 6.14: *An example of a trapezoidally shaped signal. The time intervals that define the rise time and the flat-top time are identified by the dashed lines.*

In Figure 6.15 both analog and digital ^{241}Am X-ray spectra of the Channel #1 obtained with the same shaping time, i.e. 0.5 μs, are shown.

(a)

(b)
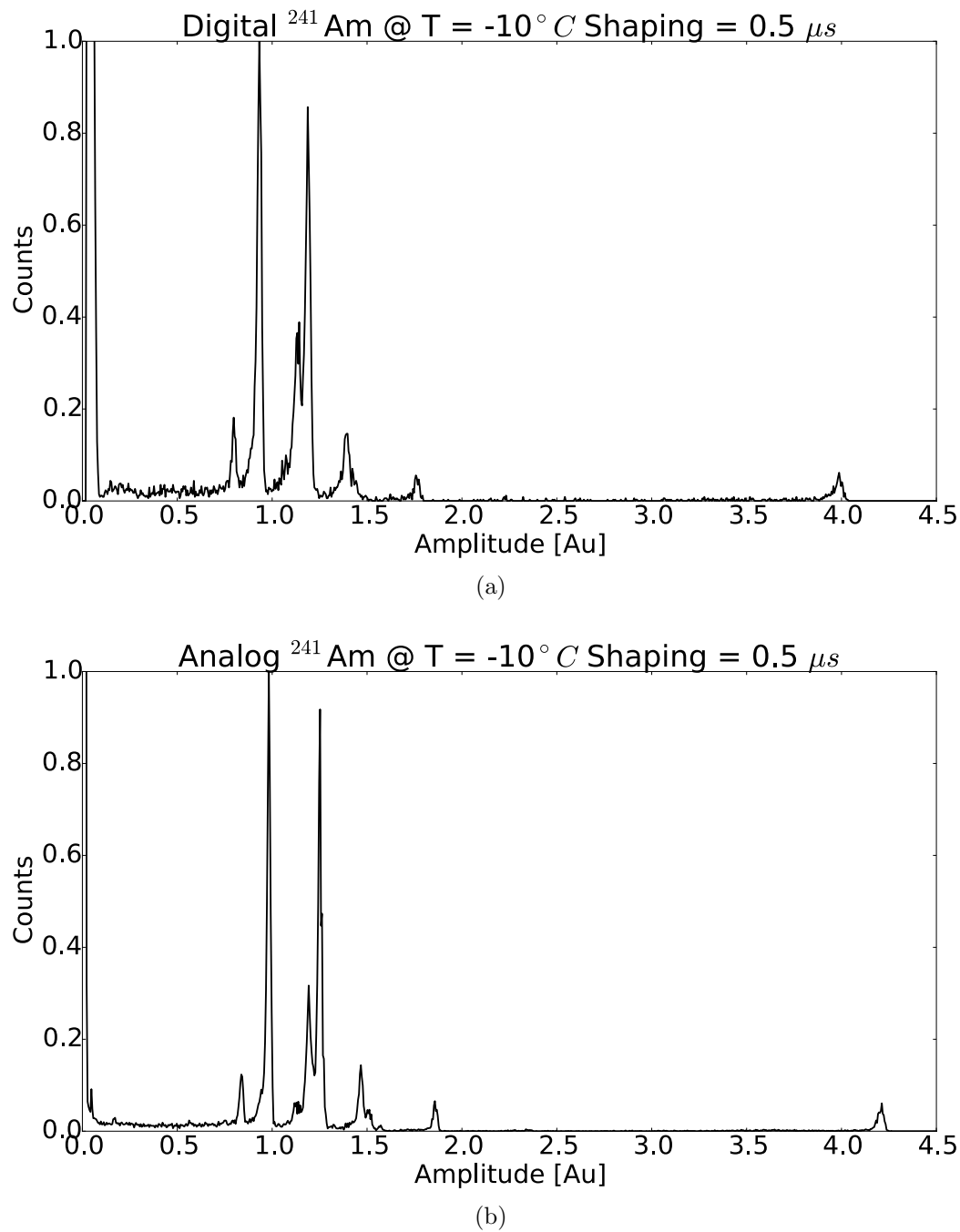
Figure 6.15: *(a) The* ^{241}Am *obtained with the digital setup (b) and* ^{241}Am *obtained with the analog setup. Both spectra are normalized to the amplitude of the 13.94 keV line. Measurements were performed at* $T=-10\ ^\circ C$ *in both cases.*

The line width obtained by fitting the 13.9 keV line can be adopted to make a comparison between the performance of the two adopted setups. The widths must be relative to the same shaping time to allow a proper comparison. For the analog setup, a FWHM of 581 ± 44 eV is measured against 609 ± 34 eV for the digital setup. The two values are consistent within the errors, i.e. at the 1σ level. This shows how the digital setup, despite being a relatively new technology, can already provide results that are comparable with those obtained by reliable and widely used analog setups.

Despite the analog chain shows a slightly lower noise, the advantages provided by the digital one let us to prefer the use of the latter class of chain. For this reason, in the following of this thesis, only data acquired by the digital setup will be reported.

6.3.3   X-ray characterization

Since the operating parameters of channel #2 have been changed in order to define the correct operating points for each channel, the calibration has to be performed again. However, before this step, the scintillator crystal was optically coupled to the SDD matrix (the specification about the coupling with the crystal is described in the next subsection). The detector was then placed inside an aluminum case that, as shown in Figure 6.16, presses the two components together in order to achieve a better optical coupling.

The ^{241}Am source can no longer be used to stimulate directly the SDDs matrix, since the crystal is placed on the entrance window, stopping almost all the X-rays lines from ^{241}Am. On the other side of the SDD, the aluminum case and the preamplifier board constitute insurmountable passive layers for most of the X-ray photons. Therefore, it is needed to use a source that emits higher energetic lines enough to overcome these passive layers, but not too much in order to be detected in the relatively thin Si bulk. For this purpose a ^{133}Ba radioactive source has been chosen. The main emitted lines under 100 keV are reported in Table 6.2.

The main lines are at 30.85 keV (multiplet of 3 lines: 30.279 keV at 0.004% that we can consider negligible; 30.62 keV at 34.9% and 30.97 keV at 64.5%), 34.96 keV

X-ray from ^{133}Ba		
E [keV]	I (%)	Assignment
30.270	0.00401	Cs K$_{a3}$
30.625	34.9	Cs K$_{a2}$
30.973	64.5	Cs K$_{a1}$
34.920	5.99	Cs K$_{b3}$
34.987	11.6	Cs K$_{b1}$
35.252	0.123	Cs K$_{b5}$
35.818	3.58	Cs K$_{b2}$
35.907	0.74	Cs K$_{b4}$
Gamma ray from ^{133}Ba		
E [keV]	I (%)	Decay mode
53.161	2.199	e
79.6139	2.62	e
80.3971	34.06	e

Table 6.2: *In the table the principal emission lines from X-rays and γ-rays produced by ^{133}Ba are reported. The last column for the X-ray table represents the associated transition in the emission of the X-ray. For the γ-ray case, the same column reports the decay mode, where e stands for electron-capture.*
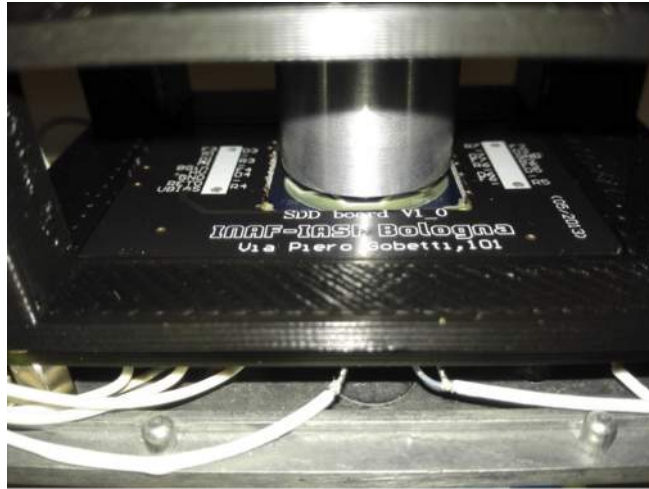
Figure 6.16: *The cylindrical encapsulated crystal is pressed towards the SDD matrix in order to perform a better optical coupling.*

(blend of 2 lines: 34,920 keV at 5.99% and 34,987 keV at 11.6%) and 80.39 keV. As shown in Figure 6.7, the SDDs are not very efficient at energies above 30 keV but with long measurements sufficient statistics can be achieved. Since the measurements made with the ^{241}Am spectrum have already demonstrated the linearity in the energy response of the SDDs, these three lines are enough to link the energy deposited in the device to the detector signal amplitude via a linear fit.

The entire characterization has been realized after placing the device in a climatic chamber at T ~ -20 °C. In Figure 6.17 an example of a raw ^{133}Ba spectrum is reported. We observe that the 80.39 keV line shows a much lower intensity with respect the 30.85 keV multiplet. This may seem to disagree with the value reported in Table 6.2 according to which the 80.39 keV line should show almost the half of the intensity of the 30.85 keV multiplet. However, the measured intensity is justified by the low detection efficiency of the SDD at such energies.

The ^{133}Ba source used is unfortunately characterized by a low activity, therefore the measured spectra show a lower statistics with respect the ^{241}Am using the same acquisition time of 25 minutes. However, this is not a problem for what regards the X-ray calibration since the statistics is sufficient to identify the centroids of the lines.
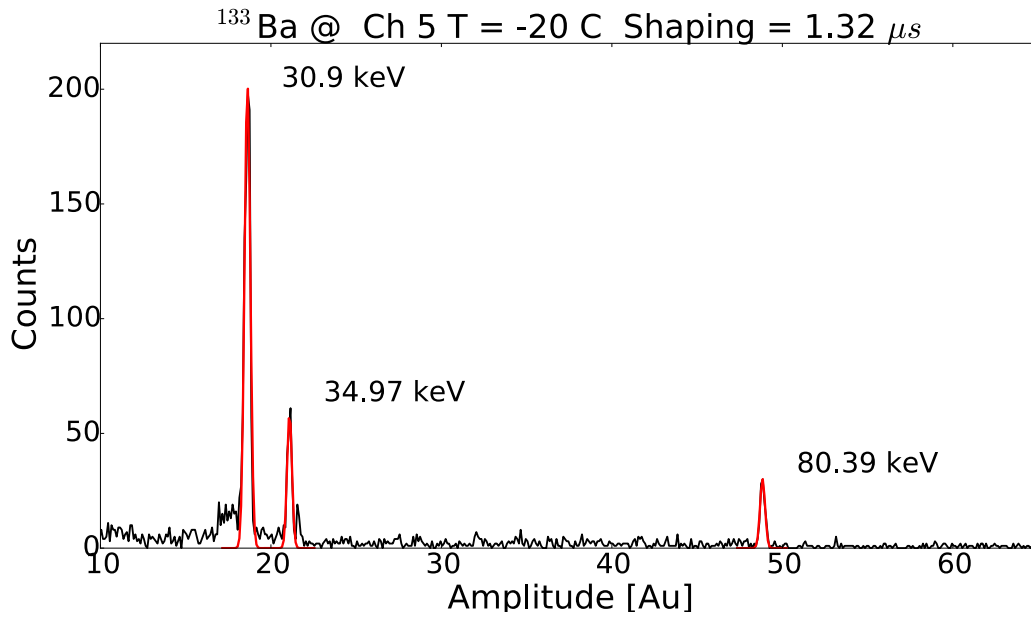
Figure 6.17: *A typical ^{133}Ba spectrum obtained with the digital setup with superimposed the performed Gaussian fit (red features).*

Since the shaping time influences the amount of signal collected and therefore its amplitude, the calibration has been performed for each shaping time investigated.

The offset and calibration coefficient values obtained are reported in Table 6.3. Since large amounts of shaping times are investigated[4], only the values relative to the best noise performance (described in the following §3.1.4) are reported in the Table. Using these coefficients it is possible to calibrate the acquired spectra in energy.

The calibration coefficients and offsets measured are comparable within few %. This shows an uniformity in the preamplifiers behavior.

The detector response can also be expressed in terms of electrons generated by a given energy deposit, using the equation $N = E/w$, where w is the mean energy necessary to generate an electron-hole pair ($w = 3.6$ eV/e$^-$ for Si). The calibration in electrons is extremely useful when the detector is operated also as a photodetector for the scintillation light, because it provides a unique way to express the signal

---

[4]A table like Table 6.3 is generated for each point

	Linear Fit report		
Channel	Calibr. coeff.	Offset	Best shaping time [μs]
1	1.3943 ± 0.0043	0.081 ± 0.001	1.65
2	1.4139 ± 0.0032	0.3635 ± 0.0027	0.264
3	1.5981 ± 0.0012	0.0582 ± 0.00034	1.32
4	1.6414 ± 0.0022	0.3898 ± 0.021	0.66
5	1.6221 ± 0.0046	0.4298 ± 0.052	1.65
6	1.4276 ± 0.0089	0.3899 ± 0.076	1.65
7	1.6997 ± 0.013	0.3374 ± 0.005	1.65

Table 6.3: *In the table we report, with the associated uncertainties, the values of the calibration coefficient and the offset obtained as result of the linear fits. The best shaping time value for channel #2 is lower than those of the others channels. This is due to its higher dark current level that provides a higher series noise contribution.*

regardless of the fact that the high-energy photon has interacted with SDD or the crystal. This is because a given signal amplitude can be generated by photons of different energies depending on whether the energy was directly deposited in the SDD or the in scintillation crystal, producing optical photons in the latter case.

In Figure 6.18 we report the same ^{133}Ba raw spectrum calibrated in both energy and number of electrons.

Once the spectra are calibrated in electrons, we can derive another useful quantity to characterize the system, the ENC. To estimate the ENC of the system, a Gaussian fit has been performed to the 30.85 keV multiplet. The other two available lines were discarded, because the line at 34 keV is also a blend of lines but has a lower statistics compared to the 30.85 keV line. The 80.38 keV line, although not a blend, has too low statistics. Only the 30.973 keV line is used to derive the ENC since it is the one with the higher statistics compared to the other lines that form the 30.85 keV multiplet.

The value of the FWHM obtained by the fitting procedure minus the statistical contribution given by Equation 3.8 leads to identify the contribution of the electronic
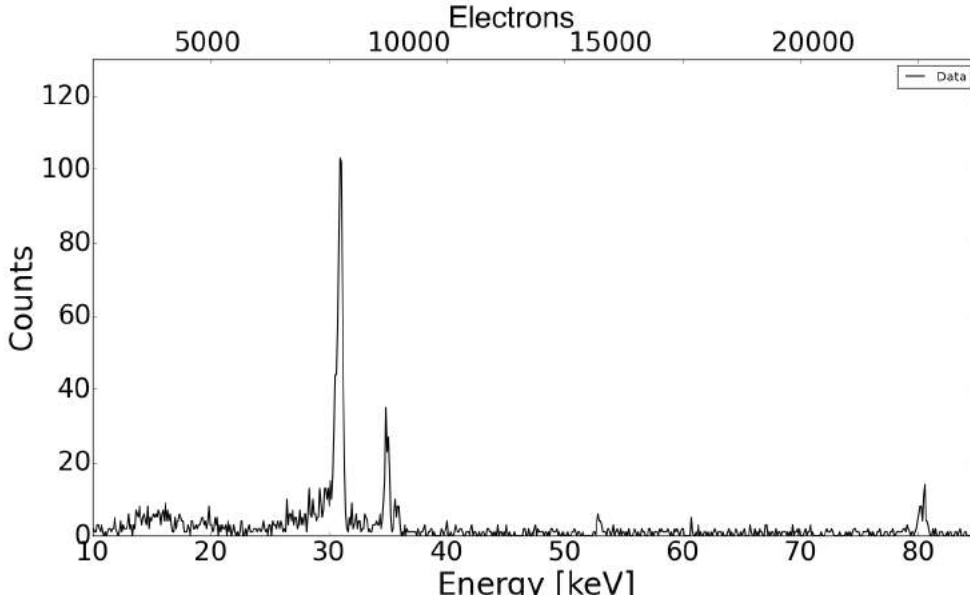
Figure 6.18: *A ^{133}Ba spectrum expressed in both energy and electrons*

noise to the total line width:

$$ENC = \sqrt{FWHM_{measured}^2 - FWHM_{stat}^2}. \tag{6.3}$$

Calculating the ENC in this way, any possible systematic contribution to the noise is automatically included. We developed a *Python* custom software to estimate the ENC value. A fit combining two different Gaussians, in order to model the two blended lines, is performed for channel #1 at 1.65 μs of shaping time (i.e. the optimal shaping time at this temperature) as shown in Figure 6.19.

The fit results in a $FWHM_{measured} = 0.42 \pm 0.02$ keV that is 116 ± 5 e^- $FWHM$. The statistical contribution has been calculated using Equation 3.8, obtaining $FWHM_{stat} = 74.88$ e^- $FWHM$. Thus, using Equation 6.3.3, an ENC of 35 ± 1 e^- r.m.s, that is consistent with other noise measurement performed on other similar devices (ReD-SoX collaboration, priv. comm.), has been estimated.

To estimate the noise performance for different shaping times, the calculation
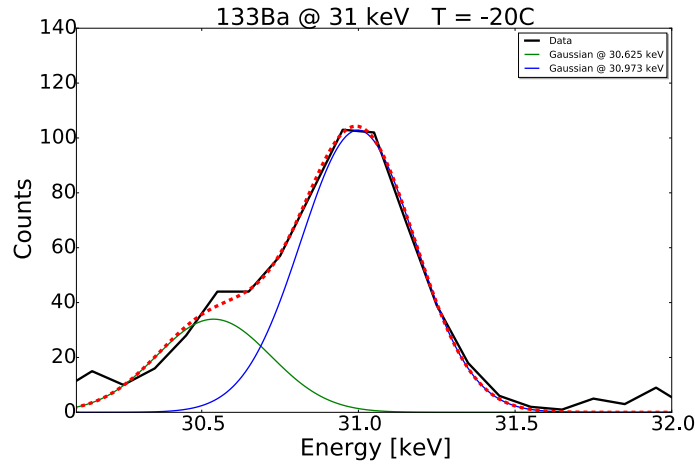
Figure 6.19: *The fit with two Gaussian curves used to model the 30.85 keV blend. The red dotted line is the total fit curve, the green and the blue curves represent the 30.625 keV and 30.973 lines, respectively, which produce the multiplet.*

of the FWHMs is performed, to simplify, using only one Gaussian for the entire multiplet. The main lines of the multiplet are separated by 348 eV (i.e. $\sim$96 e^-). This introduces a systematic broadening of the line but it does not affect the performance comparison between the channels and the shaping time at which the minimum noise value is found.

In Figure 6.20 the noise is reported as a function of the shaping time for the different channels, at a temperature of $-20\,°$C. The best noise performance generally occurs at shaping times longer that 1 μs (where the most common value is 1.65 μs) except for channels #2 and #4.

In particular the trend of #2 is different and shows higher noise. This behavior is similar to the one shown by the other channels at room temperature (Figure 6.11), so it can be interpreted as being due to a higher dark current. The comparison between these curves and those obtained in Figure 6.11 shows how the lower temperature has impacted on the noise performance at long shaping times. In contrast to what was seen at room temperature, the channels maintain almost the same performance even at long shaping times. The higher values at short shaping times is due to series noise (§3.1.4) and an incomplete collection of the charge signal, i.e. the ballistic deficit
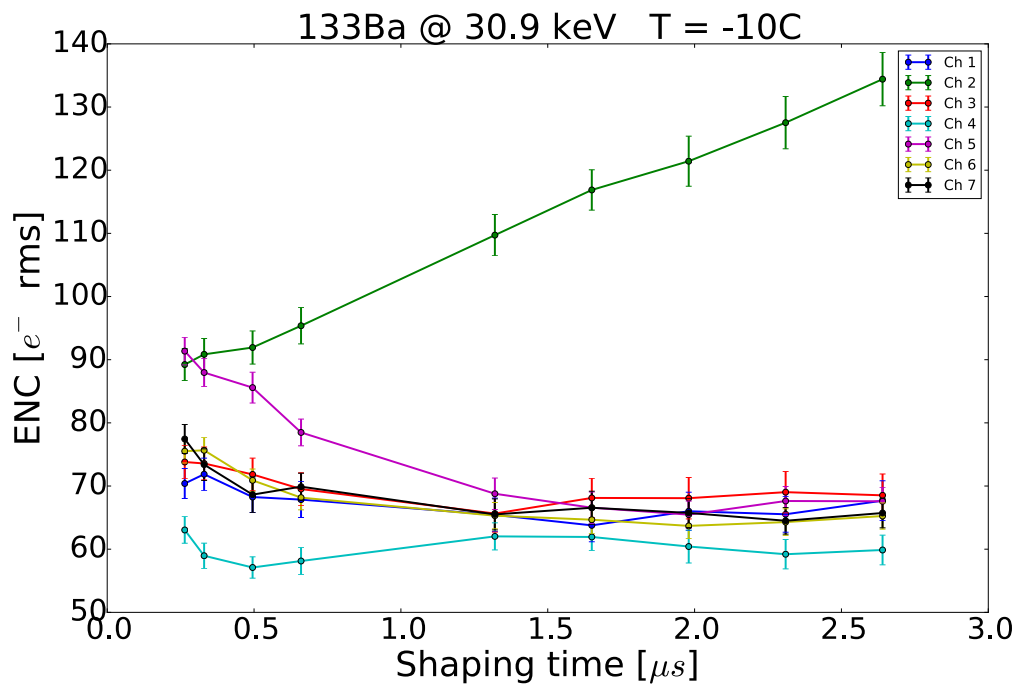
Figure 6.20: *Noise figure for the different channel (see Figure3.9, §3.1.4.). The colors are used to facilitate the immediate identification of the different channels: #1 blue; #2 green; #3 red; #4 light blue; #5 violet, #6 yellow; #7 black.*

described in §3.2.2.

6.3.4 γ-ray characterization

The next step is to characterize the response of the device when the radiation is absorbed by the scintillating crystal and the scintillation light is detected by the SDDs.

The coupling between the SDDs matrix and the scintillator will increase the detectable energy range because, as seen in Figure 6.7, a stand-alone SDD becomes almost transparent to the energies above 30 keV.

To exploit their performance, SDDs are usually coupled with crystals like CsI(Tl) that are characterized by an emission spectrum peaked at $\sim$540 nm. Since the specific need of the project is to realize an efficient coupling between SDD and LaBr$_3$(Ce), the SDDs under investigation were also treated by its manufacturer (FBK) with a surface Anti-Reflective Coating (ARC) in order to increase the detection efficiency to the wavelengths where LaBr$_3$(Ce) emits its scintillation light. To characterize the optical properties of the SDDs used here, the quantum efficiency at wavelengths between 350 and 1100 nm was measured on different devices coming from the same production run (ReDSoX collaboration, Priv. comm.). Figure 6.21 shows the results of the quantum efficiency measurements, comparing the response of SDDs with and without ARC surface treatments. These data can be used to measure the improvements due to the ARC as well as to evaluate the optimal performance of such detectors if a further enhanced QE is achieved.

The ARC has led to an increase in quantum efficiency, in correspondence of the wavelengths to which the LaBr$_3$(Ce) emits its light, close to a factor of 2 with respect to the measured QE without the ARC treatment.

The optical coupling between a scintillator and a Silicon detector is usually achieved by using an optical grease. Reporting as example the properties of the BC-630 Silicone Optical Grease produced by Saint Gobain, this medium features excellent light transmission and low evaporation. It has an index of refraction of 1.465 and a very flat transmission of approximately 95% for wavelengths between 280 nm
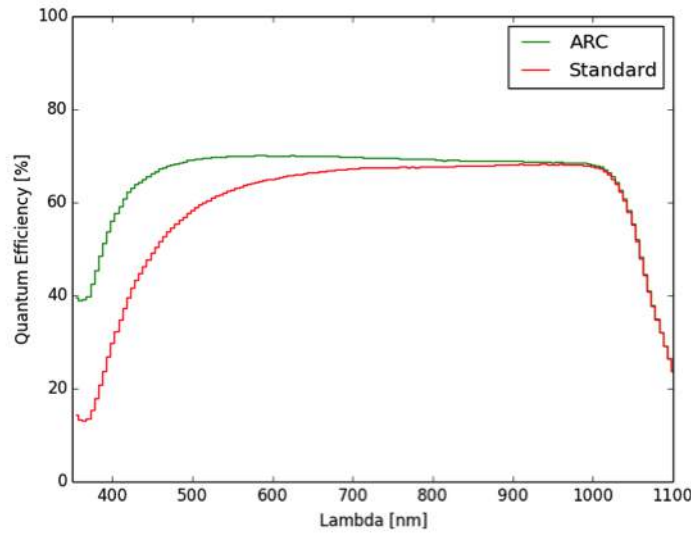
Figure 6.21: *Quantum efficiency results obtained measuring SDDs with ARC surface treatment (green curve) and without (red curve).*

and 700 nm. Furthermore, it allows to minimize the distance between the device and the scintillator, reducing the photon losses. In our case, since the prototype nature of the device under test, the use of a silicone-based solid optical layer of 1 mm thickness was preferred. This layer is designed to be easily removable and in case of disassembling does not leave traces on the optical window.

In order to characterize the energy response of the whole device, radioactive sources with energy lines of a few hundreds of keV were used. For this reason the ^{137}Cs and ^{22}Na radioactive sources have been chosen. The ^{137}Cs presents only one line at 662 keV, the ^{22}Na spectrum is instead characterized by two lines, one at 1274 keV and another, more intense, at 511 keV. This latter line is not directly emitted by the ^{22}Na, but it is due to the positron emitted in the β^- decay that loses its energy in the source material and, once at rest, it annihilates in the presence of an electron producing two photons with an energy of 511 keV, which are emitted in opposite directions for the conservation of momentum.

I developed a custom software in Python able to perform the calibration using the

662 keV line of ^{137}Cs and the 511 keV and 1274 keV lines of ^{22}Na even if their spectra were acquired at different measurement times.This procedure has been performed for each investigated shaping time. In Figure 6.22 the ^{137}Cs and ^{22}Na spectra obtained for channel #1 and for channel #3, which represents the typical case of a peripheral cell, are reported.
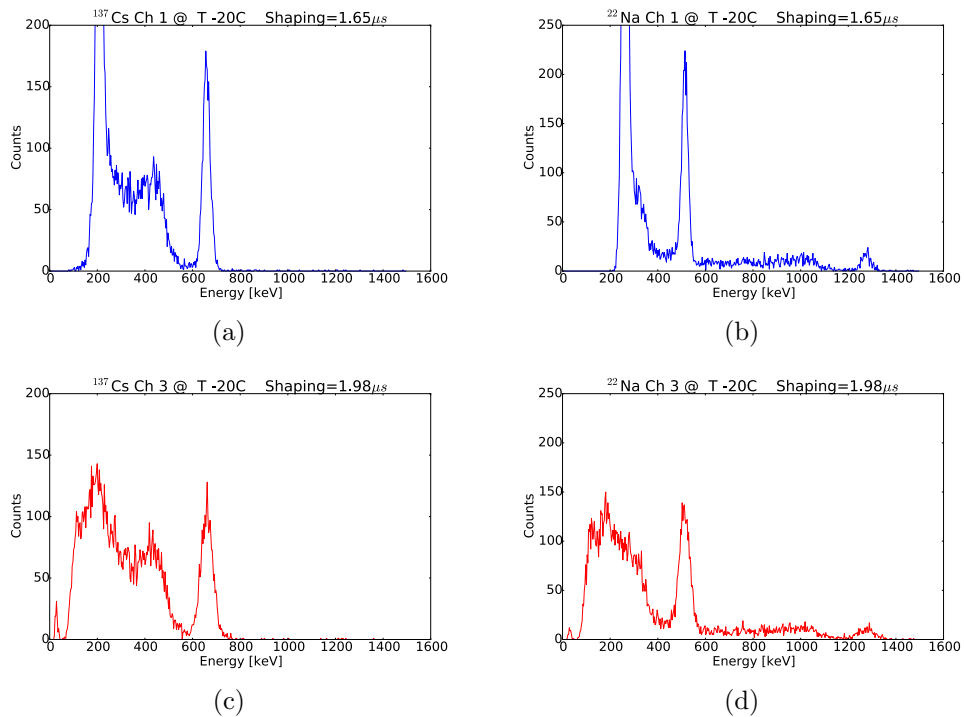
Figure 6.22: *The ^{137}Cs and ^{22}Na spectra obtained for channel #1 (blue line) and for channel #3 (red line).*

The energy resolution has been measured at different shaping times on the 662 keV peak by performing a Gaussian fit and it has been reported as a function of the shaping time in Figure 6.23, where is evident that the behavior of channel #2 is similar to the other channels despite the higher dark current. This is due to the fact that the energy resolution in γ-ray spectroscopy is dominated by the statistical contribution and this is the opposite to what happens for X-ray spectroscopic case in which the electronic noise dominates. Channel #4 for shaping time values shorter

than 1 μs is affected by ballistic deficit. A similar behavior is visible also for other channels but only for shaping times shorter than 0.5 μs. This difference may be due to anomalies in the electric drift field. Such anomalies may alter the drift velocity of the electrons within the SDD slowing the charge collection. This causes the detected signals to reach their maximum amplitude in a longer time.

The best value of the shaping time, in this configuration, is measured at longer shaping times with respect to those measured in the X-ray characterization. When an X-ray photon is directly absorbed in the SDD, its interaction is point-like, releasing an electron cloud. This cloud drifts towards the anode to be collected. As a first approximation, the time interval that elapses between the collection of the first and the last electron of the cloud defines the rise time of the signal. Since the size of the cloud is small (Figure 6.24, left side), the typical rise time for an X-ray event is 100 ns and even if the drift velocity is slow, it does not significantly affect the rise time of the signal. Instead, the case of a scintillation event is different. The optical photons
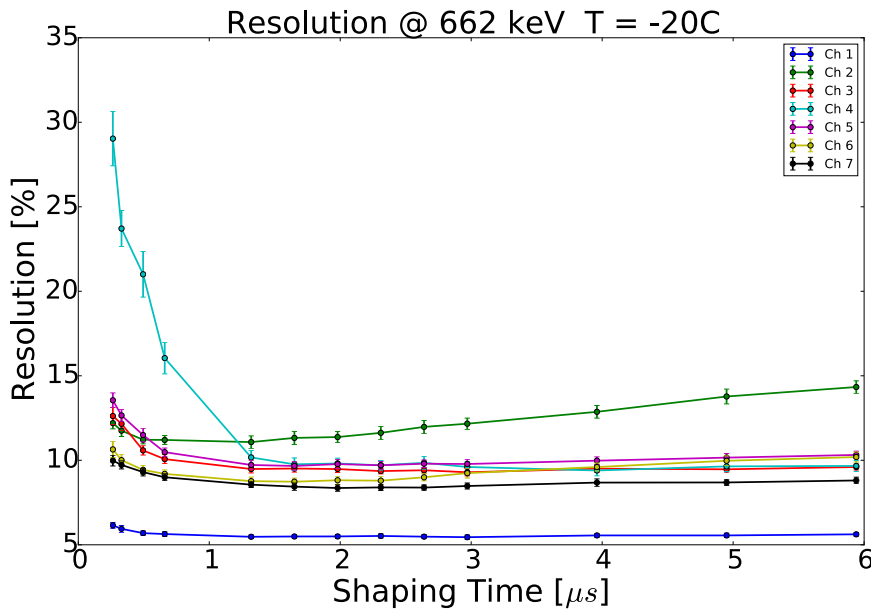
Figure 6.23: *Energy resolution provided by 662 keV line at different shaping times. Different colors represent different channels.*

emitted by the crystal strike the whole sensitive surface of the photodiode, leading to the formation of an extremely diffuse electron cloud (Figure 6.24, right side). The rise time of this signal starts as soon as the electron nearest to the anode is collected and is completed, reaching its maximum amplitude, as soon as the most distant one is collected. Therefore a slower drift velocity influences the arrival time of the farthest electron. The drift velocity is proportional to the SDD biasing voltage, but the electron collecting time, in some applications, can be influenced also by the decay time of the scintillator. Therefore, the higher the voltage, the faster the collection
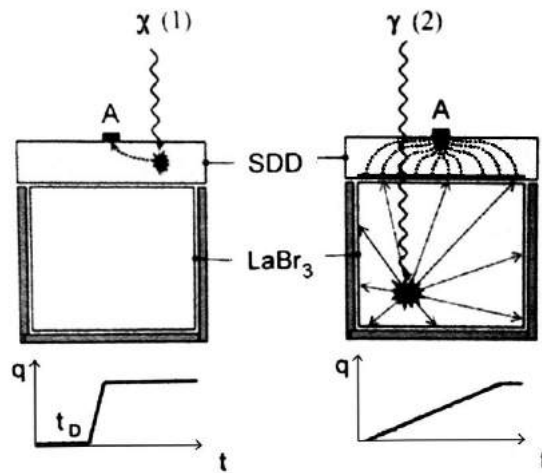
Figure 6.24: *The interaction of a X-ray in the SDD that results in the generation of a little electron cloud and the typical signal characterized by a fast rise time (Right panel). The interaction of a γ-ray in the crystal volume that results in the isotropic production of optical photons and the signal characterized by the typical slow rise time (Left panel).*

time. The decay time governs the time scale at which the optical photons are emitted by the crystal. A scintillator with a rapid decay time as the $LaBr_3(Ce)$ makes the photons arrive almost instantly on the SDD surface and the signal rise time, in this case, is given by the time taken for the most distant cloud to be harvested. A slow decay constant, as in the case of CsI, leads to long emission time, therefore an almost continuous stimulation of the SDD volume takes place until the emission process is completed. The signal results to be characterized by a long rise time. In the last case

a longer shaping time will be needed to fully integrate the signal without suffering of ballistic deficit.

As anticipated during the X-ray characterization, the calibration in electrons is also useful when the photons emitted by the crystal are detected by the SDD. When a γ-ray photon of energy E interacts with the crystal, the crystal emits isotropically, within its volume, a number of optical photons given by $N_{\text{ph}} = E \cdot L_\lambda$ where L_λ is the light yield of the crystal (§5.3). Considering the crystal self-absorption and the photon losses due to the escaping from the crystal surface, usually only one half of the emitted light arrives on the contact surface between the crystal and the SDDs. A fraction of them, identified by the quantum efficiency of the SDDs, interacting within the SDD sensitive volume, results in the production of electrons in a 1:1 proportion. Therefore the number of electrons detected after a γ-ray interaction within the scintillator gives us an indicator of the efficiency of the detector optical coupling and of the light collection.

The previously determined calibration coefficients are used to calibrate the γ-ray spectra that are thus reported in Figure 6.25 and Figure 6.26.

The amplitude of the signal detected by the interaction of the photons varies from cell to cell, depending on the crystal coverage. Channel #1, that is the only fully covered, shows the highest detected amplitude. The other channels, that are covered only for the $\sim$55% of their surface, detect almost half of the signal. The relative differences in resolution and spectral shape among the peripheral channels, may be due to a non symmetrical placing of the scintillator over the SDD matrix.
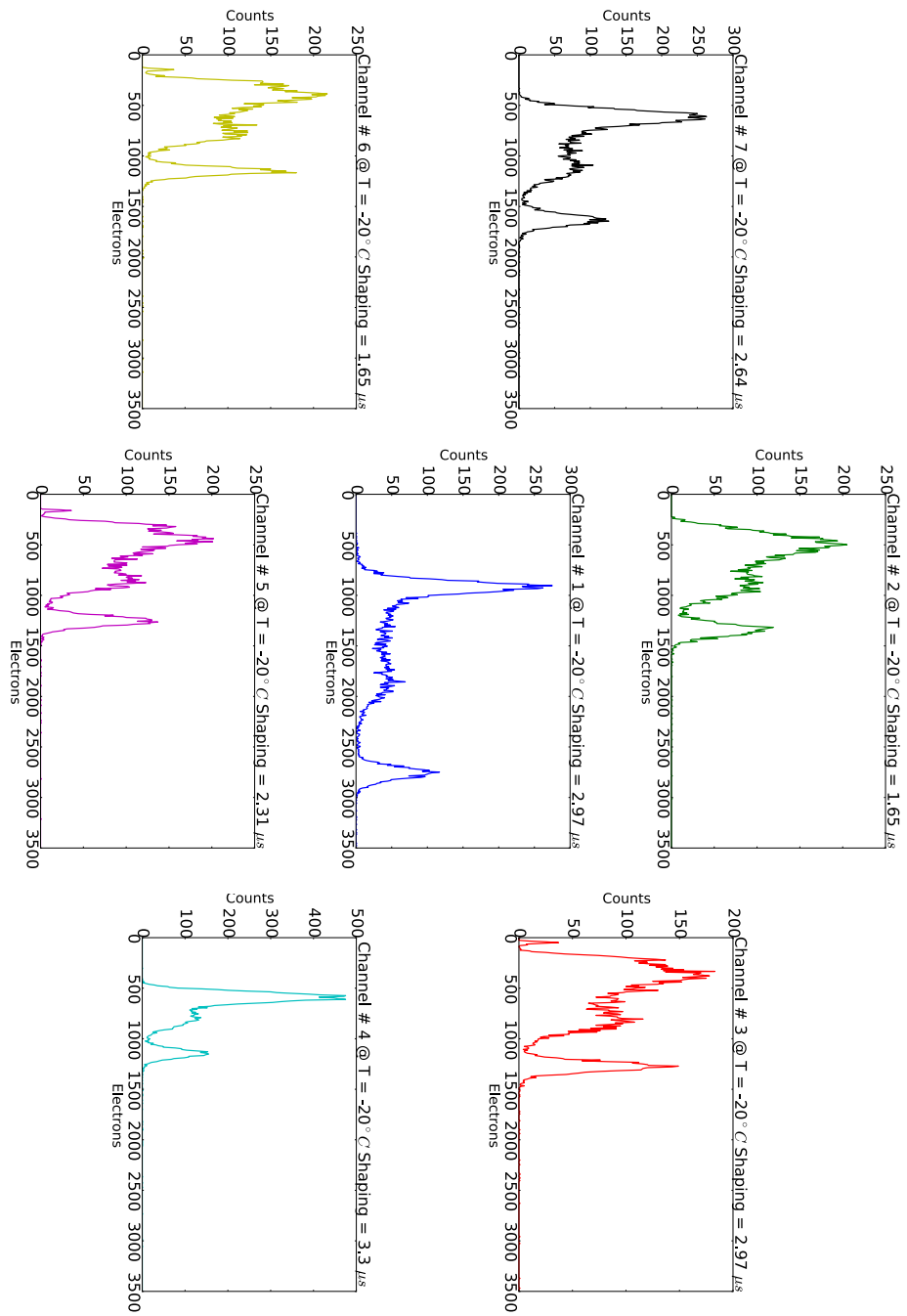
Figure 6.25: *The ^{137}Cs spectrum obtained from each SDD array cell.*
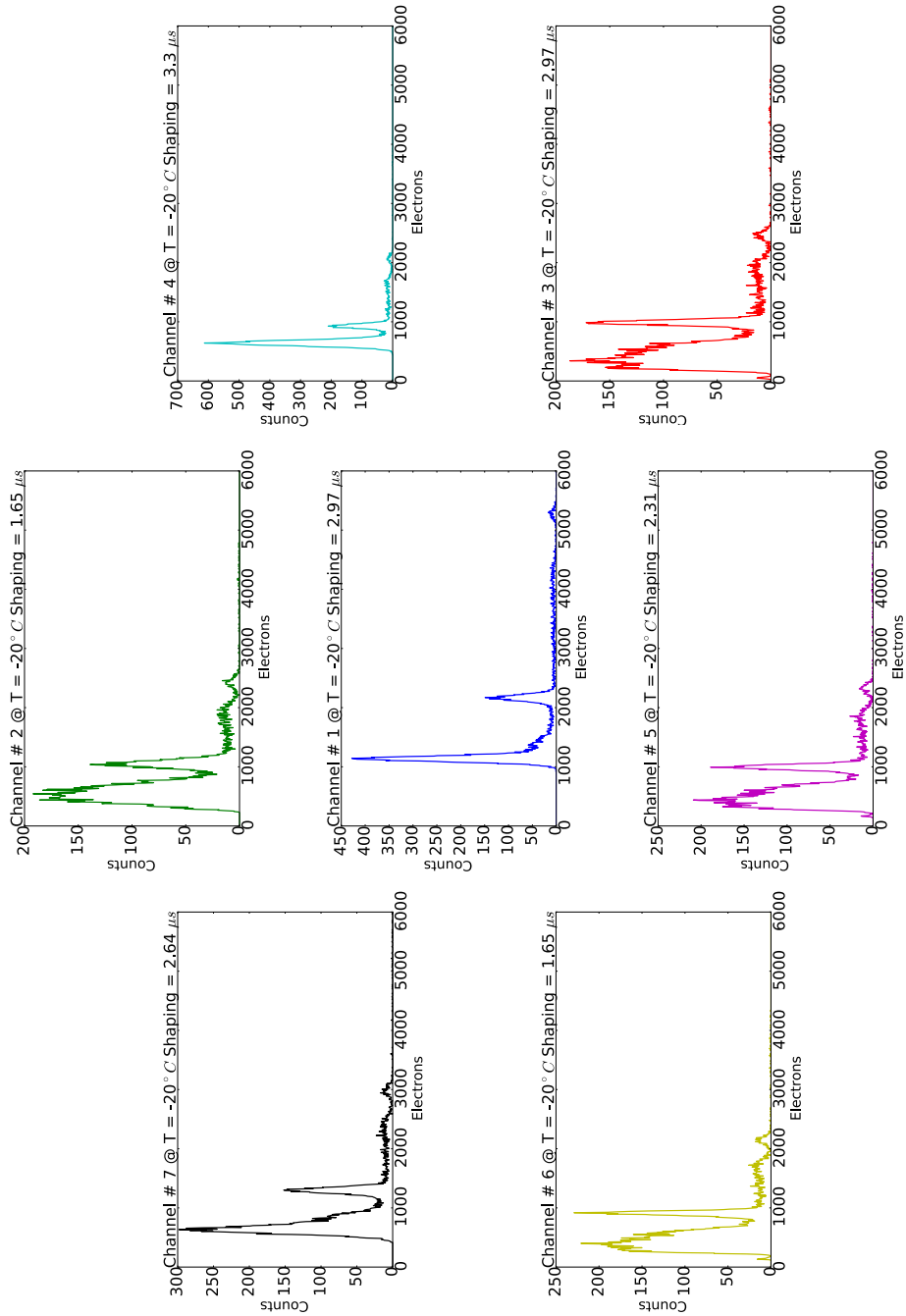
Figure 6.26: *The ^{22}Na spectrum obtained from each SDD array cell.*

6.3.5 Light output

One of the most important parameters that characterize the quality of detectors based on scintillators is the *light output*. This quantity refers to the amount of scintillation light detected by the photodetector per unit of absorbed energy and is expressed in e$^-$/keV. In order to derive the light output, a Gaussian fit is performed using the 511 keV, 662 keV and 1274 keV energy peaks of ^{137}Cs and ^{22}Na when the spectrum is electron-calibrated. Therefore the total amount of electrons is divided by the corresponding energy determining the light output for each cell, reported in Table 6.4.

| | **Light output [e$^-$/keV]** | | |
#	511 keV	662 keV	1274 keV
1	4.24 ± 0.03	4.16 ± 0.03	4.14 ± 0.05
2	2.05 ± 0.05	2.02 ± 0.03	1.90 ± 0.04
3	1.93 ± 0.03	1.92 ± 0.02	1.93 ± 0.04
4	1.81 ± 0.02	1.73 ± 0.02	1.82 ± 0.04
5	1.95 ± 0.02	1.89 ± 0.02	1.82 ± 0.04
6	1.78 ± 0.02	1.74 ± 0.01	1.68 ± 0.03
7	2.54 ± 0.03	2.47 ± 0.02	2.34 ± 0.05
Tot	16.3 ± 0.2	15.9 ± 0.1	15.4 ± 0.3

Table 6.4: *Light output for each channel obtained using the 511 keV, 662 keV and 1274 keV peaks. The last row reports the total light output obtained by summing the contribution of each channel.*

Since each cell detects a portion of the scintillation light (generated isotropically within the crystal by a single incoming γ-ray photon) the contribution coming from all the cells have to be integrated to estimate the global performances of the system. The last row in Table 6.4 shows that the global light output is $\lambda_{\text{tot}} \sim 16$ e$^-$/keV and that the variation between the value measured at different γ-ray lines is consistent within a few percent, as expected.

6.3.6 The reconstructed signal

Up to now I have presented the analysis focused on the behavior of each cell separately, but the device has to operate as a single detector. The outputs of each cell, i.e. both signal and electronic noise, have to be summed in order to reconstruct the total response of the device. This process is necessary when a segmented detector, as the SDDs matrix, is used to read the scintillation light from a single crystal. The summation process leads to an improvement of the energy resolution until R_{Stat} is the dominant contribution over the electronic noise R_{El}.

In this type of detectors, each single cell covers a fraction f of the crystal contact surface A_{Tot}. Assuming that it is possible to produce cells that perfectly cover the whole surface A_{Tot}, their maximum number is $N_{\text{Max}} = \frac{A_{\text{Tot}}}{A_{\text{Cell}}}$. If A_{Tot} is fixed, then N_{Max} depends only on A_{Cell}. L_{γ} is the light yield of the crystal, i.e. the number of optical photons produced inside the crystal per keV deposited. Considering the quantum efficiency of the SDD and the light collection, λ_{Tot} is the total amount of detected photons that are distributed over A_{Tot}. Thus the single cell will collect a fraction f of λ_{Tot}, i.e. $\lambda_{\text{Cell}} = f\lambda_{\text{Tot}} = \lambda_{\text{Tot}}\frac{A_{\text{Cell}}}{A_{\text{Tot}}}$. Summing all the cell contributions, the total number of collected photons is $N_{\text{Ph}} = N_{\text{Cell}}\lambda_{\text{Cell}}E_{\lambda} = N_{\text{Cell}}\lambda_{\text{Tot}}\frac{A_{\text{Cell}}}{A_{\text{Tot}}}E_{\lambda}$, where E_{λ} is the energy of the initial λ photon.

Assuming that the electronic noise is the same for every cell, regardless of its area A_{Cell}[5], the total energy resolution is

$$R_{\text{Tot}} = \sqrt{\frac{1}{N_{\text{Ph}}} + N_{\text{Cell}}R_{\text{El}}^2} = \sqrt{\frac{A_{\text{Tot}}}{N_{\text{Cell}}\lambda_{\text{Tot}}A_{\text{Cell}}E_{\lambda}} + N_{\text{Cell}}R_{\text{El}}^2} \qquad (6.4)$$

where the possible presence of a systematic contribution is neglected. Assuming a crystal with A_{Tot}=210 mm^2, an ENC of 10 e^- *r.m.s.* for each channel and a $\lambda_{\text{Tot}} = 5$ e^-/keV, some curves describing the energy resolution for various values of N_{Cell} are reported in Figure 6.27.

The minimum value of the energy resolution splits the plot in two regions: for

---

[5]This assumption is unrealistic since the dark current is proportional to the surface of the detector. However, it is useful in our case to show a simplified model that aims to indicates the role of the statistical and the noise contributions.
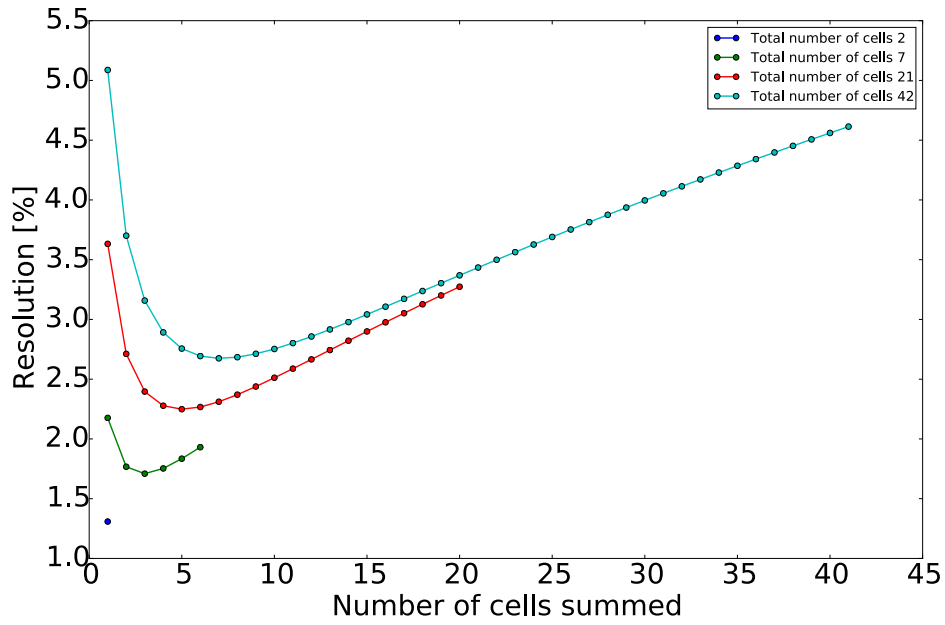
Figure 6.27: *Improvement in the measured energy resolution using the 662 keV line when progressively summing each channel. The crystal surface $A_{\mathrm{Tot}}=210mm^2$ is fixed. Different colors refer to systems with different number of cells. Their area is related to the number of cell $A_{\mathrm{Cell}} = \frac{A_{\mathrm{Tot}}}{N_{\mathrm{Cell}}}$. For example, the red line represents a system with 21 cell of $A_{\mathrm{Cell}}=10$ mm^2 each. Note that in these examples any systematic contribution from the crystal non-linearities is neglected, and we further assume an electronic noise independent on the cell area A_{Cell}.*

$N < N_{\text{Cell}}^{(\text{Min})}$ the resolution is dominated by the statistical contribution because an increase in the number of cells leads to a higher light collection and therefore an improvement of the performance; for $N > N_{\text{Cell}}^{(\text{Min})}$ the increasing contribution of electronic noise exceeds the benefits due to the larger light collection, leading to a worsening of the performance. It is evident how the use of a single cell is, in principle, preferable with respect to a multi-cell configuration since it allows to achieve a higher total energy resolution. In a multi-cell system, the overall electronic noise results to be much higher since it is due to the quadrature sum of the single noise contributions. However, the operation of a the single cell system can be compromised by an occurring malfunction, while a multi-cell system, thanks to its redundancy, can continue to operate even if a defective cell of the system is turned off.

The above mentioned procedure has been performed on each cell of the SDD matrix. To reconstruct the final spectrum, the spectra electron-calibrated, in their best operational configuration, are summed. Every time a channel is added to the partial spectrum, it is calibrated in energy and the energy resolution is calculated using the 662 keV line. Figure 6.28 shows the improvement in energy resolution for different number of summed channels. Once the 7 channels are added together, a total energy resolution of 3.45% is obtained.

From this energy resolution trend, we can conclude that the response of the prototype under study is dominated by the statistical contribution. Figure 6.29 compares the ^{137}Cs spectrum obtained by the central cell to the total spectrum obtained summing the contribution of each recalibrated channel, showing the improvement in resolution.

To estimate the final light output of the device, the spectra calibrated in electron are summed together. On the resulting spectrum, the light output is estimated using the 662 keV line, and then a value of 16.45 e/keV is obtained. This value is comparable with the one achieved by the simple sum of the single light outputs measured in each cell.
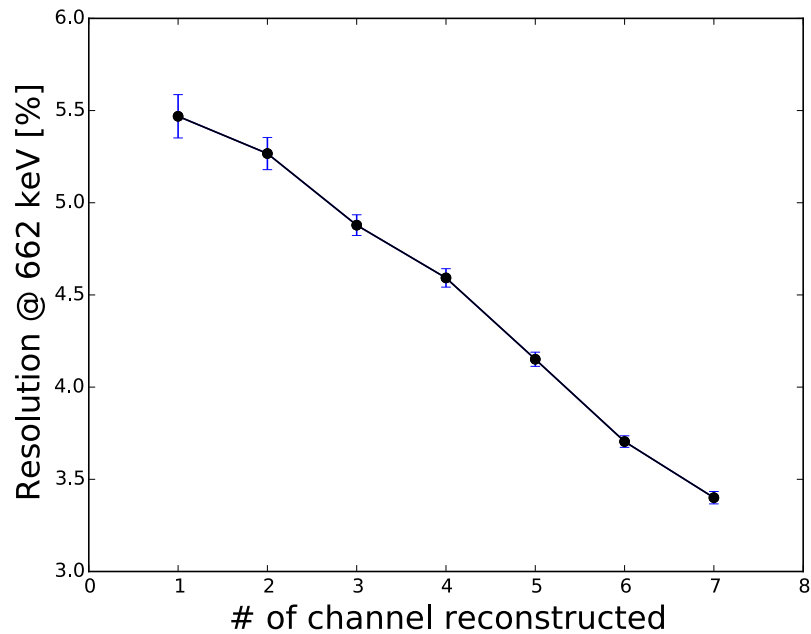
Figure 6.28: *Improvement in energy resolution measured using the 662 keV line when progressively summing each channel.*
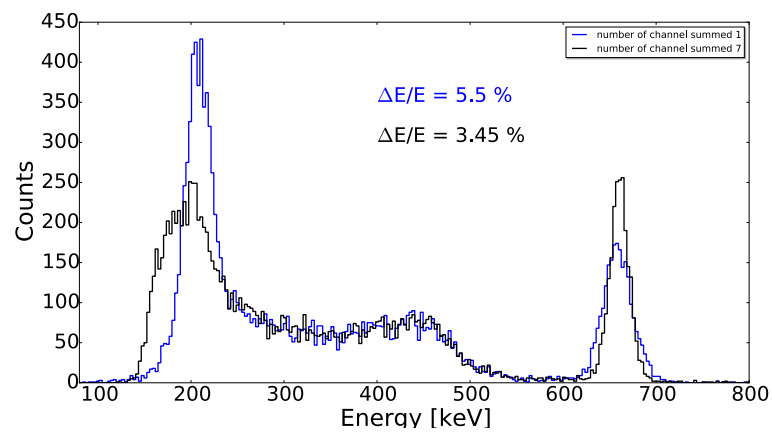
Figure 6.29: *The comparison of the spectrum obtained from a single cell (#1, blue curve) and the reconstructed spectrum obtained summing all channels (black curve). We observe the 662 keV line, that is the meter of this comparison, the Compton continuum and the noise tail.*

6.3.7 Discussion of the results

In literature a light output close to $\sim$30 e$^-$/keV and a resolution of 2.8% is reported (Fiorini et al., 2013) when coupling a SDD with a LaBr$_3$(Ce) crystal. The lower values measured here can be related to the quantum efficiency of the SDD array used, especially at wavelengths below 450 nm where the LaBr$_3$(Ce) scintillation light spectrum peaks. In Figure 6.30 the LaBr$_3$(Ce) emission spectrum is compared with the measured QE of the photodetector. In order to estimate the fraction of the scintillation light detected by the SDD, we have normalized the area under the scintillation emission spectrum obtained from the Saints Gobain datasheets and then we performed the convolution of this area with the measured QE data. In the case of LaBr$_3$(Ce), only 44% of the incoming light is detected by the SDD. If our choice had fallen on CsI(Tl), corresponding to higher QE, the detected fraction would be 71%. Similarly, it is possible to estimate the fraction attainable if a device with a QE similar to the one used by Fiorini et al. (2013) were available (red dashed line in Figure 6.30). In the case of enhanced QE, the fraction of LaBr$_3$(Ce) scintillating
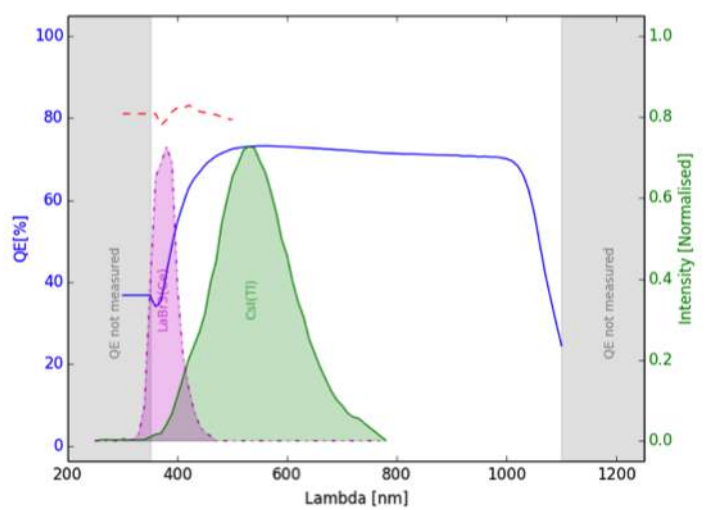
Figure 6.30: *Comparison between the measured quantum efficiency (blue) and scintillation light spectrum of CsI(Tl) (green),* LaBr$_3$(Ce) *(violet) and an example of enhanced QE (red dashed) (Fiorini et al., 2013). Their intensity are reported normalized to the maximum value of the measured QE.*

light detected can be increased up to ~81%. This means that if we measure a light output of ~16 e^-/keV when only 44% of the scintillating light can be seen by the SDD, then for an enhanced QE a light output of about 29.5 e^-/keV can be obtained.

We have measured a total resolution of $R_{\text{Measured}} = 3.46\%$ on the 662 keV line. Recalling Equation (3.10) and expressing the energy resolution as

$$R_{tot}^2 = R_{\text{Stat}}^2 + R_{\text{El}}^2 + R_{\text{Sys}}^2 \tag{6.5}$$

to evaluate the presence of a systematic contribution to the total energy resolution, we have to compare the R_{Measured} to the expected resolution in absence of a systematic contribution;

$$R_{\text{no-sys}}^2 = R_{\text{Stat}}^2 + R_{\text{El}}^2. \tag{6.6}$$

We can analytically estimate the statistical and the electronic noise contributions. $R_{\text{Stat}} = \frac{1}{\sqrt{N_{\text{ph}}}}$, where N_{ph} is the number of total electron detected by the photodetector, i.e. $N_{\text{ph}} = \lambda_{\text{tot}} E_\gamma = 10889 \ e^-$ at 662 keV. R_{el} is the total electronic noise, where the single cell contribution is added in quadrature, thus $R_{\text{el}} = \frac{2.35 \cdot \sqrt{7} ENC}{N_{\text{ph}}}$ = assuming the same ENC value for each channel, i.e. 35 e^- rms measured in §6.3. Therefore we can estimate $R_{\text{no-sys}} = 3\%$. The difference with respect to the measured value of 3.45% shows the presence of a systematic contribution to the total resolution, that can be estimated using

$$R_{\text{sys}} = \sqrt{R_{\text{Measured}}^2 - R_{\text{no-sys}}^2}. \tag{6.7}$$

resulting in $R_{\text{sys}} = 1.7\%$. This value is comparable with the literature (Moses, 2002) and can be attributed to the intrinsic non-linearities of the $LaBr_3(Ce)$ crystal. This result shows that the prototype and the spectroscopic chain under test are not affected by any type of additional systematic contribution apart from the intrinsic scintillator contribution.

We also can estimate the energy resolution (Figure 6.31), including also the intrinsic contribution, as a function of both electronic noise and light output according
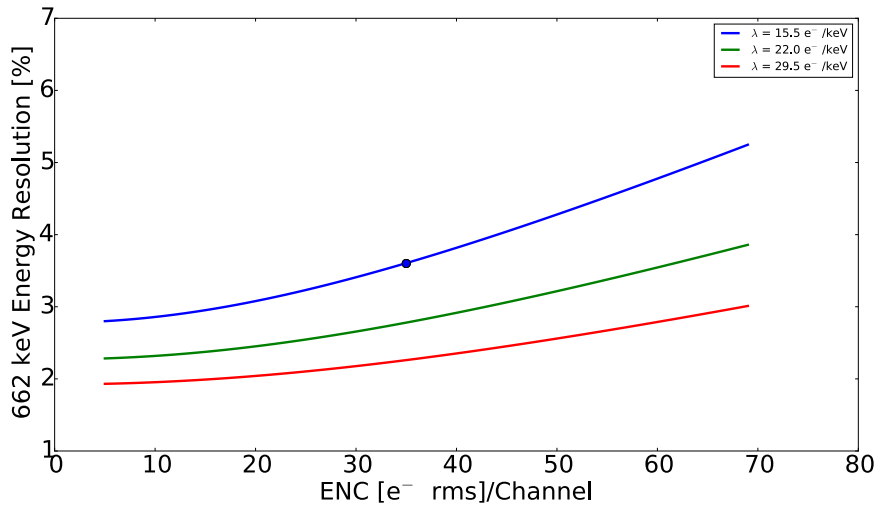
Figure 6.31: *Resolution at the 662 keV line estimated at adopting few values of ENC and QE. The blue line represents the actual QE and the marker on it is the value measured in this thesis. The red line represents the value of the enhanced QE which will result in collecting of $\sim 81\%$ of $LaBr_3(Ce)$ scintillating light. The green line represents an intermediate value of QE.*

to different QEs, from the present one to some possible enhanced QE. The blue curve, which represents the present QE of the prototype tested, shows that even stressing the electronic noise requirements, using expensive high performance electronics, only a little improvement in the energy resolution can be achieved, reaching 2.85% at 662 keV. It is evident that enhancing the QE leads to a larger improvement. Indeed, the use of extremely performing electronics (i.e. less than 10 e^- r.m.s) with the present QE results in about the same performance that would be attainable by doubling the QE and relaxing the electronic noise requirements by more then a factor of 10 (5 e^-rms vs. 70 e^-rms). The natural conclusion is that efforts must be primarily focused in achieving an enhanced QE. It is clear that the use of high-performing electronics with an enhanced QE would lead to obtain above state of the art spectroscopic performance, reaching 1.95% resolution on the 662 keV line, close to the intrinsic systematic limit.

6.4 Timing performance

In a large number of applications, information on the precise arrival time of photons in the detector is of particular interest. The accuracy by which timing can be performed depends both on the properties of the specific detector and on the type of electronics used to process the signal. Sources of timing inaccuracy are divided into two categories: those that apply when the input pulse amplitude is constant are usually called sources of *time jitter*, whereas the effects that derive primarily from the variable amplitudes of input pulses are defined as *amplitude walk*. The former are always present since they are related to signal-to-noise ratio (Figure 6.32). The latter, instead, can be removed if the method used to determine the timing information is amplitude independent.

(a) (b)
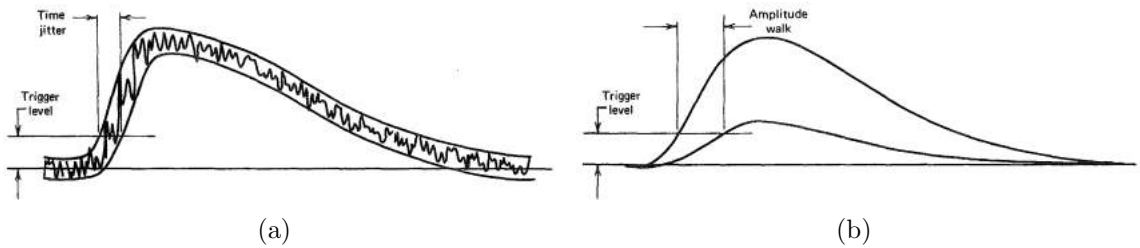
Figure 6.32: *(a) Example of time jitter when the threshold used to identify the starting point of the signal rise is set to a constant value. (b) Example of amplitude walk with the same pick-off method. Figure from Knoll (2010)*

An important source of time jitter are the random fluctuations in the signal pulse size and shape. These fluctuations can arise from the electronic noise and from variations of the rise time.

Since the signal output amplitude from the detector prototype under test is proportional to the deposited energy, we have to adopt a pick-off method that allows us to avoid the uncertainty that arises from the amplitude walk. A *constant fraction discriminator* is used to identify when a signal has reached a constant fraction of its peak amplitude. Referring to fractions of the peak amplitude, we can define the rise time in a unique way regardless the absolute value of the signal, avoiding the amplitude walk.

The algorithm, schematized in Figure 6.33 that brings as an example the output from the preamplifier (Figure 6.33a), involves multiplying the signal by a factor f that corresponds to the desired fraction of full amplitude. The input waveform is also inverted and delayed for a time longer than the rise time to give the waveform shown in Figure 6.33(c). The sum of the waveforms in Figure 6.33(b) and Figure 6.33(c) is then taken, producing the pulse sketched in Figure 6.33(d). The time at which the pulse crosses the zero axis (i.e. the *zero cross* time) is independent of the pulse amplitude and corresponds to the time when the pulse reaches a fraction f of its final amplitude.
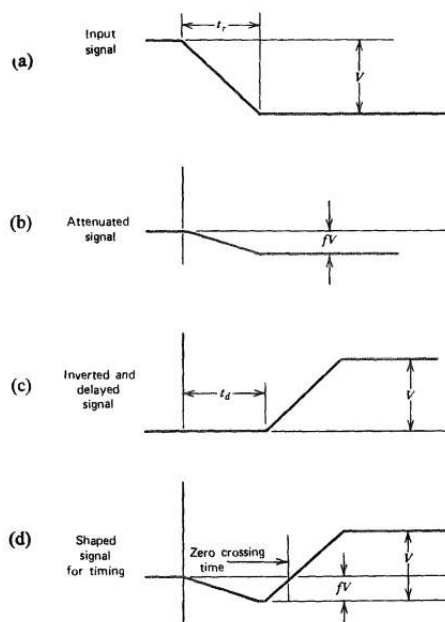
Figure 6.33: *Waveforms in the constant fraction time pick-off method. Figure from Knoll (2010).*

I have implemented this method by means of a Python program, then we have applied it on previously acquired preamplifier digitized waveforms (thus avoiding the need to repeat a measurement with the appropriate setup as would have happened in the analog case). I chose the ^{241}Am signals to study the X-ray signal time properties, since they allow us to investigate a wide amplitude range. For the γ-ray events, the

choice has fallen on the 511 keV line of ^{22}Na and on the 662 keV line of ^{137}Cs, rejecting the 1274 keV line because of its low statistics. I chose the signal recorded by the central and a peripheral cell, since they present different amplitudes at a given energy. A linear fit was used to determine the zero cross and the rise time of the signal was defined as the time elapsed between the 30% and the 80% of the maximum signal amplitude, since these thresholds identify the signal portions that are easier to locate and are less affected by the presence of noise. In Figure 6.34 the rise time distributions at different signal amplitudes are reported.
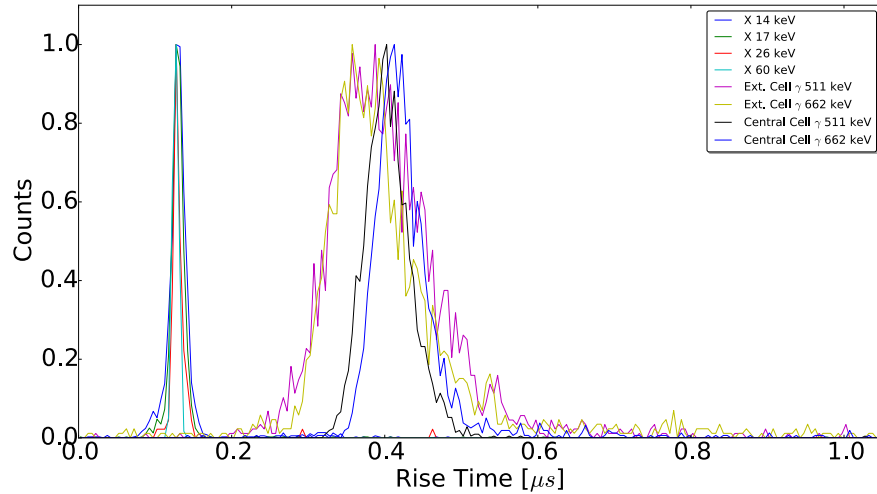
Figure 6.34: *Distribution of the rise time for different amplitude pulses normalized to unity amplitude in order to allow a better comparison of the centroids.*

One can observe that the X-ray events show a constant rise time of ∼150 ns at the various signal amplitudes. γ-ray events, instead, show a different behavior. A slight dependence on the signal amplitude is evident as the Gaussian centroid is observed at longer rise times at different amplitudes, i.e 380 ns and 420 ns for the 662 keV signal detected by a peripheral and the central cell respectively, in addition to showing an asymmetry in the rise time distribution that is not observed in the case of X-ray events.

A Gaussian fit has been performed on each distribution, and in Figure 6.34(a)

the FWHMs obtained, i.e. the jitters, are reported for various signal amplitudes.
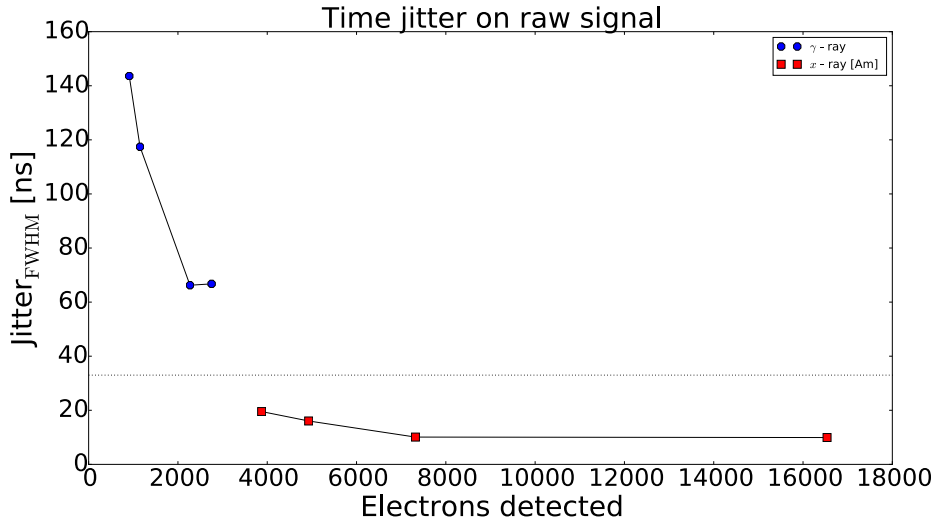
Figure 6.35: *The jitter at various amplitudes of the signal. The red squares represent the X-ray events of* ^{241}Am, *the blue circles represent the γ-ray events at energies of 511 keV* ^{22}Na *line and 662 keV* ^{137}Cs *line. The first two points are detected in a peripheral cell and the last two, with almost twice amplitude, are detected in the central cell. The dotted line shows the sampling rate of the digitizer used.*

The dotted line represents the sampling rate at which the waveform are digitized, i.e. a sample every 33 ns. It is possible to reach time resolutions below the instrument's accuracy threshold because, since the zero cross is determined through a linear fit, its uncertainty is no longer associated to the sampling rate. The red points represent the X-ray events and the blue represent the γ-ray ones.

The X-ray events, that are characterized by the same rise time, have a higher accuracy when a larger amplitude is measured. The best accuracy is measured at 16538 e$^-$ and results in $\sim$10 ns. The γ-ray event accuracy shows instead a strong dependence on the amplitude. This may be due to both the worse signal-to-noise ratio and the different shape of the signal pulse.

To estimate the contribution to the jitter given by the signal-to-noise ratio, we repeated the same analysis on the trapezoidally shaped signals. We choose a shaping time of 0.65 μs and 2 μs for X-ray and γ-ray respectively, which are the ones at
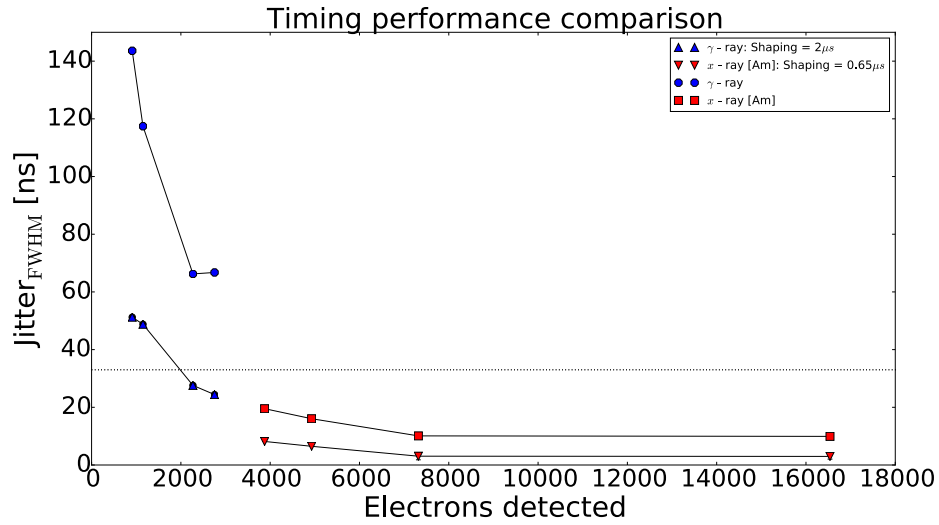
Figure 6.36: *Comparison of the timing results obtained for raw and shaped signal. The improvement in timing performance due to the shaping is, on average, about 33% with respect to the raw signals.*

which also the best spectroscopic performance is achieved. In Figure 6.36 a comparison between the raw and shaped signals is reported. The shaping results provide an average improvement of timing performance of about 33% in both the X-rays and γ-rays with respect to the raw signals. This improvement may be attributed to the better signal-to-noise ratio that is can be obtained with shaped signals. The asymptotic trend at $\sim$3 ns, that is found for the X-rays data at the highest amplitudes, shows the limit in the timing accuracy that can be achieved with this prototype.

Signals with larger amplitude provide better timing performance. Improving the QE will lead to produce signals, due to γ-ray event, with a larger amplitude. Therefore, the use of an enhanced QE increases both the spectroscopic performance and the timing accuracy. Another method to achieve high timing performance for γ-ray signal is to modify their shape in order to be more similar to the X-ray signal shape. This can be obtained if a higher drift field is used. Thus, for a given Si bulk resistivity, the only way is to modify the internal voltage divider of the SDD that sets the voltage of each cathode.

Chapter 7

Conclusions

For centuries astronomical studies have been limited only to observations in the visible band. Only in the last decades, thanks mainly to the technological developments and the possibility to send instruments outside the Earth atmosphere, the observation of the sky has been extended to all the frequencies of the electromagnetic spectrum. The study of X-rays and γ-rays revealed a violent and variable Universe whose phenomena are not yet completely understood. Currently, there is a huge scientific interest towards high-energy astronomy, as evidenced by various space missions (HERMES, THESEUS and e-Astrogam) that have been proposed in the context of ESA Cosmic Vision program.

The need to build instruments as much compact and lightweight as possible with high performance is a key aspect in designing new space missions. Given the requirements mentioned above, it is therefore necessary to design new devices that can maximize the spectroscopic and timing performance. In this thesis we have carried out the study of a γ-ray spectrometer based on the coupling of a scintillator crystal, $LaBr_3(Ce)$, with a solid state photodetector, the Silicon Drift Detector (SDD).

SDDs are solid state devices mainly designed for X-ray applications. However, they can be used to obtain γ-ray detectors with high-spectroscopic performance when they are optically coupled with adequate scintillator materials. The peculiar design of the SDDs allows to disentangle the anode capacitance from the area of the device, reducing the electronic noise at short shaping times (§3.1.4), and to obtain many

different SDD layouts. SDDs have been successfully coupled with inorganic crystals such as CsI(Tl), whose emission spectrum covers the same wavelength at which the SDD quantum efficiency peaks.

LaBr$_3$(Ce) is a relatively recently developed scintillator crystal. The main desirable properties of a scintillator crystal used for spectroscopy applications are the light yield, i.e. the number of optical photons produced per unit of energy within the crystal that should be as high as possible, and the intrinsic contribution to the energy resolution (that takes into account the fluctuations in the number of optical photons produced) that should be as low as possible. The short decay time (16 ns), along with a high light yield (63 ph/keV) and a low intrinsic contribution to the resolution (Figure 7.1), make LaBr$_3$(Ce) one of the most promising scintillator crystals for applications in which energy resolution and timing are of primary importance. Therefore, it qualifies as an optimal candidate to design a state of the art performance γ-ray detector. However, producing an efficient γ-ray detector by coupling LaBr$_3$(Ce) with SDD is not a trivial task.

In this thesis we have extensively tested a γ-ray detector prototype composed by a matrix of 7 hexagonal Silicon Drift Detectors optically coupled with a commercial cylindrically shaped LaBr$_3$(Ce) with a 0.5" diameter and 0.5" height.

For the characterization of time properties, we have observed that the accuracy on the measurement of the arrival time of an event results to be dependent on the amplitude and shape of the signal. The maximum accuracy is therefore obtained when the signals are trapezoidally shaped, since the signal-to-noise ratio is improved. We measured a jitter, i.e. the width of the signal rise time distribution, of 3 ns for the X-ray events generated by the interaction in the SDD of the ^{241}Am 59.54 keV line. In the case of γ-ray scintillation events, the maximum accuracy achieved is of 24 ns, with a mean accuracy of 37.5 ns.

We have quantified the fluctuations in the signal baseline due to the electronic noise, expressed in terms of Equivalent Noise Charge (ENC), of $\sim$35 e^- $r.m.s$ for each SDD cell, comparable with values measured in other ReDSoX SDDs coupled with similar readout electronics. The energetic resolution for γ-rays has been estimated using the 662 keV ^{137}Cs line. A value of $\sim$5.5% has been measured for the central

cell, i.e. the only one totally covered by the crystal, and $\sim 10\%$ for the peripheral cells (average value), covered only for a fraction of $\sim 55\%$. A light output of 4.25 $e^-/$keV has been obtained for the central cell that is almost twice the mean value for peripheral cells of 1.9 $e^-/$keV (average value).

Collecting the information obtained from all cells in their best operational conditions, an energy resolution of 3.45% and a light output of 16.5 $e^-/$keV are achieved. The presence of a systematic contribution of the crystal to the total energy resolution has been estimated comparing the measured resolution with the theoretically expected value in absence of any systematics. We have estimated a systematic contribution to the energy resolution of 1.9%, comparable with the values obtained in literature (Moses, 2002) and reported in Figure 7.1.
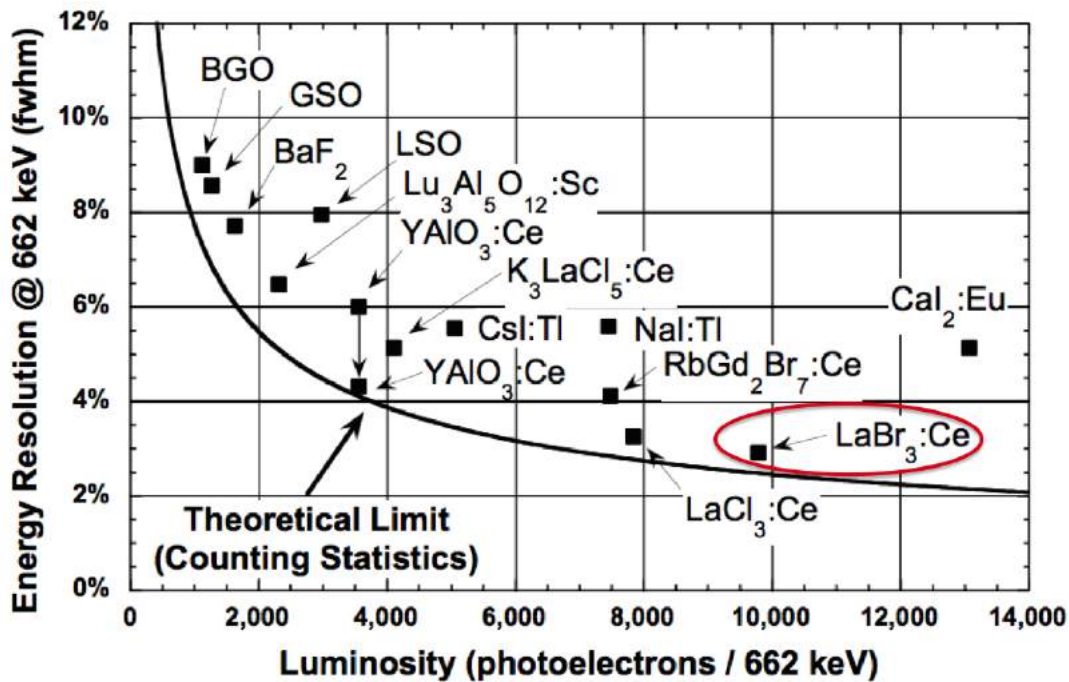
Figure 7.1: *The squares represent the measured energy resolution of each scintillator crystal. The black curve is the theoretical energy resolution limit given by the number of photoelectrons collected. The difference between the experimental measurements and the black curve represent the intrinsic systematic contribute of each crystal. The* LaBr$_3$(Ce) *is encircled in red. Figure from Moses (2002).*

The measured values of energy resolution and light output are worse than the actual state of the art reported. This result has been interpreted as due to the lower quantum efficiency (QE) of the SDD compared with Fiorini et al. (2013). The absence of any additional unknown systematic effects (apart the crystal one) allows us to estimate the expected results for different ENC and QE (Figure 6.31). A detector with an enhanced QE will allow us to achieve state of the art results much more easily than we can obtain reducing electronic noise maintaining the current QE values. Furthermore, the enhanced QE will also increase significantly the timing accuracy in the case of γ-ray events because it will result in higher signal-to-noise ratio. These results led the ReDSoX collaboration to focus their efforts in this direction. Newly produced SDDs with optimized quantum efficiencies have been already produced and will be tested soon.

We are therefore confident that, in the next few months, we can successfully produce an efficient coupling between the SDDs and the LaBr$_3$(Ce), improving the spectroscopic and timing performance results. That would pave the way to high-performance spectroscopic and timing detectors for many proposed future experiments for high-energy astrophysics.

List of Tables

List of Figures

133

Bibliography

M. Ackermann, M. Ajello, A. Allafort, L. Baldini, J. Ballet, G. Barbiellini, M. G. Baring, D. Bastieri, et al. Detection of the Characteristic Pion-Decay Signature in Supernova Remnants. *Science*, 339:807–811, February 2013.

G. Amelino-Camelia, J. Ellis, N. E. Mavromatos, D. V. Nanopoulos, and S. Sarkar. Tests of quantum gravity from observations of γ-ray bursts. *Nature*, 395:525, October 1998.

J. R. P. Angel. Lobster eyes as X-ray telescopes. *The Astrophysical Journal*, 233: 364–373, October 1979.

R. Barkana and A. Loeb. In the beginning: the first sources of light and the reionization of the universe. *Physics Reports*, 349:125–238, July 2001.

R. Campana, F. Fuschino, C. Labanti, M. Marisaldi, L. Amati, M. Fiorini, M. Uslenghi, G. Baldazzi, and others. A compact and modular x- and gamma-ray detector with a csi scintillator and double-readout silicon drift detectors. *Proc. SPIE*, 9905:99056I–99056I–10, 2016.

K. S. Cheng, C. Ho, and M. Ruderman. Energetic radiation from rapidly spinning pulsars. I - Outer magnetosphere gaps. II - VELA and Crab. *The Astrophysical Journal*, 300:500–539, January 1986.

E. Churazov, R. Sunyaev, S. Grebenev, J. Isern, P. Jean, J. Knodlseder, F. Lebrun, M. Renaud, E. Bravo, R. Diehl, and E. Kuulkers. Detection of the 847 keV gamma-

ray line of radio-active Co56 from the Type Ia Supernova SN2014J in M82 with INTEGRAL. *The Astronomer's Telegram*, 5992, March 2014.

E. Costa, F. Frontera, J. Heise, M. Feroci, J. in't Zand, F. Fiore, M. N. Cinti, D. Dal Fiume, L. Nicastro, et al. Discovery of an X-ray afterglow associated with the γ-ray burst of 28 February 1997. *Nature*, 387:783–785, June 1997.

F.C.L. Crespi, F. Camera, N. Blasi, A. Bracco, S. Brambilla, B. Million, R. Nicolini, L. Pellegri, et al. Alpha, gamma discrimination by pulse shape in labr3:ce and lacl3:ce. *Nuclear Instruments and Methods in Physics Research Section A: Accelerators, Spectrometers, Detectors and Associated Equipment*, 602(2):520 – 524, 2009.

R.D. Evans. *The Atomic Nucleus*. @Internat. S.in P. & A. Physics. McGraw-Hill, 1955.

U. Fano. Ionization Yield of Radiations. II. The Fluctuations of the Number of Ions. *Physical Review*, 72:26–29, July 1947.

C. E. Fichtel, G. A. Simpson, and D. J. Thompson. Diffuse gamma radiation. *The Astrophysical Journal*, 222:833–849, June 1978.

C. Fiorini, M. Bellini, A. Gola, A. Longoni, F. Perotti, P. Lechner, H. Soltau, and L. Struder. A monolithic array of 77 silicon drift detectors for x-ray spectroscopy and gamma-ray imaging applications. *IEEE Transactions on Nuclear Science*, 52 (4):1165–1170, 2005.

C. Fiorini, L. Bombelli, P. Busca, A. Marone, R. Peloso, R. Quaglia, P. Bellutti, M. Boscardin, et al. Silicon Drift Detectors for Readout of Scintillators in Gamma-Ray Spectroscopy. *IEEE Transactions on Nuclear Science*, 60:2923–2933, August 2013.

E. Gatti and P. Rehak. Semiconductor drift chamber — An application of a novel charge transport scheme. *Nuclear Instruments and Methods in Physics Research*, 225:608–614, September 1984.

P.F. Sampietro M. Speziali V. Gatti, E. Manfredi. Suboptimal filtering of 1/f noise in detector charge measurements. *Nuclear Instruments and Methods in Physics Research A*, 498(297):467, feb 1990.

A. Georgiev and W. Gast. Digital pulse processing in high resolution, high through-put, gamma-ray spectroscopy. *IEEE Transactions on Nuclear Science*, 40(4):770–779, 1993.

K. Guzik, Z. Tomasz. Algorithms for digital γ-ray spectroscopy. *Nukleonika*, 58(2): 333–338, 2013.

Valentin T. Jordanov and Glenn F. Knoll. Digital synthesis of pulse shapes in real time for high resolution radiation spectroscopy. *Nuclear Instruments and Methods in Physics Research Section A: Accelerators, Spectrometers, Detectors and Associated Equipment*, 345(2):337 – 345, 1994.

Glenn F Knoll. *Radiation detection and measurement; 4th ed.* Wiley, New York, NY, 2010.

C. Kouveliotou, C. A. Meegan, G. J. Fishman, N. P. Bhat, M. S. Briggs, T. M. Koshut, W. S. Paciesas, and G. N. Pendleton. Identification of two classes of gamma-ray bursts. *The Astrophysical Journal, Letters*, 413:L101–L104, August 1993.

C. Kouveliotou, J. Kommers, W. H. G. Lewin, J. van Paradijs, G. J. Fishman, M. S. Briggs, K. Hurley, A. Harmon, M. H. Finger, and R. B. Wilson. GRO J1744-28. *IAU Cirulars*, 6286, January 1996.

C. Kouveliotou, T. Strohmayer, K. Hurley, J. van Paradijs, M. H. Finger, S. Dieters, P. Woods, C. Thompson, and R. C. Duncan. Discovery of a Magnetar Associated with the Soft Gamma Repeater SGR 1900+14. *The Astrophysical Journal, Letters*, 510:L115–L118, January 1999.

S. Hartmann R. Krisch S. Hauff D. Richter R. Soltau H. Struder L. Lechner, P. Eck-bauer et al. Silicon drift detectors for high resolution room temperature x-ray

spectroscopy. *Nuclear Instruments and Methods in Physics Research Section A: Accelerators, Spectrometers, Detectors and Associated Equipment*, 377(2):346 – 351, 1996.

William R. Leo. *Techniques for Nuclear and Particle Physics Experiments*. Springer-Verlag Berlin Heidelberg, 1994.

B.G. Lowe. Measurements of fano factors in silicon and germanium in the low-energy x-ray region. *Nuclear Instruments and Methods in Physics Research Section A: Accelerators, Spectrometers, Detectors and Associated Equipment*, 399(2):354 – 364, 1997.

Gerhard Lutz. *Semiconductor Radiation Detectors*. Springer Berlin Heidelberg, 2 edition, 2007.

M. N. Mazziotta. Electron hole pair creation energy and Fano factor temperature dependence in silicon. *Nuclear Instruments and Methods in Physics Research A*, 584:436–439, January 2008.

C. A. Meegan, G. N. Pendleton, M. S. Briggs, C. Kouveliotou, T. M. Koshut, J. P. Lestrade, W. S. Paciesas, M. L. McCollough, et al. The Third BATSE Gamma-Ray Burst Catalog. *Astrophysical Journal, Supplement*, 106:65, September 1996.

P. Meszaros, P. Laguna, and M. J. Rees. Gasdynamics of relativistically expanding gamma-ray burst sources - Kinematics, energetics, magnetic fields, and efficiency. *The Astrophysical Journal*, 415:181–190, September 1993.

William W Moses. Current trends in scintillator detectors and materials. *Nuclear Instruments and Methods in Physics Research Section A: Accelerators, Spectrometers, Detectors and Associated Equipment*, 487(1‚Äì2):123 – 128, 2002. 3rd International Workshop on Radiation Imaging Detectors.

E. Nakar. Short-hard gamma-ray bursts. *Physics Reports*, 442:166–236, April 2007.

J. A. Nousek, C. Kouveliotou, D. Grupe, K. L. Page, J. Granot, E. Ramirez-Ruiz, S. K. Patel, D. N. Burrows, and others. Evidence for a Canonical Gamma-Ray Burst Afterglow Light Curve in the Swift XRT Data. *The Astrophysical Journal*, 642:389–400, May 2006.

M. J. Rees and P. Meszaros. Relativistic fireballs - Energy conversion and time-scales. *Monthly Notices of the RAS*, 258:41P–43P, September 1992.

M. J. Rees and P. Mészáros. The impact of relativistic fireballs on an external medium: a new model for "cosmological" gamma-ray burst emission. In M. Friedlander, N. Gehrels, and D. J. Macomb, editors, *American Institute of Physics Conference Series*, volume 280 of *American Institute of Physics Conference Series*, pages 987–991, 1993.

G. B. Rybicki and A. P. Lightman. *Radiative processes in astrophysics*. 1979.

R. Sari, T. Piran, and R. Narayan. Spectra and Light Curves of Gamma-Ray Burst Afterglows. *The Astrophysical Journal, Letters*, 497:L17–L20, April 1998.

Schonkeren. *Photomultipliers*. Philips Gloeilampenfabrieken, 1970.

Gerald K. Skinner, Peter von Ballmoos, Neil Gehrels, and John Krizmanic. Fresnel lenses for x-ray and gamma-ray astronomy, 2004.

V. V. Sokolov, T. A. Fatkhullin, A. J. Castro-Tirado, A. S. Fruchter, V. N. Komarova, E. R. Kasimova, S. N. Dodonov, V. L. Afanasiev, and A. V. Moiseev. Host galaxies of gamma-ray bursts: Spectral energy distributions and internal extinction. *Astronomy & Astrophysics*, 372:438–455, June 2001.

H.V. Klapdor-Kleingrothaus T. Kihm, V.F. Bobrakov. A digital multi-channel spectroscopy system with 100 mhz flash adc module for the genius-tf and genius projects. *Nuclear Instruments and Methods in Physics Research Section A- Accelerators Spectrometers Detectors and Associated Equipment*, 498 (1-3):334 – 339, 2003.

G. Zampa, A. Rashevsky, and A. Vacchi. The X-Ray Spectroscopic Performance of a Very Large Area Silicon Drift Detector. *IEEE Transactions on Nuclear Science*, 56:832–835, June 2009.

G. Zampa, R. Campana, M. Feroci, A. Vacchi, V. Bonvicini, E. Del Monte, Y. Evangelista, F. Fuschino, et al. Room-temperature spectroscopic performance of a very-large area silicon drift detector. *Nuclear Instruments and Methods in Physics Research A*, 633:15–21, March 2011.